Calibration of Ultra-high-precision Robots Operating in an Unsteady Environment

THÈSE N° 5098 (2011)

PAR

Emanuele LUBRANO

EPFL

ÉCOLE POLYTECHNIQUE
FÉDÉRALE DE LAUSANNE

Suisse
2011

Version Abrégée

Actuellement, les nanotechnologies contribuent au développement et à la fabrication de produits toujours plus innovants. L'évolution des techniques de fabrication de très haute précision dépend de la capacité à rendre ces processus compatibles avec la production en grande série, permettant ainsi l'usinage et l'assemblage de produits de petite taille en diminuant drastiquement les temps et les coûts de fabrication.

Lorsque l'on considère des produits et des procédés industriels à l'échelle nanométrique, il est nécessaire de comprendre comment les lois de la physique modifient le niveau de précision du procédé. En effet, les phénomènes tels que la friction, le transfert de chaleur et les forces d'adhésion ont un impact plus important qu'à plus grande échelle sur le comportement des corps. Ces différents effets induisent des contraintes et provoquent des déformations dans certaines parties de la structure, influençant ainsi les performances du procédé industriel réalisé par le robot. Il est donc impératif de comprendre comment ces sources d'imprécisions agissent sur les robots dans le domaine nanométrique dans le but d'atteindre une précision submicrométrique. De plus, la compensation de ces différents phénomènes doit être envisagée afin de maintenir la précision absolue du robot dans des niveaux acceptables.

Dans le cadre de cette thèse, une nouvelle procédure d'étalonnage développée spécifiquement pour les systèmes industriels d'ultra haute-précision travaillant dans un environnement thermiquement instable est proposée. Une méthode permettant de compenser l'effet des forces parasites externes agissant sur les robots de très haute précision ainsi qu'une procédure couplant l'étalonnage de plusieurs robots travaillant conjointement ont été développées et expérimentées. La première phase permettant d'atteindre les objectifs fixés dans cette thèse consiste à mesurer les déformations induites par les différentes sources d'imprécision et à modéliser leurs effets pour les compenser en temps réel. Cette phase requiert donc une nouvelle procédure d'étalonnage comprenant les étapes suivantes :

Etape 0 : Conception judicieuse du robot tenant compte du problème de l'étalonnage et de la mesure de la position de l'organe terminal du robot.

Etape 1 : Etude des sources d'imprécisions agissant sur la structure et sur le procédé industriel réalisé par le robot.

Etape 2 : Mesure de la position de l'organe terminal du robot en plusieurs points du volume de travail.

Etape 3 : Identification d'un modèle qui décrit la géométrie et le comportement du robot soumis aux sources d'imprécisions déterminées durant l'étape 1.

Etape 4 : Implémentation du modèle identifié à l'étape 3 dans le contrôleur du robot.

Etape 5 : Validation de l'étalonnage et éventuellement retour à l'étape 1 ou 0.

L'efficacité de cette procédure d'étalonnage a été vérifiée en l'expérimentant sur trois cas d'étude d'ordre de complexité croissant :

- Un axe linéaire de très haute précision a été calibré durant le changement thermique de l'environnement.

- Un robot de très haute précision possédant trois degrés de liberté (Agietron Micro-Nano) a été calibré durant le changement thermique de l'environnement en ayant de plus une force externe agissant sur l'organe terminal du robot.

- Un système composé de deux robots de très haute précision a été étalonné durant le changement thermique de l'environnement. Une étude sur la réalisation du couplage de la calibration des deux robots a été également réalisée.

L'expérimentation de chaque cas a nécessité le développement de systèmes de mesures de très haute précision afin d'acquérir la position et l'orientation de l'organe terminal du robot. L'identification du modèle mathématique décrivant le comportement du robot soumis aux facteurs d'imprécisions est réalisée en déplaçant l'organe terminal sur l'ensemble du volume de travail du robot, soumis aux conditions environnantes instables. L'algorithme « Stepwise Regression » est ensuite utilisé sur les mesures de positions de l'organe terminal du robot afin de modéliser et déterminer l'influence des sources d'imprécisions sur la géométrie du robot. Le modèle obtenu est alors implémenté dans le contrôleur du robot et une validation de l'étalonnage est effectuée.

L'expérimentation de cette procédure d'étalonnage sur chaque robot de très haute précision considéré dans cette thèse a permis d'atteindre des précisions absolues de ±100 nm. En conclusion de cette thèse, une analyse du procédé de nano-indentation comme confirmation de l'étalonnage ainsi que comme méthode industrielle a été réalisée.

Ce travail de thèse a été financé par le Fond National Suisse pour la recherche (FNS).

Mots-clés : Robotique, Nano-robotique, Etalonnage, Haute-précision, Dérive thermique, Forces externes, Stepwise regression, Indentation.

Abstract

In recent years nanotechnology has become an enabling technology for the development and fabrication of new innovative products. The growth of micro- and nano-manufacturing lies in the ability of converting micro- and nano-fabrication techniques into mass-production industrial processes, where small-scale products can be economically manufactured in a short period of time. When dealing with nano-scale objects and industrial processes it is necessary to take into account the physics acting at this level of precision. Phenomena such as friction, heat transfer, and adhesion forces have far more dramatic effects on the deformation of the robot geometry at the nano-scale than at macro- and micro-scales, thus affecting the industrial process that the robot will perform.

The development of micro- and nano-fabrication techniques thus requires a thorough understanding of the physics behind nanorobotics. Specifically, to enable sub-micrometer accuracy for ultra-high-precision robots it is necessary to acquire a complete knowledge of how all sources of inaccuracy deform the robots at nano-scale. Furthermore, a way to compensate for such effects to maintain an acceptable level of accuracy has to be found.

In this thesis we fulfill these needs by proposing a new calibration procedure specifically designed for industrial nano-systems working in a thermally unstable environment, a method to evaluate and compensate for external forces acting on ultra-high-precision robots and a method to relate the calibration of several robots working together.

This is done by measuring how each source of inaccuracy deforms the robot, modeling this effect and compensating it in real-time. To allow this modus operandi, we propose a new calibration procedure summarized in the following six steps:

Step 0: A *judicious design of the robot* that takes into account the calibration problem and the pose measurement,

Step 1: *Study of the sources of inaccuracy* linked to the robot and the industrial process that it will perform,

Step 2: *Measurement* of several end-effector poses,

Step 3: *Identification* of a function that describes the robot geometry and its behavior when subjected to the sources of inaccuracy identified in *Step 1*,

Step 4: *Implementation* of the model found in *Step 3* into the robot controller,

Step 5: *Validation* and potential return to *Step 1* or *Step 0*.

The effectiveness of this calibration procedure is proven by testing it on three case studies, examined in order of complexity:

- A 1 DOF (degree(s)-of-freedom) ultra-high-precision linear axis was calibrated while thermal effects were deforming it.

- The 3 DOF ultra-high-precision parallel robot Agietron Micro-Nano was calibrated while thermal effects and an external force were acting on it.

- An ultra-high-precision 2-robot system was calibrated while thermal effects were acting on it. Thus, an exhaustive study on relating the references of the two robots was carried out.

For each case we developed an appropriate ultra-high-precision measuring system used to acquire the pose of the robot end-effector. We measured the end-effector position throughout the workspace while the sources of inaccuracy were acting on the robot to map how they affect the robot geometry. We used the Stepwise Regression algorithm to identify a mathematical model able to describe the geometric features of the robot while all the sources of inaccuracy are acting on it. The model is then implemented in the robot controller and a validation of the calibration accuracy is performed. For every ultra-high-precision robot considered in this work we reached an absolute accuracy of ±100 nm. We finished the coverage of this thesis by analyzing the nano-indentation process as a calibration confirmation tool and as an industrial process. Furthermore, we describe how to use a multiple ultra-high-precision concurrent system of robots.

    This work was financed by the FNS (Swiss National Foundation for research).

Keyword: Robotics, Nano-Robotics, Calibration, High-precision, Thermal Drift, External Forces, Stepwise Regression, Indentation.

Acknowledgements

Contents

Abbreviations and Conventions

Acronyms

DGM: Direct Geometric Model.

DOF: Degree(s) of Freedom.

(μ-, wire-)EDM: (micro-, wire-) Electric Discharge Machining.

IGM: Inverse Geometric Model.

MRA: Multiple Regression Analysis.

RMS: Root Mean Square (error).

SEM: Scanning Electron Microscope.

UHMWPE: Ultra-High-Molecular-Weight Polyethylene.

Institutes Mentioned in this Work

CMI: Center of Micronanotechnology (EPFL, Switzerland).

EPFL: École Polytechnique Fédérale de Lausanne (Switzerland).

FNS: Swiss National Foundation for Research.

LSRO: Laboratory of Robotic Systems (Institute of Microengineering, School of Engineering, EPFL).

METAS: Swiss Federal Office of Metrology.

Conventions

Axes: x, y, z

End-effector coordinates: $x, y, z, \theta_x, \theta_y, \theta_z$

Force: F

Matrix: $\mathbf{M}$

Motor coordinate: q_i (where i is the motor axis number)

Orientation: $\theta_x, \theta_y, \theta_z$

Point: $A(x, y, z)$ on a 3D coordinate system, $A(x, y)$ on a 2D coordinate system

Pose: $x, y, z, \theta_x, \theta_y, \theta_z$

Position: x, y, z

Temperature: t_i (where i is the thermal sensor related to the temperature)

Vector of error values: E

Vector of force values: $\bar{F}$

Vector of motor coordinates: Q_i (where i is the motor axis number)

Vectors of rotational measures: $\Theta_X, \Theta_Y, \Theta_Z$

Vector of temperatures: T_i (where i is the thermal sensor related to the temperature)

Vectors of tranlational measures: X, Y, Z

Part I

Theory, Methodology and Materials

Chapter 1

Introduction

1.1 General Introduction

In the first decade of the 21st century, nano-technology has become an enabling technology. As a matter of fact, several innovative products available on the market today have been manufactured using nano-fabrication processes (*e.g.* nano-imprint lithography). New nano-manufacturing techniques are still in development [79]. At the nanometer scale, technology has been moving towards greater control of the structure of the matter itself, suggesting the feasibility of achieving thorough control of molecular structures, atom by atom.

The future development of micro- and nano-manufacturing lies in the ability of converting micro- and nano-fabrication techniques into mass-production manufacturing processes, where small-scale products can be economically manufactured in a short period of time [40]. In this context, we believe that *a full understanding of the physics behind nanorobotics* and *the development of micro- and nano-factories* are key to the future development of nanotechnologies (and the growth of the companies involved in their development).

Nanorobotics is the study of large robots capable of manipulating objects that have dimensions in the nano-scale range with nanometer resolution or accuracy, *i.e.* ultra-high-precision robots [16].

Micro- and *nano-factories* are small system where one or more ultra-high-precision robots perform one or more manufacturing processes on certain work-pieces. Often they are designed to be modular and to supply a clean environmental system for the manufacturing process [88].

At the nano-scale, physical phenomena like friction, heat transfer, and adhesion forces have far more dramatic effects than at macro- and micro-scale [55, 92]. For example, in Figure 1.1 we observe the influence of the temperature on the positioning capability of an ultra-high-precision robot. In this experiment, the robot was kept steady at the level of the encoders by its motors. Despite that, we measured that the end-effector was drifting almost proportionally to the robot temperature.

Another significant example is shown in Figure 1.2. Here we see the effect of an external force applied on a robot end-effector. In this case the robot was controlled to hold the same position and appears to be steady when reading the motor encoders (with a resolution of 5
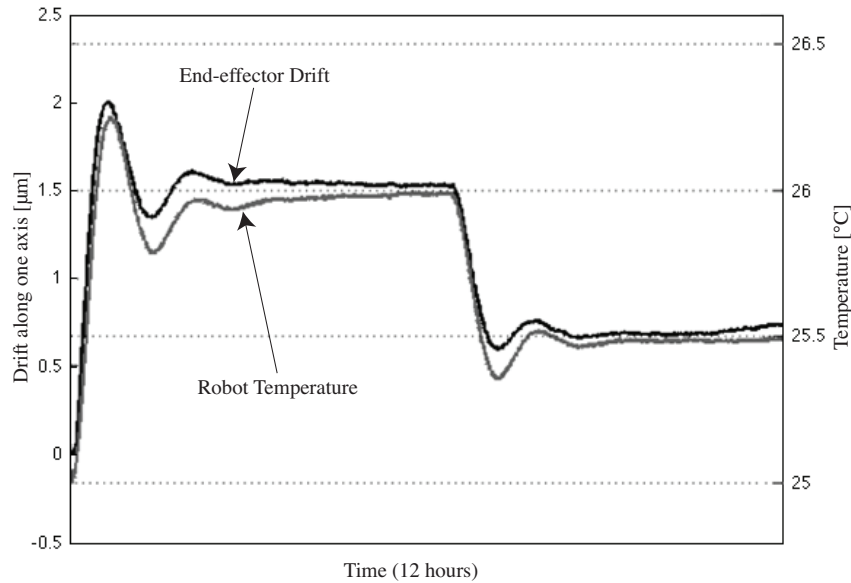
Figure 1.1: *Plot of a robot end-effector position drift versus the robot temperature evolution. During the measures, the robot was kept steady by its controller.*

nm and an incertitude of ±30 nm). Notice that also in this case the end-effector misplacement appears to be proportional to its cause.

In the light of the previous examples, we deduce that to enable sub-micrometer accuracy of ultra-high-precision robots it is necessary t*o elaborate a full understanding of the sources of inaccuracy acting on them at nano-scale.* Furthermore, *a way to compensate such effects* has to be proposed.

In this thesis we fulfill these needs by proposing a new calibration procedure specifically designed for industrial nano-systems, a method to evaluate and compensate for external forces acting on ultra-high-precision robots, and a method to establish a relationship between the calibration of several robots working together.

This work is highly multidisciplinary; in fact, it encompasses several scientific disciplines, such as robotics, physics, metrology, computer science, mathematics and science of materials. We believe that following the guidelines described here it will be possible to evolve many of the nano-fabrication processes available now, allowing a stronger use of robots and miniaturizing mass-production lines.

1.2   Preliminary Definitions

Here we present a few preliminary concepts essential for the understanding of this thesis: we will introduce the conventions adopted in this work, the robot geometric models, the quantities that define the positioning capability of a robot, and some techniques used to develop ultra-high-precision robots.
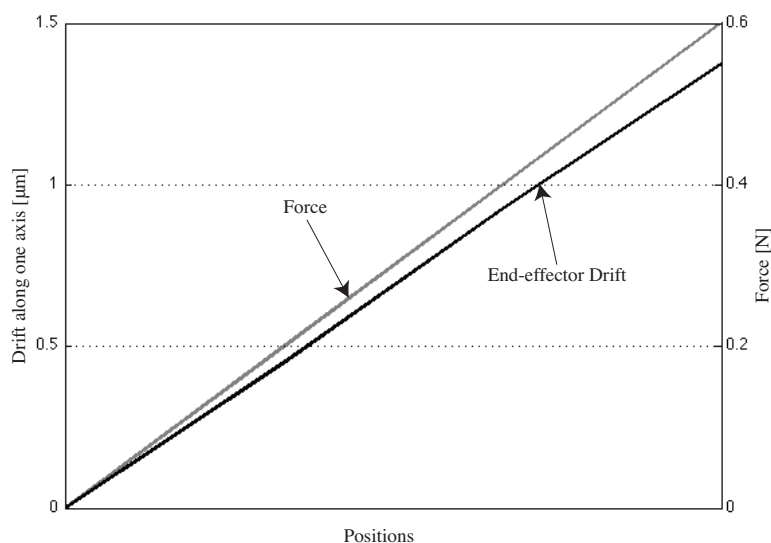
Figure 1.2: *Displacement caused by a force applied on a robot end-effector. During the experiment the robot is kept steady by its controller (with a resolution of 5 nm and an incertitude of ±30 nm). The displacement is measured along the same direction of the force.*

1.2.1 Coordinate System, Pose and Geometric Models

A *coordinate system* is used to describe the pose of a robot end-effector. It consists of three axes x, y, and z which are orthogonal and have the same *zero* point x_0, y_0, z_0. The frame $x_0, y_0, z_0, \theta_{x_0}, \theta_{y_0}, \theta_{z_0}$ defines the origin and the orientation of the *end-effector coordinates* system; and is called *reference* frame.

The *pose* of a robot end-effector is always described using six coordinates, *i.e. x, y, z,* $\theta_x, \theta_y, \theta_z$, where *x, y, z* describe the *position* of the end-effector towards the zero, while its *orientation* is described by the angles $\theta_x, \theta_y, \theta_z$ (refer to Figure 1.3).

The *motor coordinates* system is defined on the angular or translational coordinates of each joint of a robot. On an n DOF[1] robot, for each set of motors coordinates $q_1, \ldots, q_n$ there corresponds an end-effector coordinate $x, y, z, \theta_x, \theta_y, \theta_z$. Notice that independently from the number of DOF, the end-effector pose in end-effector coordinates is always described by the 6 variables seen before. Nevertheless, for kinematically redundant robots (generally where $n > 6$) or other robots having more postures for the same end-effector pose there could be more joints configuration $q_1, \ldots, q_n$ corresponding to the same end-effector pose $x, y, z, \theta_x,$ θ_y, θ_z [82].

The Geometric models of a robot are used to transform one coordinate system to another. We illustrate them in the next page.

---

[1]DOF: Degree(s) of freedom.
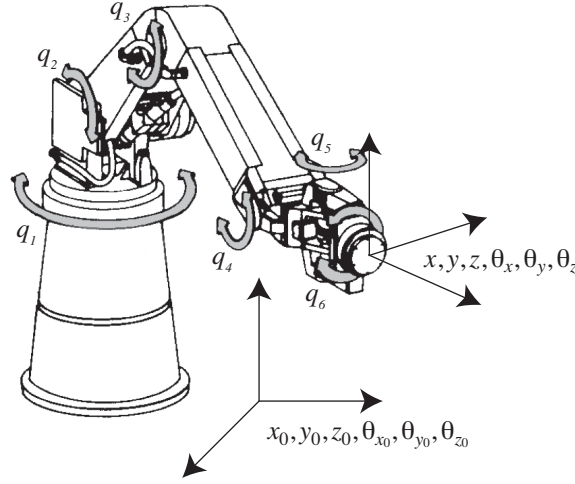
Figure 1.3: *The notation convention used in this thesis.*

Direct Geometric Model (DGM)

The DGM (Figure 1.4, left) is a complex mathematical function that takes as input a set of motors coordinates $q_1,\ldots,q_n$ and returns the corresponding set of end-effector coordinates $x,y,z,\theta_x,\theta_y,\theta_z$:

$$x,y,z,\theta_x,\theta_y,\theta_z = DGM(q_1,\ldots,q_n) \tag{1.1}$$

Inverse Geometric Model (IGM)

The IGM (Figure 1.4, right) is the inverse transformation of the DGM. It takes as input a set of end-effector coordinates $x,y,z,\theta_x,\theta_y,\theta_z$ and returns the corresponding motors coordinates $q_1,\ldots,q_n$:

$$q_1,\ldots,q_n = IGM(x,y,z,\theta_x,\theta_y,\theta_z) \tag{1.2}$$

The utility of having such coordinate transformations lies in the fact that the human operator will control the robot in end-effector coordinates, while the robot itself is controlled using motor coordinates. Since the IGM transformation is the one that is finally used to operate the robot, we will consider the calibration of this relationship. Nevertheless, all the techniques discussed in this thesis can be also applied to the DGM transformation.
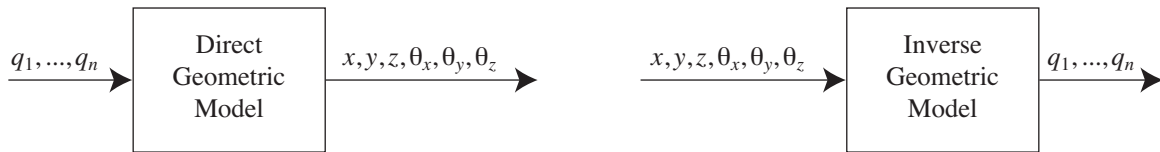
Figure 1.4: *The Direct Geometric Model (left) and the Inverse Geometric Model (right) transformations.*

1.2.2 Linearity and Time-invariancy

In system theory, the system described by the function $f(x)$ is called *linear* when the following properties are satisfied:

$$f(x + y) = f(x) + f(y) \tag{1.3}$$

$$f(\alpha x) = \alpha f(x) \tag{1.4}$$

Where x and y are input of the system and α is a constant. The property expressed by Equation 1.3 is called *additivity*, while the one expressed by Equation 1.4 is called *homogeneity*.

A time-invariant system described by the function $f(x, t)$ satisfies the following property:

$$f(x, t) = f(x, t + \tau) \tag{1.5}$$

Where x is an input of the system and t and τ are time instants. The propery expressed by Equation 1.5 is called *time-invariancy*, and its meaning is that, given a certain input to a system, the output will be the same independently from time.

A robot geometric model is generally described by a *nonlinear time-invariant* function. A geometric model is nonlinear because normally it contains terms of order greater than the first, so it does not respect the conditions expressed by Equations 1.3 and 1.4. On the other side, as time is frequently not kept in account in this kind of transformations, the model is implicitly time-invariant.

1.2.3 Accuracy, Precision and Resolution

The terms accuracy, precision and resolution are used to characterize the positioning capability of a robot [1]. Such quantities can be expressed in terms of motors coordinates as well as in terms of end-effector coordinates:

- *Accuracy* (*Précision absolue* in French) is the difference between a nominal pose that a robot has to reach, and the actual pose that it has reached. For a single pose it is represented by a measure, while when dealing with more poses it is considered as a statistical measure. Furthermore, we define *departing accuracy* as the accuracy that the robot has before calibration, and *final accuracy as* the accuracy reached by the robot after the calibration process.

- *Precision* or *Repeatability* (*Précision Relative* or *Répétitivité* in French) is a statistical measure of how much a robot actual motions differ from each other when the robot is commanded to repeat a single desired motion.

- *Resolution* (*Résolution* in French) is the finest incremental motion that can theoretically be achieved by a robot. The resolution at the level of the joints corresponds to the resolution of the joint sensors.
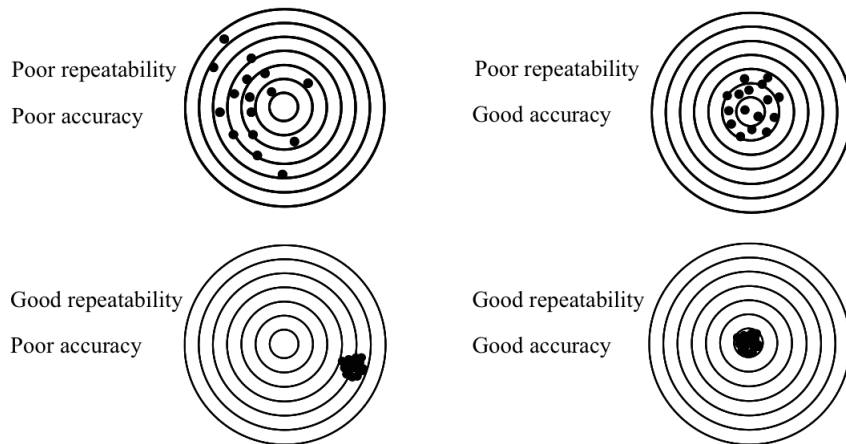
Figure 1.5: *Repeatability and accuracy of a shooter evaluated from the observation of different shooting targets.*

To clarify the difference between accuracy and repeatability, a clever analogy with a shooter is shown in Figure 1.5 [27]. Repeatability and resolution are characteristics that are intrinsic to the robot design and assembly; therefore once the robot is built they are difficult to be improved. On the other side, accuracy is strictly linked to the mathematical models of the robot, hence easier to change: by optimizing the mathematical description of the robot behavior it is possible to enhance the accuracy.

1.2.4   Ultra-high-precision Robots

In this thesis we will use several times the expressions "high precision" and "ultra-high precision". We define them here:

- *High precision*: devices with precision between 10 and 1 μm.

- *Ultra-high precision*: devices with precision between 1 μm and 1 nm.

Developing and building *ultra-high-precision robots* is a challenging task that requires a deep mastering of different engineering fields such as physics, material science and electronics. In our laboratory, the LSRO[2], we adopt the following solutions and technologies to develop ultra-high-precision robots:

- *Parallel kinematic*: in a parallel configuration, all the arms of the robot are attached to the end-effector, creating one or more closed-loop kinematic chain. The advantages of this configuration are high-dynamics, high-acceleration and good stiffness. This configuration has the drawback of having a limited working volume and a geometric model more complex than a serial.

---

[2]LSRO: Laboratoire de Systèmes Robotiques, EPFL, Lausanne, Switzerland.

- *Ultra-high-precision sensors*: the robot positioning precision is directly inherited by the precision of its motor sensors. For this reason it is fundamental to use sensors with nanometric precision.

- *High-precision actuators*: we use voice coils or mobile magnet motors to avoid introducing dry-friction into the system.

- *Flexure-hinge joints*: with these types of joints it is possible to have motion without dry-friction, backlash or wear. As in the case of parallel kinematics, the drawback of this kind of joint is the limited working space.

The robots considered in this work will be introduced in detail in Chapter 4.

1.3 What is Robot Calibration

Calibration is a process used to enhance robot-positioning accuracy. It consists in modifying the robot software instead of modifying its mechanical structure or redesigning it. To achieve this goal, the calibration procedure involves the development of a model whose parameters accurately represent the real robot's behavior [20].

Since robot calibration is used to increase the final accuracy of a robot, it is not needed for all those processes or applications where *only the precision* is relevant (refer to subsection 1.2.3 on page 7 for the definitions of accuracy and precision), *e.g.* when the end-effector position is constantly monitored using a camera; calibration will be used anyway to improve the accuracy of the camera or the sensors involved in the robot controller, but not directly on the robot.

Robot calibration is a procedure that encompasses four distinct actions [97]:

Step 1: Determination of the robot IGM (*Modeling*),

Step 2: *Measurement* of several end-effector poses,

Step 3: Mathematical *Identification* of the difference between the geometric model found in *Step 1* and the real end-effector poses measured in *Step 2*,

Step 4: *Implementation* of the model found in *Step 3* in the robot controller.

In the rest of this thesis we will refer to this method as the "classic calibration procedure". The following paragraphs introduce these steps in details.

Step 1: Kinematic Modeling

Modeling consists in establishing the robot DGM and IGM, which will be successively used to displace the robot. The robot designer normally carries out this task by finding a mathematical relationship that describes the needed coordinate transformations.

For the purpose of calibration, we consider only the IGM. As seen in the previous subsection, this function has as input the desired end-effector pose, and returns the corresponding motors coordinates (Equation 1.2).

Step 2: Pose Measurement

In this phase, an $m \times 6$ matrix of *ideal poses* $\mathbf{P_e} = [X, Y, Z, \Theta_x, \Theta_y, \Theta_z]$ is generated. This matrix contains the m poses in which the end-effector will be displaced. While the end-effector is moved in each pose, a 6 DOF measuring system is used to determine the real end-effector pose corresponding to each ideal one. By using such measures, the matrix of the *real poses* $\mathbf{R_e}$ is built:

$$\mathbf{R_e} = \left[X_r, Y_r, Z_r, \Theta_{x_r}, \Theta_{y_r}, \Theta_{z_r} \right]$$

At this point we calculate the positioning error matrix in end-effector coordinates $\mathbf{E_e}$ of the robot:

$$\mathbf{E_e} = \left[E_x, E_y, E_z, E_{\theta_x}, E_{\theta_y}, E_{\theta_z} \right] = \mathbf{P_e} - \mathbf{R_e} \tag{1.6}$$

It is now possible to calculate, for each column of the matrix $\mathbf{E_e}$, all the statistical values[3] required to characterize the robot positioning error in *end-effector* coordinates.

Step 3: Kinematic Identification

We recall here that the IGM does the following transformation (Equation 1.2):

$$q_1, \ldots, q_n = IGM(x, y, z, \theta_x, \theta_y, \theta_z)$$

To achieve robot calibration, *we have to find an inverse geometric model that describes the robot geometry in a closer way. The new function has to return the same motor coordinates of the not calibrated IGM, but from the real end-effector coordinates* $x_r, y_r, z_r, \theta_{x_r}, \theta_{y_r}, \theta_{z_r}$ (Figure 1.6).

---

[3]There are several strategies to extract a statistical indicator from a vector of errors. One of the most common is performing the Root Mean Square (RMS) of the vector elements. This operation consists in calculating the square root of the average of the squares of the values.

In this thesis we use a different method: to reduce the error vector into a single element we consider the standard deviation of the error vector, limited to a confidence interval of 90% (corresponding to 1.645σ). In this way we are able to exclude errors too far from the error mean (often due to random effect or measuring errors, therefore distinguished from causal variations). Furthermore, as Dr. Fazenda used this parameter to evaluate his calibration, we allow the direct comparison with the results of his PhD thesis [27] (introduced in 2.1 on page 17).
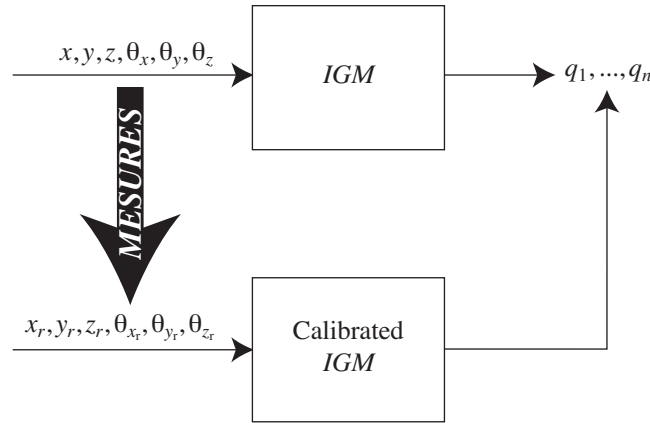
Figure 1.6: *Comparison between IGM and calibrated IGM.*

If we insert each line of the *ideal poses* matrix $\mathbf{P_e} = \begin{bmatrix} X, Y, Z, \Theta_x, \Theta_y, \Theta_z \end{bmatrix}$ in the IGM, we will obtain a matrix of the *ideal* motor coordinates used to displace the end-effector in such poses: $\mathbf{P_m} = [Q_1, \ldots, Q_n]$, $m \times n$ matrix where m is the number of positions and n is the DOF of the robot.

In the same way, we insert in the IGM of the robot each line of the real end-effector pose matrix $\mathbf{R_e} = \begin{bmatrix} X_r, Y_r, Z_r, \Theta_{x_r}, \Theta_{y_r}, \Theta_{z_r} \end{bmatrix}$. We obtain the matrix $\mathbf{R_m} = \begin{bmatrix} Q_{1_r}, \ldots, Q_{n_r} \end{bmatrix}$.

We calculate the matrix $\mathbf{E_m}$, that expresses the positioning error in motor coordinates:

$$\mathbf{E_m} = \begin{bmatrix} E_{q_1}, \ldots, E_{q_n} \end{bmatrix} = \mathbf{P_m} - \mathbf{R_m} \tag{1.7}$$

The identification consists in finding a mathematical function that returns the error in motor coordinates $e_{q_1}, \ldots, e_{q_n}$ while providing in input the corresponding real end-effector pose $x_r, y_r, z_r, \theta_{x_r}, \theta_{y_r}, \theta_{z_r}$:

$$e_{q_1}, \ldots, e_{q_n} = error(x_r, y_r, z_r, \theta_{x_r}, \theta_{y_r}, \theta_{z_r}) \tag{1.8}$$

Notice that from a mathematical point of view this is only one of the possible ways of seeing the calibration problem. Actually, all the functions and procedures able to match the relationship between *measured end-effector coordinates* and *ideal motor coordinates* perform the robot calibration.

Step 4: Kinematic Compensation

In the last step we find a function that describes the positioning error of the end-effector while using the IGM. By adding it to the IGM (Figure 1.7) we compensate this error and we obtain a model describing the robot in a way closer to reality: the calibrated IGM.

To finish the calibration procedure, the IGM in the robot controller has to be substituted with the Equation 1.9:

$$q_1, \ldots, q_n = IGM(x_r, y_r, z_r, \theta_{x_r}, \theta_{y_r}, \theta_{z_r}) + error(x_r, y_r, z_r, \theta_{x_r}, \theta_{y_r}, \theta_{z_r}) \tag{1.9}$$
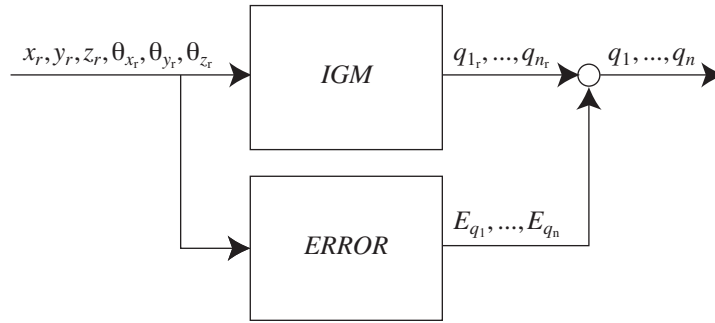
Figure 1.7: *The blocks forming the calibrated model.*

1.4   Issues in Ultra-high-precision Robot Calibration

In this section we will introduce the sources of inaccuracy that act at the macro-, micro-, and nano-scales on ultra-high-precision robots. According to the literature, they can be classified in three groups [27]:

- *Geometric errors.*

- *Non-geometric errors.*

- *Effects linked to the robot working conditions* (environment and manufacturing process).

Geometric errors are caused by the mismatch between the robot geometric model and the real robot geometry. They are due to manufacturing tolerances and to the assembly of different components. Since these errors are systematic, they can be compensated using a calibration procedure.

   Non-geometric errors are dependent on robot configurations. They are caused by friction, wear and backlash. They are very difficult to treat using a calibration procedure. Normally one tries to avoid them through good robot design.

   The analysis, modeling and compensation of the *effects linked to the robot working conditions* are the principal topic of this thesis. Because of their significant effect at nano scale, these issues are more relevant for ultra-high-precision robots. As we will see in section 2.3, the principal factors that besides geometric errors lower the accuracy of such robots are the followings:

1. *Thermal effects.*

2. *External forces* acting on the robot.

3. Incertitude in the *reference* / use of *multiple robots.*

Those factors will be introduced in detail in the state of the art (Chapter 2).

1.5 The Objective of this Thesis

In this section we provide the postulate, the goal, the original contributions and the organization of this thesis.

1.5.1 Postulate

"The accuracy of ultra-high-precision robots can be enhanced by using a calibration procedure that takes into account the physical phenomena acting on the robot at macro-, micro-, and nano-scale: namely geometric errors, thermal effects, external forces and incertitude in the reference positioning. Those are measured, modeled and then compensated in real-time during robot use."

1.5.2 Goal

The purpose of this thesis is to allow the use of ultra-high-precision robots in *unsteady environments* and *during the manufacturing process* without compromising the final accuracy of the robot. To do so, we provide a new calibration technique that besides correcting the robot geometric errors is able to model and compensate all the sources of inaccuracy acting on the robot.

The goal of this work has been divided and attained according to the following steps:

- How ultra-high-precision robots are influenced by *environment thermal variations,*

- How ultra-high-precision measuring devices are influenced by *environment thermal variations,*

- How *external forces* act on the robot geometry,

- How to relate the robot reference to *the reference of the tool-tip* mounted on the robot end-effector,

- How relate *the references of two-robot system,*

- Proposing a *general calibration procedure* able to handle these sources of inaccuracy,

- Verifying the calibration by mean of *nano-indentation.*

1.5.3 Original Contributions

As we will see in detail in Section 2.1, this thesis is the direct continuation of a previous work performed in our laboratory: Dr. N. Fazenda's thesis on ultra-high-precision robots calibration[4]. The original contributions that we are going to list here are presented directly in comparison with the ones of this previous work (of which the contributions are presented in parenthesis, for purpose of comparison):

---

[4] [27]: N. Fazenda. *Calibration of high-precision flexure parallel robots.* PhD Thesis n. 3712, Lausanne, EPFL, 2007.

- We propose a *general calibration procedure for ultra-high-precision robots* that keeps in account and corrects the effect of external sources of inaccuracy acting on them (the calibration strategy proposed in [27] only corrects the geometric errors of an ultra-high-precision robot). Furthermore, we prove the effectiveness of this procedure by testing it on three case studies.

- A *6 DOF ultra-high-precision measuring system* has been proposed and adapted for each of the case studies (in Fazenda's thesis a 3 DOF ultra-high-precision measuring system was proposed: to obtain 6 DOF data for calibration such system was mounted along different measuring axes, the measures were then collected and assembled together through the use of a complex procedure). With the system proposed in this thesis it is possible to collect straightaway the measurements for the calibration. We will see that the measuring strategy proposed here is less time-consuming in comparison with the one of Dr. Fazenda.

- The influence at nano-scale of three sources of inaccuracy on ultra-high-precision robots has been investigated: *thermal effects, external forces and reference incertitude.* Those are measured and their effect on the robot is evaluated and compensated during robot usage (in Fazenda's work thermal effects are avoided by stabilizing the whole system and the other sources of inaccuracy are not considered).

- We propose a single *data processing algorithm* capable of fitting the calibration data and producing a good quality calibrated model within seconds (while Dr. Fazenda proposed a comparison of several mathematical algorithms that are effective but extremely slow in computation).

- We suggest *a mathematical approach to rapidly identify the inverse geometric model of a robot without knowing its geometry in details,* while knowing the matching between motor coordinates and corresponding end-effector coordinates.

Since – at the best of our knowledge – no one has yet calibrated ultra-high-precision robots while keeping in account external effects acting on them[5], we consider the case studies of this thesis as "practical" original contributions. We successfully perform the calibration of the following robots:

- An ultra-high-precision *linear axis.* The calibration performed in this case takes in account the deformations introduced by the thermal instability of the environment. Furthermore, we propose an exhaustive investigation on the importance of each parameter and each thermal sensor used for the calibration.

- The 3 DOF ultra-high-precision robot *Agietron Micro-Nano.* The robot is calibrated while thermal effects and an external force are acting on it. Using the experience gathered through the calibration of the linear axis, we are able to compensate for the thermal drift. Furthermore, we impose a force on the end-effector, in order to simulate

---

[5]In fact, Dr. Fazenda succeeded in the calibration of exclusively the geometric errors of two ultra-high-precision robots.

the cutting-forces coming from the industrial process that the robot will perform. We demonstrate that we are able to compensate for the structural deformations caused by both effects at the same time.

- The 2-robot system composed by the *Agietron Micro-Nano* and the 3 DOF high-precision robot *MinAngle*. For the first time, the issues coming by the concurrent use of two robots working at nano-scale level are considered. We discuss how to handle the merging of their two coordinate frames, as well as the thermal effects acting on both of them.

- The 2-robot system performing nano-indentation. In the purpose of using the nano-indentation as a tool for calibration validation[6], we adjust the 2-robot system models in order to compensate the effects coming from this process.

The most important improvement in comparison to [27] consists in the fact that the approach proposed here finally *consents the use of ultra-high-precision robots in an industrial context at ultra-high precision*. In a relatively short time, our calibration procedure allows the compensation in real-time of all the sources of imprecision considered, preserving the accuracy reached after the calibration process also during the robot usage.

1.6 Organization of this Thesis

We have organized the explanation of all the matters in the following way:

- In *Chapter 2* we analyze the results and the procedures set out in Dr. Fazenda's thesis. Furthermore, we present the research state of the art on ultra-high-precision measurements, compensation of thermal effects and/or external forces acting on ultra-high-precision robots and the handling of the reference issue on industrial robots.

- *Chapter 3* is the core of this thesis. Here we introduce in detail the proposed calibration methodology and the theory behind it.

- In *Chapter 4* we present the three robots considered in the case studies. Furthermore, we introduce all the measuring instruments and all the other devices developed to perform the practical experiences of this thesis.

- *Chapters 5, 6,* and *7* respectively introduce the three case studies considered in this thesis. For each case we apply the calibration procedure presented in Chapter 3. We describe in details all the steps done to perform the calibration, from the development of the measuring system to the data processing. The calibration results and a commentary for each case are presented at the end of each respective chapter.

---

[6]Nano-indentation has been proposed as a tool for calibration validation for the first time in Dr. Fazenda's thesis.

- In *Chapter 8* we continue the discussion begun in Chapter 7 by introducing nano-indentation. We present the sources of inaccuracy coming from this process and coming from the concurrent use of the two robots. To conclude the chapter, we present and comment the nano-indentation results.

- *Chapter 9* concludes this thesis. Here we present a summary of the results and contributions arising from this work. Finally, we outline some suggestions to continue the research on ultra-high-precision robot calibration.

Chapter 2

State of the Art

As mentioned in Chapter 1, this thesis follows the outcome of a previous PhD thesis done at the LSRO: "*Calibration of high-precision flexure parallel robots*", by Dr. N. Fazenda [27].

In the first part of this chapter we will summarize the key points of Fazenda's thesis and the conclusions that have motivated the follow-up of his research.

In the second part we will introduce the state of the art of the areas related to this thesis, presented in this order:

1. Research on *ultra-high-precision measuring system.*

2. Studies on *external effects acting on robots:*

   (a) Thermal effects.
   (b) External forces.
   (c) Thermal effects and External forces.
   (d) Reference incertitude (between the robot end-effector frame and its tool-tip frame, or between two or more robots tool-tip frame).

Standard robot *geometric calibration* is an area of research that has grown considerably over the last thirty years. For this reason we can find a large number of publications on this subject, including textbooks [4, 56] and survey papers [20, 37, 73, 87]. Since this topic is very well covered, this state of the art will focus especially on works related to ultra-high-precision robot calibration.

2.1 Previous Research at LSRO

In [27], a methodology for the calibration of ultra-high-precision robots was proposed. To prove the effectiveness of this concept, two case studies are presented: the calibration of the translational 3 DOF robot *Delta Cube 2* (Figure 2.1) and the calibration of the 6 DOF robot *Sigma6* (Figure 2.2). Furthermore, an exhaustive study of all the data-processing techniques to perform calibration is proposed. Finally, nano-indentation is suggested and employed as a method to confirm the calibration.
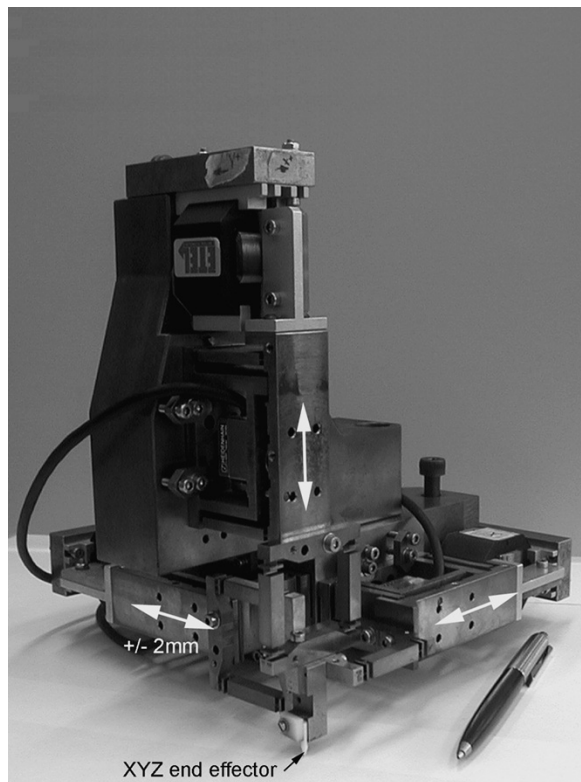
Figure 2.1: *The robot Delta Cube 2.*
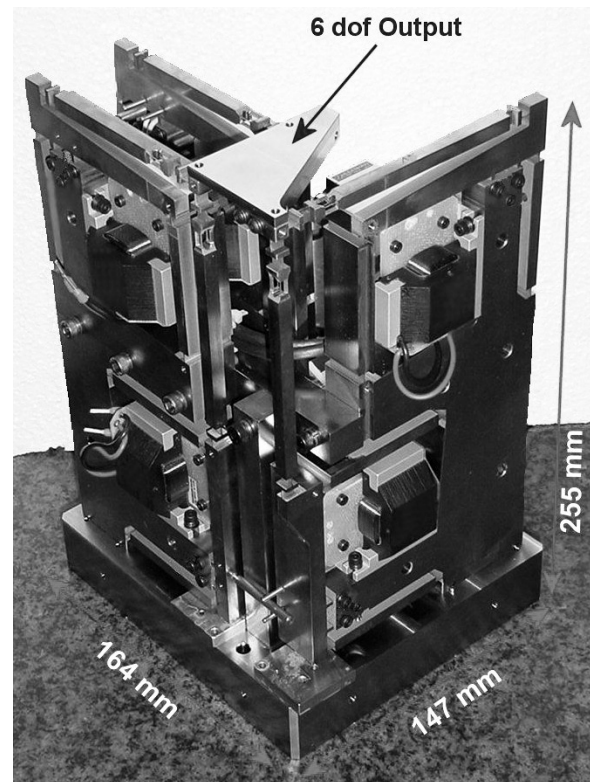
Figure 2.2: *The robot Sigma6.*

2.1.1   The Methodology

Dr. Fazenda proposed a calibration procedure of 5 phases:

Step 0:   Some *basic decisions before the calibration* work have to be taken: The choices of the measuring devices and the measuring procedure are of special importance.

Step 1:   The *measuring devices have to be prepared* for data acquisition (configurations of the measuring devices and data acquisition software development).

Step 2:   After a thermal stabilization, *the measurements are acquired.*

Step 3:   Using a model-based or a model-free approach, *the data processing is carried out.*

Step 4:   The *calibration is verified* using an alternative measuring strategy.

Notice that in this work a remarkable emphasis is given to the measuring phase. This is done because the measurement quality directly affects the accuracy reachable with the calibration process. For this reason while in the classic calibration algorithm[1] there is just one step

---

[1]Summary of the classic calibration steps as seen in section 1.3 on page 9:

Step 1: Modeling,

Step 2: Measurement,

Step 3: Identification,

Step 4: Implementation.

devoted to the measurements, in Fazenda's thesis there are *steps 0, 1* and *2* dedicated to this task. Meanwhile, *step 3* remains unaltered from the classic procedure and *step 1* of the classic calibration procedure disappears. Finally, a new point used to verify the calibration is introduced (*step 4*).

2.1.2 The Measuring Systems and the Measuring Procedures

Two different measuring strategies have been described in [27], one for each robot. Both have in common:

- The use of a high-precision mirror cube in Zerodur®, with a flatness on each measuring surface better than $\lambda/20$ (~30 nm). A cube is mounted on each robot end-effector. It defines the position and the orientation of the absolute frame of each robot and reflects the beams of the measuring devices.

- The application of 10 *pt1000* thermal sensors, used to monitor thermal changes on sensitive parts of the measuring loop (robot, robot's frame and measuring device supports).

- The employ of a SIOS SP-2000 Interferometer for the measure of translations and a Newport LDS-1000 Autocollimator for the measure of rotations. Those measuring instruments will be introduced in detail in section 4.2 on page 55, while their working principle will be described in Appendix A on page 131.

- The thermal stabilization of the system: to avoid thermal drift in the measures and deformations of the robot due to changes in the temperatures, the measuring system and the robot were mounted in an insulated box, where a thermal stabilization of the air is performed.

In the following sub-subsections we will underline the differences in the measuring system and strategy for the Delta Cube 2 and for the Sigma6 robots.

2.1.2.1 Delta Cube 2

The workspace of the Delta Cube 2 robot occupies a volume of ~4 × 4 × 4 mm^3. The stroke in translation along one axis is completely measurable with one interferometer and the parasitic rotations around two axes are largely measurable with a single autocollimator.

To obtain a 6 DOF dataset necessary for the calibration, the following steps have to be executed (Figure 2.3 on the next page):

1. Interferometer mounted along x axis, autocollimator mounted to measure θ_y and θ_z.

2. Thermal stabilization.

3. Measure along x, θ_y and θ_z.

4. Interferometer mounted along y axis, autocollimator mounted to measure θ_x and θ_y.
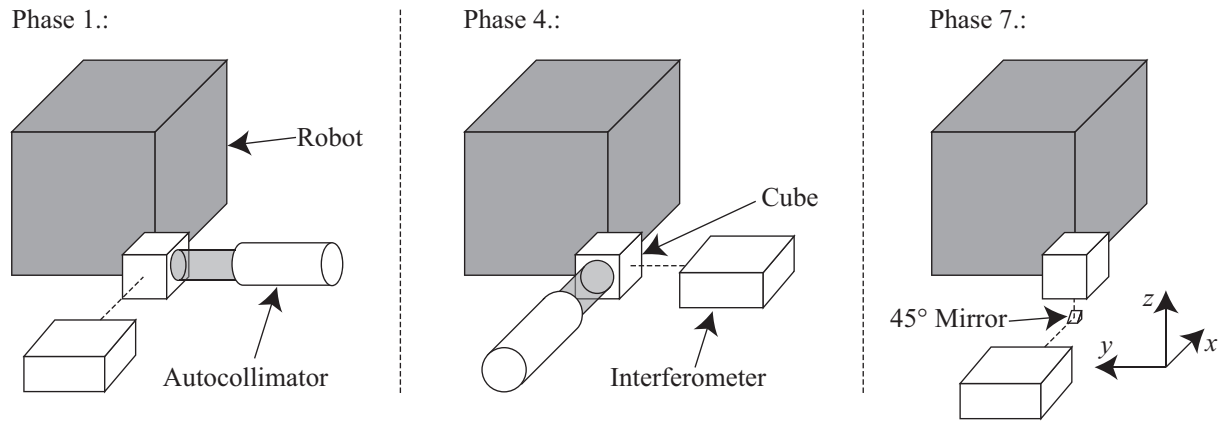
Figure 2.3: *The three measuring devices configurations for the Delta Cube 2.*

5. Thermal stabilization.

6. Measure along y, θ_x and θ_y.

7. Interferometer mounted along z axis.

8. Thermal stabilization.

9. Measure along z.

10. Merging of the the different measures to build a 6 DOF measure dataset for calibration.

Using this procedure is effectively possible to measure the 6 DOF pose of the robot end-effector at ultra-high level of precision. Nevertheless, this procedure has the following draw-backs:

- Before starting each measuring session, a thermal stabilization of the system has to be performed. The measure can be performed only when the robot temperature is stabilized to $25.00 \pm 0.01°C$. This operation is time demanding, in fact it takes 8-10 hours.

- To change the configuration of the measuring devices, the insulated box has to be opened, and the thermal stabilization has to be performed again. Consequently, 3 thermal stabilizations are needed to acquire a complete dataset of poses.

- The overall measuring procedure is extremely time consuming, making it not suitable for industrial applications. In fact, with an evaluated measuring session of 28 hours[2], the taking off, setting up and alignment of the measuring devices estimated to 30 min-utes and a thermal stabilization session evaluated to 9 hours (an average time), we ob-tain a total measuring time of $3 \cdot (0.5 + 9 + 28) = 112.5$ hours, *i.e.* ~4.5 working days of 24

---

[2]The author claims to measure 6859 end-effector poses. Thus, considering a waiting time of 10 seconds between each displacement, and 5 seconds to collect the measure and displace the robot to the next position, we obtain $6859 \cdot 15 = 102885$ seconds of total measuring time, that is ~28 hours.
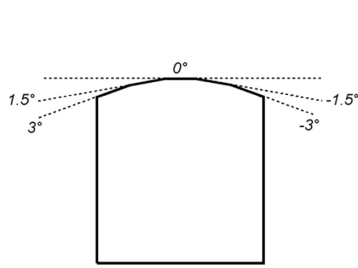
Figure 2.4: *The different orientations of the prism's facets.*
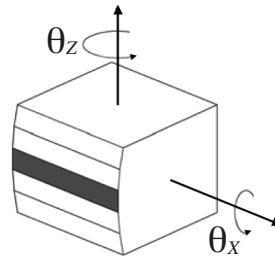
Figure 2.5: *The prism oriented to measure ±3° rotations around θ_X axis.*

Figure 2.6: *The end-effector of the Sigma6 with the mirror cube and the sphere..*

hours. Such amount of time increases if we consider that the process is not automatic: a human operator has to be present when phases 3 and 6 are terminated to perform the adjustments of points 4 and 7. Therefore, an additional time must be added if those phases finish when an operator is not available (*e.g.* during the night or weekend).

2.1.2.2   Sigma6

Due to the major complexity of this case[3], a second LDS-1000 Autocollimator and 3 *Keyence Laser Triangulation Displacement Sensors* have been added to the set of measuring devices. In this case, the procedure to obtain the 6 DOF data for the calibration is even more complex than for the Delta Cube 2. In addition, some intermediate calibrations are performed before obtaining the final data. In comparison to the Delta Cube 2, the following modification have been performed:

- The autocollimator course is significantly smaller than the rotational course of the Sigma6. To enlarge the measuring capability of the autocollimators, three mirror prisms have been manufactured (Figures 2.4 and 2.5). Each of them is used to measure larger rotations only around one axis. Those prisms will be mounted alternatively to the mirror cube on the robot end-effector to allow reading larger rotations around the three axes.

- A steel-polished sphere is mounted on the end-effector, to define the robot's center of rotation (Figure 2.6).

The author has applied the following procedure to acquire the 6 DOF dataset used for calibration:

1. Calibration of the robot angular motions:

---

[3]The translation courses of the Sigma6 are in the same order of magnitude of the Delta Cube 2 ones, but in this case the rotation courses are ±3° around the three axes

(a) The cube is mounted on the robot end-effector. The two autocollimators are mounted to measure the rotations around the three axes. A thermal stabilization is not needed while measuring rotations.

(b) Measure of θ_x, θ_y and θ_z, for angles between ±400".

(c) The prism for measuring θ_x is mounted in place of the cube.

(d) Measure of θ_x, for angles between (-3°, -1.5°, 1.5°, 3°)±400".

(e) The prism for measuring θ_y is mounted in place of the cube.

(f) Measure of θ_y, for angles between (-3°, -1.5°, 1.5°, 3°)±400".

(g) The prism for measuring θ_z is mounted in place of the cube.

(h) Measure of θ_z, for angles between (-3°, -1.5°, 1.5°, 3°)±400".

(i) The measures acquired in (b), (d), (f) and (h) are merged.

(j) A rotation calibration model is established using the dataset built in (i).

2. Calibration of the robot translation motions, using the model found in 1.(j):

(a) The cube is mounted on the robot end-effector and the interferometer is mounted along x axis.

(b) Thermal stabilization.

(c) Measure of x.

(d) Interferometer mounted along y axis.

(e) Thermal stabilization.

(f) Measure of y.

(g) Interferometer mounted along z axis.

(h) Thermal stabilization.

(i) Measure of z.

(j) The measures acquired in (c), (f) and (i) are merged.

(k) A calibrated model to perform "pure" translations is found using the dataset found in (j).

3. Obtaining the full 6 DOF data (the robot here is displaced using both model found in 1.(j) and 2.(k)):

(a) The cube is substituted with a weight used to simulate the cube's center of mass; the Keyence Orthogonal system is mounted to measure the sphere position (Figure 2.7).

(b) For 33 rotation centers, the following actions are performed:

    i. The robot is displaced to a center of rotation and the Keyence system is adjusted to read its position.
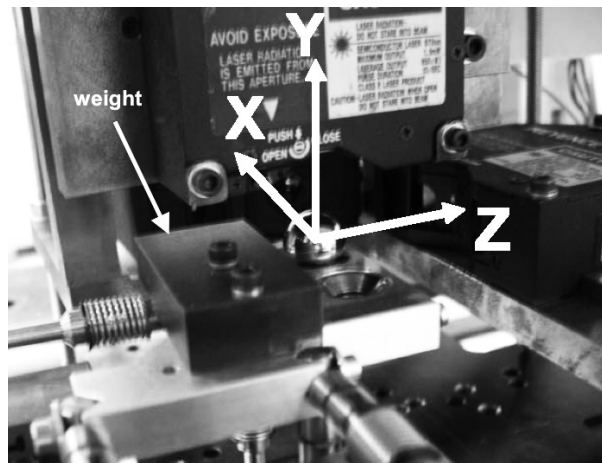
Figure 2.7: *The Keyence Orthogonal system. The weight is set on the end-effector instead of the mirror cube.*

    ii. Thermal stabilization.

    iii. The robot performs rotations around the center of the sphere. The Keyence system is used to correct the parasitic translations in closed-loop.

  (c) The positions of "pure" rotations found in (b) are used to build the final 6 DOF dataset used for calibration.

With this tricky procedure it is possible to acquire 6 DOF ultra-high-precision measures, even if the available measuring devices lack in course. Nevertheless, this procedure has the following drawbacks:

- As for the case of the Delta Cube 2, 8-10 hours are needed to perform each thermal stabilization.

- In this case, 36 thermal stabilizations are needed (zero for point 1, 3 for point 2 and 33 for point 3).

- Mounting alternatively the mirror cube, three mirror prisms and the weight changes the position of the end-effector center of mass and the weight of the end-effector. At nano-scale these changes have a significant influence on the robot geometry. When merging the dataset obtained with such different mountings, this will introduce an error in the measure.

- The amount of time to collect the 6 DOF data for calibration is enormous. We estimate:

    – Point 1: 47 hours[4] for point 1.(b); 15 hours[5] for each measuring phase involving the prisms (1.(d), 1.(f), and 1.(h)). Thus the dismounting, setting up and alignment

---

[4] The trajectory file used for this phase is composed of 11319 points. Considering a waiting time of 10 seconds between each displacement, and 5 seconds to collect the measure and displace the robot to the next position, we obtain $11319 \cdot 15 = 169785$ seconds of total measuring time, that is ~47 hours.

[5] In this case 3564 points have been measured. Considering a waiting time of 10 seconds between each

of the measuring devices estimated to 30 minutes and a thermal stabilization session evaluated to 7 hours (an average time), we obtain a total measuring time of $0.5 + 9 + 47 + 3 \cdot (0.5 + 9 + 15) = 130$ hours, *i.e.* ~5.5 nonstop working days.

- – Point 2: 3 hours[6] for each measuring session. Again, the dismounting, mounting and alignment of the measuring devices estimated are to 30 minutes and a thermal stabilization session is evaluated to 9 hours (an average time). Thus, we obtain a total measuring time of $3 \cdot (0.5 + 9 + 3) = 37.5$ hours.

- – Point 3: 4.5 hours for each center of rotation closed-loop of point 3. With half an hour for the alignment of the Keyence system and a thermal stabilization of 9 hours we obtain $33 \cdot (0.5 + 9 + 4.5) = 462$ hours, *i.e.* ~19 24-hours working days.

A total time of ~26 nonstop working days is estimated without considering the computational time of the two intermediate calibrations. Furthermore, an extra time must be added for the cases in which the human operator is not available for switching the measuring devices. For this reason this process is completely out of any possible industrial application.

2.1.3 Data Processing

Once the data is acquired, two kinds of model correction have been tested:

- • *Model-based* approach,

- • *Model-free* approach.

In the model-based approaches, the IGM of the robot is used, and only the positioning error is modeled. The function found in this way will be used to compensate the error generated by the IGM.

On the contrary, in the model-free approaches, the IGM of the robot is ignored, and a new relationship between measured end-effector coordinates and motor coordinates is found from scratch.

In both cases, several simulations have been performed in order to compare different data-fitting techniques, *i.e.* Neural-networks, Parameters research, Genetic Algorithms and Splines interpolation. Thus, the author proposes a tree-based technique to find the "optimal" Neural Network structure to be used to solve a particular calibration problem [28].

The result of such comparison is that all of those techniques are capable of fitting the data in the same way, with or without the help of the IGM. The mathematical tool used for modeling is not the crucial technique (in the end all the methods are different abstractions

---

displacement, and 5 seconds to collect the measure and displace the robot to the next position, we obtain $3564 \cdot 15 = 53460$ seconds of total measuring time, that is ~15 hours.

[6]729 poses are measured in this case. Considering a waiting time of 10 seconds between each displacement, and 5 seconds to collect the measure and displace the robot to the next position, we obtain $729 \cdot 15 = 10935$ seconds of total measuring time, that is ~3 hours.

of a parameters research), on the other hand it is very important to acquire high-quality measurements.

Unfortunately, the author does not explicitly declare the computational cost of every calibration technique employed. As the author claims that all of them are effective, a time comparison would have been interesting to define which one has the lower time cost.

For future comparison with the algorithm used in the current thesis, parameter research and Neural Network time costs have been evaluated:

- For the parameter research, a duration of ~4 hours has been evaluated for the *Delta Cube 2* robot; a duration between 16 and 24 hours has been evaluated or the *Sigma6*.

- Regarding the Neural Networks, the training of a single Neural Network is evaluated between 2-3 hours for the *Delta Cube 2* and 8-10 hours for the *Sigma6*. Furthermore, the research of the "optimal" network took at least 8-10 iteration to find the best network. This means that in the best of the cases, the Neural Network that better fits the geometry of the *Delta Cube 2* is found and trained at least in 16 hours, while for the *Sigma6* the amount of time needed is in at least 64 hours [52].

2.1.4   Calibration Results

For each robot, the calibrated model has been inserted in the robot controller and used to displace the end-effector in some positions. The error in positioning is measured and calculated considering a confidence interval of 90%, equivalent to 1.645σ.

Regarding the *model-based* approach the author obtained:

- For the *Delta Cube 2* a final accuracy in translation of ±100 nm.

- For the *Sigma6* a final accuracy of ±120 nm has been obtained performing "pure" translations. For translations coupled with rotations the accuracy decreases to ±400 nm.

- For the *Sigma6* again, a final accuracy of ±0.36" has been reached for angles between ±400". A final accuracy of ±3" has been reached for angles between (-3°, -1.5°, 1.5°, 3°)±400".

Regarding the *model-free* approach the following accuracies have been measured:

- For the *Delta Cube 2* a final accuracy in translation below ±100 nm.

- For the *Sigma6* a final accuracy of ±120 nm has been obtained while displacing along "pure" translations. For translations coupled with rotations the accuracy decreases to ±600 nm.

- For the *Sigma6* again, a final accuracy of ±0.33" has been reached for angles between ±400". A final accuracy of ±2.7" has been reached for angles between (-3°, -1.5°, 1.5°, 3°)±400".

2.1.5   Nano-Indentation

Nano-indentation is a procedure classically employed to evaluate the hardness of metallic materials. In Dr. Fazenda's thesis, this process has been adapted to measure the accuracy reached by the robot after the calibration process: this is done by engraving several marks at a well-known distance over a substrate, thus measuring their distance using an alternative measuring device.

To produce the marks over the substrate, a diamond with a pyramidal shape (Vickers) is mounted on the robot end-effector. A mirror polished Invar® substrate is mounted in proximity of the diamond, over a force sensor.

To perform nano-indentation, the robot performs "pure" translations. At the beginning an alignment of the substrate with the robot frame is performed. After that, 5 marks are engraved in the substrate (the first will be the reference). The contact is detected using the force sensor and the robot performs steps of 250 nm to attain the substrate surface.

The measure of the relative distance of the indents has been performed using a Raith 150 electronic microscope. This table inside the microscope is displaced with a resolution of 1 nm. Before performing the measures, the microscope is calibrated using a "standard" positioned near the substrate. Finally, the position of the indents is measured and their error is evaluated to ±300 nm.

2.1.6   Summary on LSRO Work

The calibration of two ultra-high-precision robots was achieved, and a final accuracy around ±100 nm was reached for both of them. The drawbacks of the calibration procedure proposed in [27] are the following:

- The measuring phase is too time-consuming.

- Thermal stabilization of the robot environment allows for calibration of the robot but it does not allow *the use* of the calibrated robot in an unsteady environment. The accuracy of the robots calibrated with this technique is kept under the ±100 nm only while the environmental temperature is 25.00 ± 0.01°C.

- As a consequence of the previous point, this calibration technique compensates only for the *geometric errors* of a robot.

- Of the 11 thermal sensors employed in the measuring setup, only one is used actively. 10 readings are collected but in fact not used.

- Thermal stabilization is too time consuming. From an industrial point of view, it is too expensive to wait 8-10 hours for thermal stabilization for each piece that has to be manufactured.

- The data processing to obtain the calibrated model is too time-consuming and a complete evaluation of the time cost of the proposed calibration algorithms is missing.

- Regarding the computational time of a Neural Network calibrated model, for its complexity it is not possible to use it in a real-time process to control the robot position.

- Industrial partners express their lack of confidence in the use of black-box calibration methods.

2.2 Ultra-high-precision Measurement

We introduce here some relevant solutions that other researchers have adopted to measure a robot pose at ultra-high-precision. In this survey we narrowed our study to contactless measuring devices - especially interferometers - with ultra-high-precision capabilities.

There are two ways to achieve 6 DOF ultra-high-precision measurements with contactless devices:

- *Laser tracking systems*: an interferometer is used to produce a laser beam. This beam passes through a beam steering mechanism and finally hits a mirror positioned on the robot end-effector. When the robot moves, the beam steering mechanism will move as well, in order to keep the laser pointing on the end-effector. In this way, the beam will always be reflected back in the measuring device and treated to extract the measurement information. Some part of the measuring information also comes from the beam-steering mechanism that has its own angular encoders. This system has been used in [66, 85] to measure the 6 DOF pose of a robot end-effector (Figure 2.8).

- *Interferometers and autocollimators*: in this case the measuring devices are mounted directly towards the robot end-effector. The end-effector is equipped with standard mirrors or corner cube mirrors, in order to allow the reflection of the laser beams. This system has been used in the works [50, 67] to measure the 6 DOF pose of a robot end-effector, and in [43] to measure the 5 DOF pose of a linear stage.
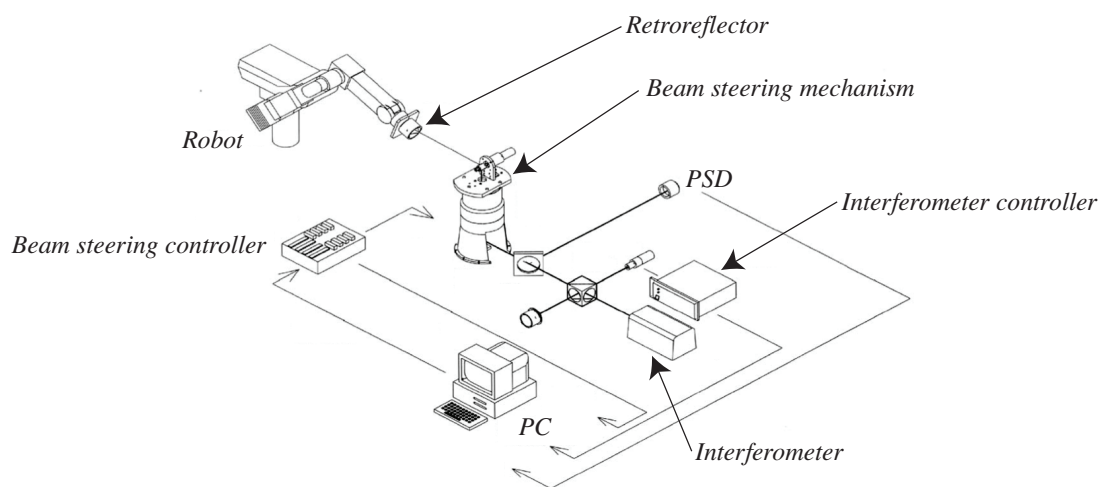
Figure 2.8: *The 6 DOF laser tracking system described in* [85].

Furthermore, in the article [41] the principles and the basis of heterodyne and homodyne interferometry are discussed. The abbe error is introduced as well as the commercial SIOS® interferometers that will be used in the current thesis. Thus, the Nanopositioning and Nanomeasuring machine (presented previously in [53]) is introduced as well. This machine (now commercialized by SIOS®) has a resolution of 0.1 nm and a measuring range up to 25 mm × 25 mm × 5 mm.

Because of its principle of operation the interferometer is very sensitive to thermal variations in the environment (refer to the Appendix for the interferometer's working principle). To avoid errors caused by this effect, two families of solutions are proposed:

- *High-precision thermal stabilization of the environment*: this technique, exploited also in [27], consists in mounting the robot and the measuring devices in a chamber or a box insulated from the rest of the environment, and controlling the air temperature in it. This technique has been recently used in [25] obtaining a steady air temperature of 20±0.007°C. Older works related to this topic are [17, 24, 44, 45, 74]. To conclude, notice that with this technique the interferometer drift is limited, but before performing the measurement it is necessary to wait a long amount of time to allow the air temperature stabilization.

- *Model and compensation of the drift*: by using this technique, the measurements of the interferometer are corrected in real-time while the external factors are changing and acting on the device. There are two possible ways of compensating this error:

  - By *measurement*: this technique has been used in [38]. Here, the interferometer beam is split and used to measure the position of a fixed reference. The drift on the measuring reference is evaluated and used to correct the real measurement of the interferometer (this technique is explained in detail in 3.2.1.3 on page 40).
  - By *modeling*: in the article [22], a brilliant way of compensating the air environmental drift is proposed. Along the path of the laser beam there are many thermal sensors used to monitor the air temperature (that is proportional to the air refraction index), the air pressure and the humidity (Figure 2.9). By using the read-outs of those sensors, the author developed a mathematical model to compensate the drift caused by the environment thermal changes.

The autocollimator is insensitive to thermal variation: in other words, air refractive index changes do not cause a drift of the measure. Furthermore, as seen in [27], as soon as the robot arms and the supports holding the system are built with materials with the same expansion coefficient, and their temperatures change in the same way, the robot will drift without forming angles.

Summary

- There are essentially two ways of acquiring 6 DOF ultra-high-precision measurements without contact: by laser tracking system or by mounting the instruments directly towards the end-effector.
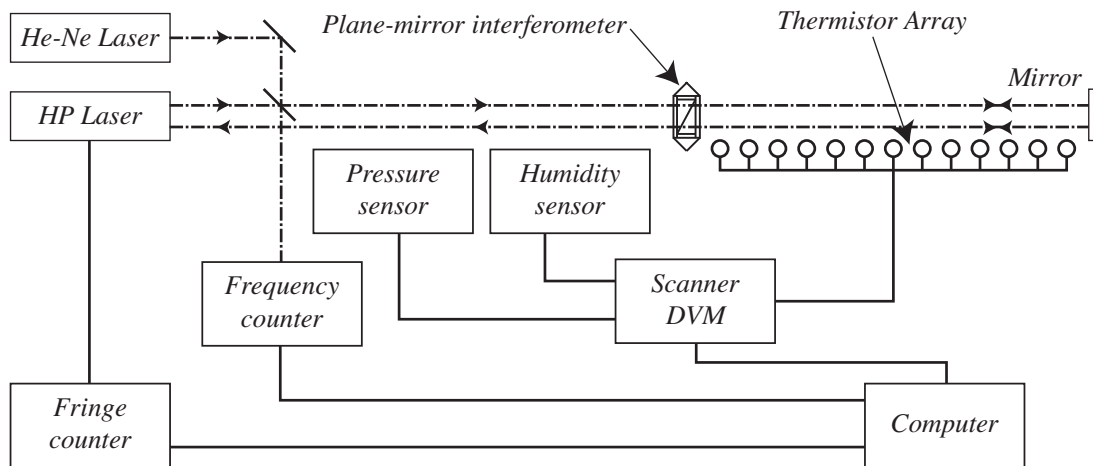
Figure 2.9: *Schematic diagram of the interferometer system proposed in* [22].

- Laser tracking systems are suited for high-precision measures and *not* for ultra-high-precision measures, in fact the beam steering mechanism introduce a considerable measuring error. This technique has anyway the advantage of having a bigger measuring volume.

- Instruments mounted directly towards the end-effector represent a good solution for ultra-high-precision measures. The drawback of this technique is the limited measuring volume.

- Interferometers suffer from environmental thermal variations. There are principally two ways of dealing with this problem: by insulating the measuring setup and stabilizing the air temperature in it or by identifying the drift and compensating for it.

2.3 Sources of Inaccuracy Compensation

We introduce here the most significant sources of inaccuracy for ultra-high-precision robots. In the literature they are classified in this way [68, 69]:

1. Thermal effects.

2. External forces acting on the robot.

3. Incertitude in the reference / use of multiple robots.

Here we will introduce how other authors in the past have dealt with them.

2.3.1 Thermal Drift

It is well known that temperature rise causes thermal expansion of an object and may induce internal stresses and deformations in the object when it is subject to constraints. In the case of robots and machine tools, such deformations are the cause of the so-called *thermal errors*.

In the article [46] the authors introduce the state of the art on works done on thermal-error modeling. They propose a classification of the ways of modeling thermal errors:

1. *Principle based* models, in which the relationship between thermal errors and heat generated are described by a system of non-linear differential equations. The solutions to those equations are found in two ways:

    (a) Through *analytical* models: in which the thermal behavior of the system is calculated using a physical description of it [11].

    (b) Through *numerical* models: in which a model of the thermal drift is established using simulation software (Newton-Rapson in [33], Ansys® in [90], and Finite Element Method in [77]).

2. *Empirical based* models, based on the assumption that thermal errors can be considered as a function of some critical discrete temperature points on the machine. Those models can be divided in two categories:

    (a) *Static* models: established on the basis of information at one isolated point in time. They can be found in two ways:

        i. *MRA*[7] *models*: the thermal error is described by the sum of the thermal reading multiplied one by one for a different coefficient. Coefficients are usually determinated using a least square method. In this way the relationship between thermal errors and temperatures is established [75, 80].

        ii. *Artificial Neural Networks*: used to easily correlate thermal error and temperatures in a multiple-input and multiple-output form. They have been used in the works [9, 34, 76, 81, 86, 94]. Moreover Support Vector Machines, an alternative ways of using Neural Network that gives more generalized solution, have been used in [70].

    (b) *Dynamic* models: based on the concept that not only the information at the present time is useful to describe the behavior of the system, but also the information at previous times. Those can be modeled using two techniques:

        i. *Common dynamic* models, such as recurrent neural networks and integrated recurrent neural networks (both used in [95]), grey dynamic models [91] or complex multi-variable regression analysis models [49].

        ii. *Adaptive dynamic* models: redefined according to continuous changes of operation status of the model (auto-regressive model [47]).

Principle based and Empirical based models have they own drawbacks.

For the first, it is challenging to build a principle-based model that accurately describes a heat source model and a heat transfer model of all the parts of the system.

For the second, the challenge comes from the fact that training an empirical-based model requires a large number of data-pairs of temperatures and thermal errors along with the patterns of working conditions. Thus, the data acquisition process can be very time consuming.

---

[7]MRA: Multiple Regression Analysis

Summary

In this sub-section we introduced all the ways of dealing with thermal errors on robots and machine tools. The research works cited here refer to systems working with precision between 1 mm and 1 μm. To the best of our knowledge, we did not find any previous work on ultra-high-precision robot thermal compensation.

2.3.2 External Forces

In this section we introduce the forces acting on a robot that induce deformations of its geometry. In the literature there are two:

- *Cutting-forces*: generated by the manufacturing process performed by the robot. If the recoil or the forces generated by the process are significant, they can cause the deformation of the robot structure. In [93], cutting-force effects are compensated in real-time on a turning center. The authors used a force sensor to measure the cutting-forces. A model of the error caused by them was established and implemented in the robot controller. To conclude, in the paper [51], the principal ways of measuring and controlling force in micromanipulation are explained.

- *Gravity*: during robot usage its arms can assume different orientations and positions in space, depending on the pose reached by the end-effector. Gravity will deform the robot arms differently depending on this pose. For this reason, gravity has to be taken into account in the calibration process. Gravity effect can be modeled as an external force acting on the robot as it was done in the works [12, 18, 61].

Summary

The force compensation topic is less treated in the literature than the thermal compensation. This is due to the fact that for ultra-high precision applications most of the time force effects are negligible in comparison to the effects caused by thermal drift.

2.3.3 Thermal Drift and External Forces

In some works, the techniques seen until now have been used to compensate both effects at the same time:

In [96], thermal errors and grinding force errors are modeled and compensated on a Precision NC Cylindrical Grinding Machine. The authors used Neural Network to model the behavior of the robot. By using this technique, the radial error of the grinding machine has been reduced from 27 to 8 μm.

A comprehensive geometric, thermal and cutting-force error compensation system has been presented in [48]. This system uses thermistors to measure several temperatures of the system, while a piezo-electric force sensor is used to measure the cutting force. A parametric model was established to describe the robot behavior and the error was reduced from 31 to 5 μm.

Summary

The two effects can be treated using the same technique: it is sufficient to add the parameters regarding the force measurement into a thermal compensation model to compensate the cutting forces. To the best of our knowledge, few works have been done on this topic.

2.3.4   Reference Incertitude and Multiple Robots System

In this subsection we consider works related to issues based on reference incertitude:

- We define *reference incertitude* as both the incertitude in relating the measuring frame to the end-effector tool-tip frame and the incertitude in relating the work piece frame to the end-effector tool-tip frame. This issue is discussed in the articles [5, 6] (from the same author). In these works a solution is proposed: the frame of the work piece is defined towards the tool-tip frame in the moment when the first cut is done. Furthermore a camera equipped with a telecentric objective is used to measure the positioning offset with a resolution of 0.465 μm.

- *Multiple robots system referring* is the incertitude in relating a robot frame towards a second robot frame. This issue has been treated only for macro industrial robots in [7, 29, 57].

Summary

Though reference incertitude has been studied for ultra-high levels of precision, this is not true for the multiple-robot systems referring.

2.4   Conclusions

The conclusions that have to be retained from this chapter are the following:

- To our knowledge and if we do not consider the work done in our laboratory, there is little work on ultra-high-precision robot calibration available in the literature.

- External effects acting on robots have not been studied at levels of accuracy under the micron.

- A complete ultra-high-precision 6 DOF measuring system has never been developed.

- There are no works in the literature that treat the problem of multiple ultra-high-precision robot system calibration.

Chapter 3

A Novel Robot Calibration Procedure

The calibration procedure seen in section 1.3 on page 9 is capable of compensating only for the *geometric errors* of the robot. Therefore, it is effective only for cases where the desired final accuracy is limited to 1-10 μm, depending on the robot characteristics. In fact, as we have seen in section 1.1, at sub-micrometric scale physical effects and other sources of inaccuracy start playing a dramatic influence on the robot, deforming its geometry in a non-linear way.

Therefore, to reach a nanometric level of accuracy it is necessary to keep in account such external effects in the modeling of the robot geometry. This is carried out by quantifying such sources of inaccuracy while measuring their effect on the robot geometry. A mathematical function describing the interaction between the sources of inaccuracy and the robot geometry is then established. To allow their compensation during the robot use, it is necessary to measure them constantly and use this measure to predict and compensate for their influence on the robot geometry (Figure 3.1).

We have integrated this core concept into the classic calibration algorithm, establishing the following *new calibration procedure for ultra-high-precision robots*:

Step 0: A *judicious design of the robot* that takes into account the calibration problem and the pose measurement,

Step 1: *Study of the sources of inaccuracy* linked to the robot and the industrial process that it will perform,

Step 2: *Measurement* of several end-effector poses,

Step 3: *Identification* of a function that describe the robot geometry and its behavior when subjected to the sources of inaccuracy identified in *Step 1*,

Step 4: *Implementation* of the model found in *Step 3* into the robot controller,

Step 5: *Validation* (evaluation of the robot absolute accuracy) and if necessary return to *Step 1* (if the desired absolute accuracy has not yet been reached and some sources of inaccuracy have still not been considered) or return to *Step 0* (if all the possible sources of inaccuracy have already been considered).

While *Steps 0, 1* and *5* are original, *Steps 2* and *4* remain equal to the ones from the classic procedure[1]. Furthermore, *Step 3* is the fusion of *Steps 1* and *3* of the classic calibration procedure. The calibration models obtained with the classic calibration procedure and the new one are different. In fact, the model obtained with the new procedure describes the geometric model, the geometric errors and the behavior of the robot when subject to sources of inaccuracy. The procedure is summarized in the flowchart in Figure 3.2 on the next page.
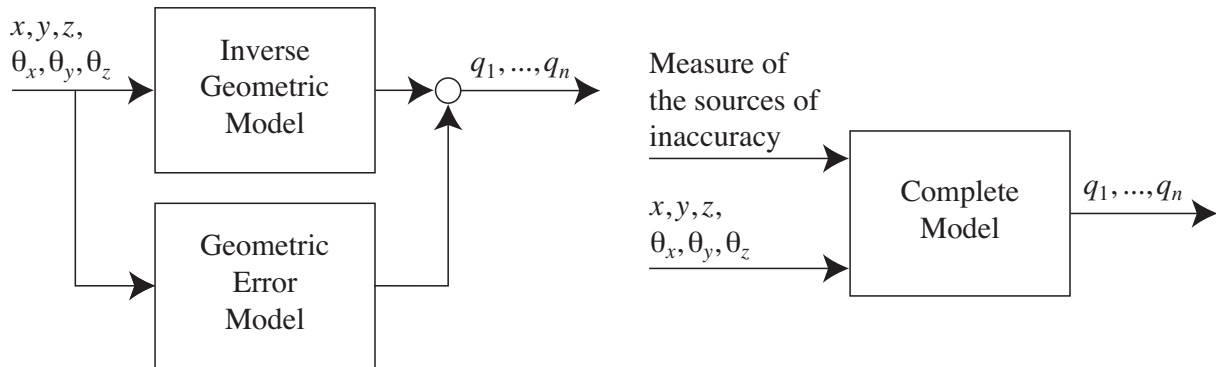
Figure 3.1: *Comparison between the scheme blocks of classical calibration (left) and new calibration (right).*

In the following sections all the steps are described in detail.

3.1   Step 0 - Judicious Robot Design

Firstly, we want to precise that this thesis does not deal with robot conception. Several PhD theses have been written on this subject in our laboratory [2, 39, 60, 62, 64, 78]. To complete them, we will cover some aspects of calibration that must be considered during the robot design.

In fact, we believe that it is not a good attitude to split the problem of robot conception from the problem of calibration. Both have to be considered at the same time, in order to avoid cases where it is not possible to calibrate the robot for issues coming from the design phase (*e.g.* cases where the end-effector is covered or hardly reachable by the measuring instruments, or cases where parasitic DOF do not allow the use of certain measuring devices).

---

[1]Comparison between the steps of the classic calibration procedure (section 1.3 on page 9) and the ones of the new calibration procedure proposed in this thesis:

Classic calibration steps:	New calibration procedure:
Step 1: Modeling,	*Step 0*: Wise robot design,
Step 2: Measurement,	*Step 1*: Inaccuracies study,
Step 3: Identification,	*Step 2*: Measurement,
Step 4: Implementation.	*Step 3*: Identification,
	Step 4: Implementation,
	Step 5: Validation.
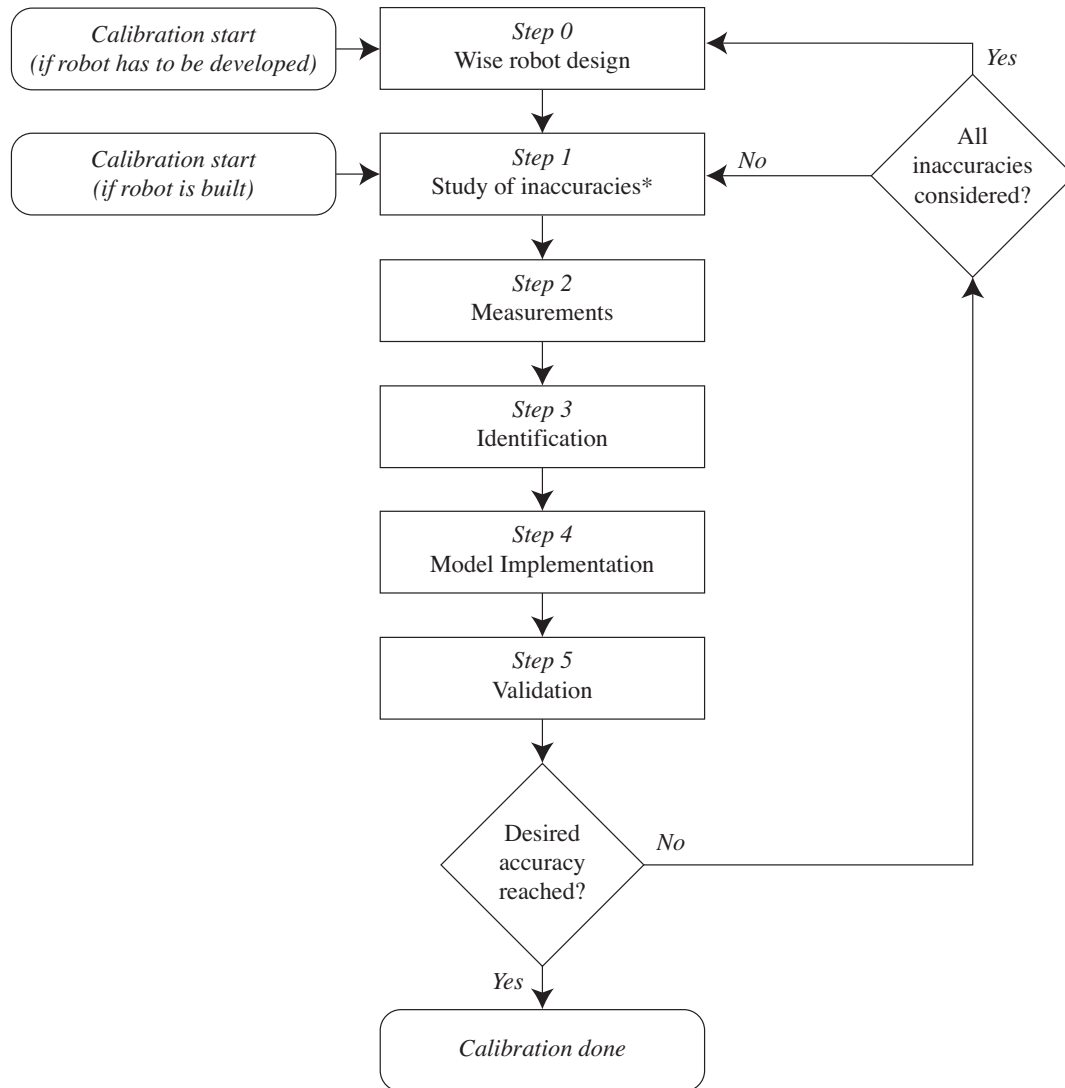
*: Part of the sources of inaccuracy study has already been considered in the design phase.

Figure 3.2: *Flowchart of the calibration procedure developed in this thesis.*

3.1.1   Desired Final Accuracy of The Robot

The most important parameter that a robot designer has to keep in mind during the development of a robot is indeed the desired robot accuracy. This parameter is directly linked to the industrial process the robot will perform, as it will limit its accuracy.

Therefore, it is the "point of departure" for all reflections about:

1. Choice of materials for the robot structure, type of kinematic, type of joints, type of motors and sensors (and their position),

2. Choice of the measuring devices that will be used for calibration (and their position).

Regarding point 1, we have already shown in sub-section 1.2.4 on page 8 the techniques used in our laboratory to develop ultra-high-precision robot. To deepen this subject we encourage the reading of some of the previously mentioned works done at LSRO: [2, 39, 60, 62, 64, 78].

Point 2 will be discussed in the next sub-section.

3.1.2   The Measuring Instruments

Here we introduce some guidelines to choose the appropriate measuring device. Then we will show how to choose a good configuration for their mounting and finally we will furnish some empirical ways to evaluate the quality of the measurements.

3.1.2.1   Choice of the Devices

The choice of the measuring devices for the calibration is done considering the desired final accuracy of the robot. Furthermore, it is an advantage to develop a measuring system capable of measuring the end-effector pose in the entire workspace of the robot. It could also be useful to measure the passive DOF of the robot, in order to evaluate parasitic translations or rotations.

During the years of research on calibration in our laboratory, we have developed two rules of thumb to ease the measuring device choice:

1. If the desired robot accuracy is no less than ~1 µm, it is possible to use contact measuring devices. For desired accuracy under the micron it is necessary to use contactless devices.

2. The measuring device must have a resolution at least 10 times greater than the robot sensors.

While the second rule is based on common sense, the first comes from practical reasons: even if in most cases contact measuring devices are cheaper and easier to use then contactless ones, using contact measuring devices for precision under the micron will introduce frictions in the system and local deformations where the contact happens (Hertzian contact stress). This will cause errors in the measurement in the same order of magnitude of the desired measuring accuracy.

The measuring devices used in this work are introduced in section 4.2.

3.1.2.2 Positioning of the Measuring Devices

Once the measuring devices are chosen, the developer has to think of their configuration in the system. The following recommendations are useful especially for laser-based devices.

First of all, we recommend to mount all the measuring devices pointing directly *towards* the end-effector. Using mirrors to reach the end-effector will introduce inaccuracies linked to the reflection (the state of the mirror surface) and to the longer path the beams have to cover.

We encourage the developer to mount the instruments as close as possible to the robot end-effector. The longer the path of the laser beam, the more the measurement will be influenced by changes in the air (changes of temperature, refraction index and humidity).

Laser devices are sensitive to the following aspects: the cosine error, caused by rotations of the mirror used to reflect the beam, and the Abbe error, caused by a misalignment of the beam towards the center of rotation of the mirror (treated in detail in Appendix A.3 on page 133).

It is important to check the features described in the measuring device datasheet like the fastest speed the device can follow, or the maximum rotation that a translation measuring device can handle before losing the signal.

The physical behavior of the measuring devices has to be considered as well. The developer has to question himself on:

- How the measuring system and its supports will react if the environmental temperature changes?

- Is the measuring device too near to heat sources of the system (*e.g.* the robot motors)?

- Is the measuring device sensitive to air refraction index changes, humidity, and other environmental behaviors?

Finally, we suggest to avoid screwing the devices too strongly to the system. Tightening the screws of the device too much will cause mechanical stress in the support that will cause deformation and therefore instability in the measures.

3.1.2.3 Measurement Quality Control

We always use the following strategies to evaluate the quality of the measurements:

- Once the measuring devices are mounted, we measure the robot at rest for a few hours in order to map the evolution of the drift in the measurements. We usually start our measurements for calibration once the instruments are steady (warmed-up).

- During the measurements for calibration, we repeat the measurement of one pose four times. We use those four measurements to calculate the standard deviation of each measurement. This value represents the quality of each measurement.

- Once a line of measurement is finished (typically after the measure of 7-10 points, depending on the trajectory file), we return the end-effector to the origin and we measure

there. The comparison of all the measures in zero will be used to monitor the drift due to thermal changes[2]. Meanwhile, those points are used for calibration too.

3.2   Step 1 - Study of the Sources of Inaccuracy

Depending on the desired level of accuracy of the robot, its application, its working environment and its mechanical and physical properties it is necessary to consider the following sources of inaccuracy seen in section 1.4 on page 12. Each of them has a different effect and amplitude on the robot:

1. *Geometric errors* (caused by manufacturing tolerances and assembly),

2. *Non-geometric errors* (caused by friction, backlash, wear, link compliance, joint encoder offsets and control errors),

3. *Effects linked to robot working conditions* (caused by environmental factors, external forces acting on the robot and incertitude due to the reference system).

Handling the effects linked to robot working conditions is the principal topic of this thesis. In fact, geometric errors are compensated using the classic calibration procedure and the non-geometric errors can be avoided by designing the robot wisely.

In the next subsections we describe them in detail.

3.2.1   Temperature

Thermal drift is one of the major causes of accuracy loss for high-precision robots [69]; at nano-scale, the effects produced by this are even more significant. Variations in the air temperature surrounding the robot will deform it and change its geometry.

Beside calibration, in this work we suggest three ways to manage thermal drift. They can be used at the same time for different parts of the system.

- *Passive*: Use of materials with a low expansion coefficient or partially thermally isolated from the rest of the system or from the environment.

- *Active*: Active thermal stabilization of sensitive parts.

- *Measuring*: The drift of sensitive parts is measured and compensate in real-time.

---

[2]On the other side, in [27] the "return to zero" was used to correct the drift due to thermal changes: the difference between the measure of two "zeros" was subtracted from the measurements between the two zeros. The zero readings are then deleted and excludes from the calibration.

3.2.1.1 Passive Avoidance of Thermal Drift

During the design of the robot and the system for measuring the robot position, it is very important to carefully choose the materials used for all the parts. Reducing the possible thermal drift in this phase will make it easier to use other techniques such as active stabilization and thermal calibration. It is also very important to avoid mixing materials with different thermal expansion coefficients: doing this will cause the structure to deform in a complex non-linear way when temperature is changing.

The materials employed in this work (with their thermal expansion coefficient) are the following [8]:

- *Aluminum* $(21.5 - 23.6 \times 10^{-6} m/mK)$: very good for manufacturing, high thermal expansion coefficient, low density, high-thermal conductivity.

- *Steel Alloy* $(\sim 12.0 \times 10^{-6} m/mK)$: properties variables depending on the kind of alloy. Low thermal expansion coefficient, high density.

- *Titanium Alloy* Ti-6Al-4V $(8.6 \times 10^{-6} m/mK)$: difficult to manufacture, thermal expansion coefficient similar to the one of steel, highly ductile, good strength to weight ratio.

- *Glass* $(\sim 8.0 \times 10^{-6} m/mK)$: used to build the rules of the linear encoders [35].

- *Invar* $(1.6 \times 10^{-6} m/mK)$: easily manufactured as Aluminum, very low thermal expansion coefficient, quite expensive.

- *Fused Silica* $(0.55 \times 10^{-6} m/mK)$: used as a substrate for mirror parts. Relatively expensive, with a really low thermal expansion coefficient [19].

- *Zerodur* $(0.02 \times 10^{-6} m/mK$ at 0-50°C): used for glass/mirror parts. Expensive, thermal expansion coefficient close to zero [83].

If not differently indicated, the robots' moving parts are in titanium, the robots' encoders are in glass, the supports holding the robots are in steel and the measuring devices supports are in aluminum. We overcome the drift of the aluminum supports by actively stabilizing their temperature. This technique employed to do so is introduced in the next sub-subsection.

3.2.1.2 Active Thermal Stabilization

This method is based on the use of an intelligent device to actively stabilize the temperature of one specific part (Figure 3.3) thus eliminating the effects of thermal expansion. In this work it has been specifically used to stabilize the supports of some measuring devices.

It consists of a Peltier Cell (Figure 3.4 and 3.5) and a thermal sensor glued on the object that has to be stabilized. The thermal sensor is connected to a computer (or an electronic device) that regulates the current applied to the Peltier Cell using a PID logic. A set-point temperature is fixed and the system stabilizes in around 30 minutes.

The stabilization of the air used in [27] is also possible but it is not considered in this work, since it is too slow and therefore not suitable for industrial application.
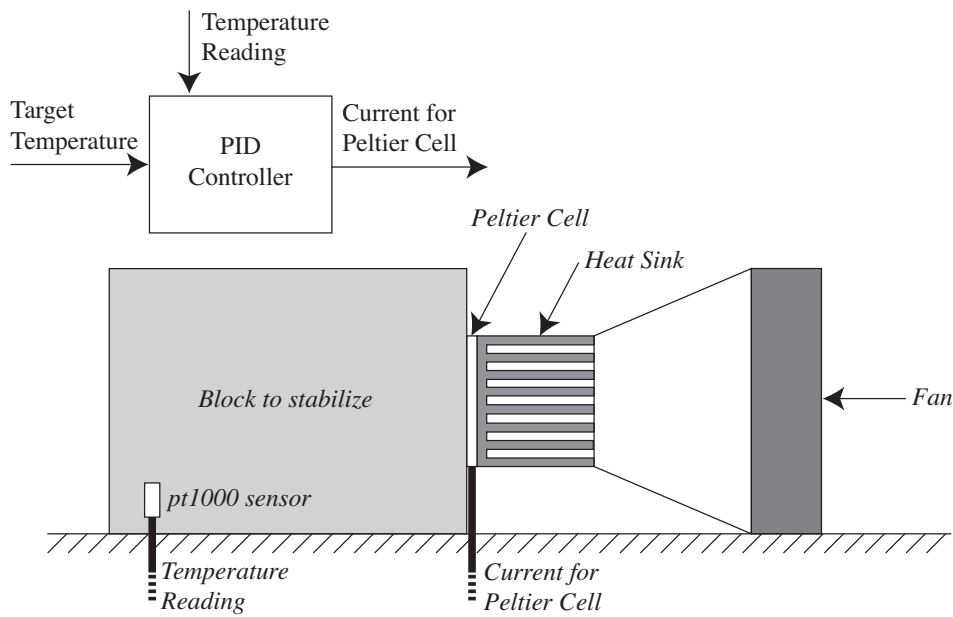
Figure 3.3: *The parts used to perform and control the active thermal stabilization of a piece of material.*
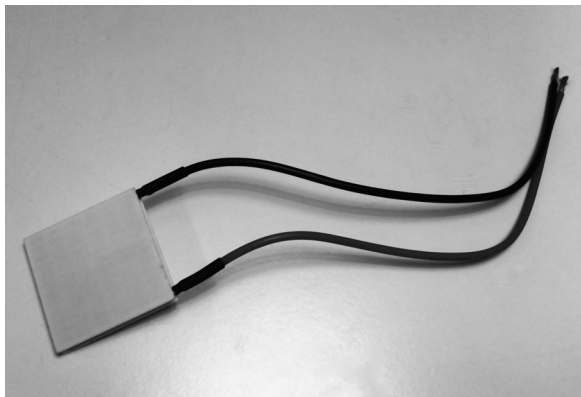
Figure 3.4: *A Peltier Cell.*
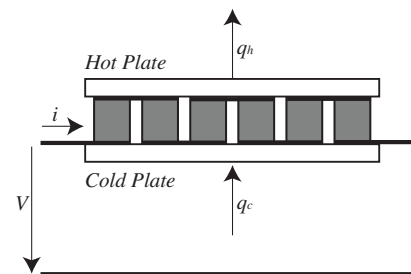
Figure 3.5: *Functional representation of a Peltier cell.*

3.2.1.3 Measuring the Thermal Drift

This solution is implemented using a measuring device with two laser beams or using two single-beam measuring devices. Referring to Figure 3.6, a first mirror is fixed on a non-mobile robot structure part, while a second one is mounted on the end-effector. The beams have to measure the same axis and - for more accurate results - they have to be as close as possible.

Beam A will point to the fixed mirror, while Beam B will point towards the mirror on the robot end-effector. Beam A will measure exclusively the drift caused by thermal effects on the robot structure. This measure will also be influenced by changes in the refraction index in the beam path air.
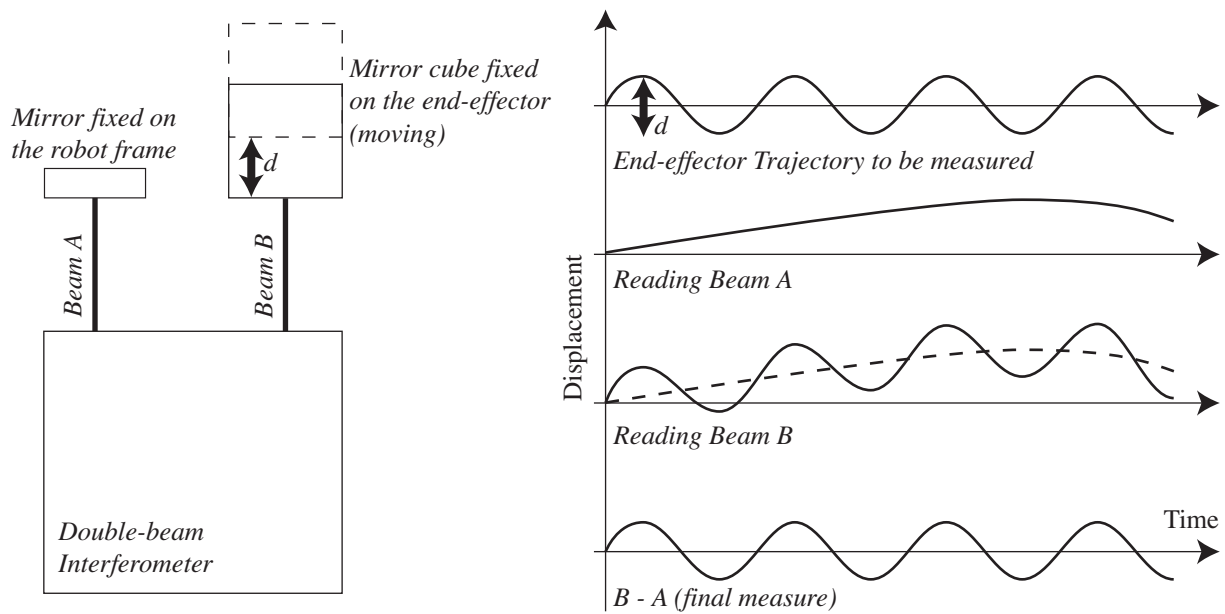
Figure 3.6: *Working principle of the double-beam interferometer: Beam A measures thermal drift while Beam B measures the end-effector position and the thermal drift. To obtain the end-effector displacement without drift it is enough to subtract the reading of Beam A from the reading of Beam B.*

Beam B will read the displacement of the end-effector. Thermal effects and changes in the air refraction index corrupt this measure as well. To extract the real end-effector displacement from the Beam B's measure, the measure of Beam A has to be subtracted from it. This is true also in the case in which the measuring device is drifting.

This technique has two drawbacks: first, a double number of measuring beams or devices is needed to measure the same number of DOF of any other technique. Therefore, this technique is the double more expensive. The second drawback consists in the fact that the drift measured with Beam B does not perfectly cover the drift behaviour of Beam A. This is due to the different position of the two mirrors, and to the displacement d of the end-effector (refer again to Figure 3.6). In fact, the changes in the refraction index happening in this zone are not corrected.

3.2.2 External Forces

The forces generated by the manufacturing process can also deform the robot [68]. Their influence in terms of loss of accuracy depend on their order of magnitude and by the stiffness of the robot. As we have seen in the state of the art, by measuring the forces acting on the robot it is possible to model and compensate them in real-time.

In our laboratory some simulation studies about gravity on an ultra-high-precision flexure-hinge parallelogram have been performed [60] (flexure hinges parallelograms are introduced in 4.1.1 on page 52). It deforms in different ways depending on its orientation toward the gravity vector. An effect of this type will be seen in the case in which the parallelogram is rotated around a horizontal axis during use (like for the *Delta Cube 2,* Figure 2.1 on page 18).

Other deformations linked to the gravitational force are the ones due to changes in the position of the center of mass. They can be observed in the following cases:

- *Pick-and-place applications*: the center of mass of the end-effector will move, if the object picked by the robot has a considerable mass. This will cause a different effect of the gravity on the robot structure.

- *Change of the robot tool*: mounting/dismounting or replacing the robot tool will modify the center of mass of the end-effector. In previous work we have seen that an ultra-high-precision robot *must* be calibrated with its tool mounted on it: mounting the tool after the calibration will change the robot geometry enough to invalidate the calibration.

3.2.3   Reference Incertitude

This source of inaccuracy is related to the incertitude in knowing the absolute position of a reference system with ultra-high precision. We categorize the reference incertitude in two classes:

Figure 3.7: *The frames involved in the use of the system. C_A and C_B are the frames used for the pose measurement. T and S are respectively the tool-tip and the substrate frames. L represents the link transformation between the T and S frame.*

- *Internal reference incertitude*: In this case, we refer to the incertitude related to a single robot's system of references. Specifically, the incertitude in knowing the coordinates transformation between the reference used for the measurements and the reference of the end-effector tool-tip (Figure 3.7, transformation from C_A to T).

- *External reference incertitude*: Here we refer to the incertitude in describing the coordinate transformation between the end-effector tool-tip reference and the reference of the working piece (Figure 3.7, the transformation from C_A to S). Moreover, a second external reference incertitude case that we consider is the incertitude in knowing the coordinate transformation of more end-effector references, in the case of multiple-robot systems (Figure 3.7, the transformation L).

As seen in sub-section 2.3.4 on page 32, for the internal reference problem, the only way to handle it is to use another measuring device (*e.g.* a camera or a microscope) to define the transformation between the two references.

For the external case problem, by using contact or the manufacturing process, we will be able to define a relative reference between the robot end-effector and the work-piece reference, or between more robot references.

3.3 Step 2 - Measuring System Development and Measures

As seen in sub-section 3.1.2 on page 36, the measuring devices are chosen in respect of the final required accuracy. The resolution and the accuracy of the measuring devices must be better than the resolution of the robot encoders and the desired final accuracy. Notice that the position/orientation measuring devices are used only to perform the measurement in *Step 3*. On the other hand, all the sensors employed to monitor the sources of inaccuracy (temperatures, forces, etc.) will be active and measuring also during normal robot usage.

While measurement is under way the sources of inaccuracy must be acting on the robot. In this way it is possible to measure their effect on the robot geometry. Thus, it is recommended to measure the pose of the end-effector in the entire workspace, doing a regular grid. This is done both to map the robot behavior in all the robot workspace and also because acquiring regular data makes it easier to locate measurement errors on the measurement plot (in a regular plot such errors are evident - Figure 3.8).

To map the thermal drift it is important to vary the temperatures acting on the robot in the same range of temperatures that the robot will encounter during normal use. For mapping external forces it is important to use a force sensor to evaluate the force vector acting on it. If possible the reading of the force used to control robot actuators can also be used to model the force behavior.
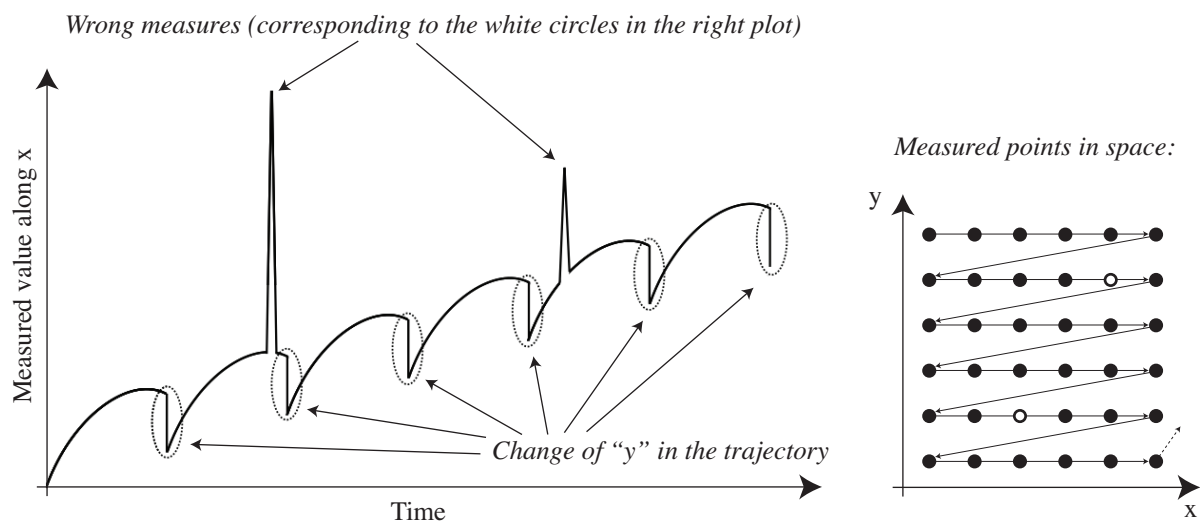
Figure 3.8: *Using a regular trajectory in the measuring of the robot end-effector (plot on the right) allows the visual control of the measurement (plot on the left). In this example, it is possible to identify the points where the measure is wrong.*

Validation Set

To evaluate the final accuracy obtained after the calibration *before* implementing the cali-brated model in the robot controller and repeat new measures, we use the following tech-nique: we acquire a secondary set of measure, called the "validation set" with the only pur-pose to evaluate the capability of the calibrated robot (Figure 3.9).

Logically, also this measuring set has to be acquired while the sources of inaccuracy are acting on the robot, and the sources of inaccuracy have to be measured as well. The points measured for this set must be different from the points used for the robot calibration. None of the measures of the validation set must be done in the same position of the measures used to calibrate the robot.

The validation set can be acquired by displacing the end-effector in a validation point after every calibration points (referring to Figure 3.9, by doing • × • × …), or by measuring all the calibration points then measuring the validation points (by doing • • …• × × …×). Also in this case we recommend the use of a regular trajectory to build the validation set.
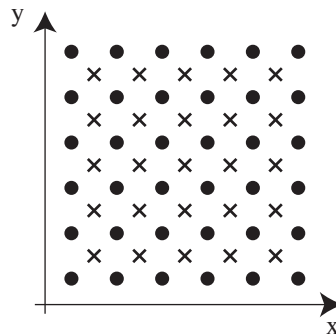
Figure 3.9: *Points used for calibration (dots) and for validation (crosses) in a trajectory file.*

3.4   Step 3 - Kinematic Modeling and Identification

As seen in the classic calibration procedure, modeling and identification are matters that are tackled separately.

Modeling consists in building a mathematical function that describes the DGM or IGM relationship of the robot. To perform this, the developer takes into account the geometrical features of the robot (arm's length, configuration of the links, etc.) to build an ideal geometric model. This operation is complicated, demanding in terms of time and requires a very good knowledge of the robot geometric features. Nevertheless, as such robot description is ideal, it is certainly different from reality. To enhance the prediction capability of the model found in this phase, identification is performed.

Identification consists in finding a mathematical function able to fit the gap between the ideal geometric model found during the modeling phase and the real robot geometry. Identification is the core of calibration, and can be seen as a function approximation or an optimization problem.

As we have seen in the state of the art, it exists plenty of techniques to solve function approximation or optimization problems. As demonstrated in [27], all of them can be employed successfully to perform the identification part of calibration, but often their are complex and time consuming.

In this thesis we will employ an existing parameters research algorithm that has not been considered in [27]: the *Stepwise Regression*. This algorithm – typically employed for statistics purposes – is so effective that allowed us performing the error identification within seconds.

Encouraged by such good results, we decided to test it also to fit the IGM relationship: by using the Stepwise Regression algorithm we have been able to merge modeling and identification problems in a unique function approximation problem, saving a great amount of time (we will exhaustively present the computational costs at the end of each case study, in Chapters 5, 6, and 7) and limiting the complexity of the model. In fact, the algorithm is able to delete the parameters of a model that are not significant to fit the relationship. This is a great advantage, allowing the development of a "light" end effective model suitable for real-time controlling applications. In 6.3.1 on page 79 we use this technique for the first time.

The Stepwise Regression algorithm has two drawbacks: firstly, the algorithm is not able to find the "shape" of the geometric model: it needs a multi-linear model in input. It is only able to find the good coefficient values to fit the model and eliminate the parameters that are useless.

For this reason, it has to be fed with several variables between which it can choose the ones significant for the prediction. The second disadvantage lies in the fact that the solution found with this model is *locally optimal*. This means that it can be possible that the model found in this way is not the "best" in the absolute to describe the robot positioning, i.e. especially when the multi-linear model is too complex, the regression could be stuck in a local minimum.

3.4.1 Stepwise Regression Algorithm

The *Stepwise Regression* algorithm (Matlab®, Statistics Toolbox™ [58]) has the capability of adding or removing terms from a multi-linear model. This is done by comparing the statistical significance of the terms in a regression. The algorithm starts with an initial model that is compared with larger or smaller models. At each step, a coefficient is added to the model and the final error with or without this last coefficient is compared. If there is an improvement in the prediction, the coefficient is kept. Otherwise the coefficient is discarded. For the coefficients that are already in the model the same process applies: if the influence of any coefficient is under a certain threshold, the coefficient is rejected.

Depending on the terms included in the initial model and the order in which terms are moved in and out, the method may build different solutions from the same set of terms. The method terminates when any single step improves the model prediction capability. There is no guarantee that a different initial model or a different sequence of steps will not lead to a better fit. In this sense, stepwise models are locally optimal, but may not be globally optimal.

3.4.2   Stepwise Regression for Calibration

In this sub-section we show how to use the stepwise regression algorithm to perform the modeling and identification phases of a generic case study. For clarity purposes, in this example we do not include yet the compensation of sources of inaccuracy (so only geometric errors are considered).

In the *identification* phase of the classic calibration procedure, a relationship between the measured end-effector coordinates and the error in positioning in motor coordinates is established. We recall here the calibration blocks (Figure 3.10) and the relationship that has to be found to calibrate the IGM (Equation 1.8 on page 11):

$$e_{q_1},\ldots,e_{q_n} = error(x_r, y_r, z_r, \theta_{x_r}, \theta_{y_r}, \theta_{z_r})$$
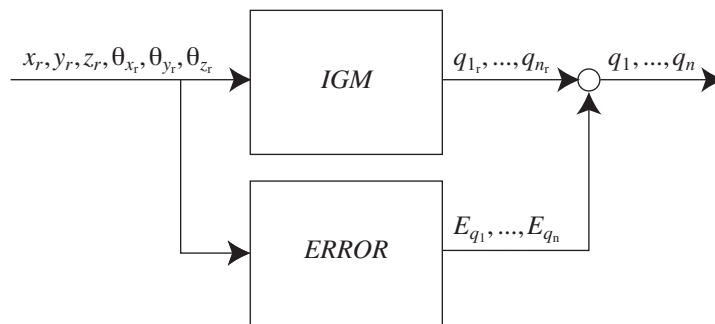
Figure 3.10: *The blocks forming the calibrated model in the classic calibration procedure.*

In our procedure, the Stepwise Regression algorithm finds a direct relationship between measured end-effector coordinates, and the corresponding motor coordinates (Equation 3.1):

$$q_1,\ldots,q_n = model(x_r, y_r, z_r, \theta_{x_r}, \theta_{y_r}, \theta_{z_r}) \tag{3.1}$$

The following procedure is used to build a calibrated model using the Stepwise Regression algorithm, once the relationship between motor coordinates and the corresponding measured end-effector coordinates has been obtained.

1. The relationship 3.1 is divided in n relationships, where n is the number of motors (i is the generic motor coordinate):

$$q_1 = model_1(x_r, y_r, z_r, \theta_{x_r}, \theta_{y_r}, \theta_{z_r})$$
$$\vdots$$
$$q_i = model_i(x_r, y_r, z_r, \theta_{x_r}, \theta_{y_r}, \theta_{z_r}) \tag{3.2}$$
$$\vdots$$
$$q_n = model_n(x_r, y_r, z_r, \theta_{x_r}, \theta_{y_r}, \theta_{z_r})$$

2. As seen before, the Stepwise Regression algorithm is not able to find the mathematical function of the model by itself. For each generic motor coordinate q_i, the user has to provide the algorithm with a polynomial, or a sum of variables, or any possible function that will be multiplied by coefficients. Only after this Stepwise Regression will be able to find the values for the coefficients. For example, a 2nd degree polynomial composed of all the measured DOF of the robot[3] could be built in this case:

$$Q_i = a_1 X_r^2 + a_2 X_r + a_3 Y_r^2 + a_4 Y_r + a_5 Z_r^2 + a_6 Z_r + a_7 \theta_{X_r}^2 + a_8 \theta_{X_r} + \\ + a_9 \theta_{Y_r}^2 + a_{10} \theta_{Y_r} + a_{11} \theta_{Z_r}^2 + a_{12} \theta_{Z_r} + a_{13} \tag{3.3}$$

3. The Stepwise Regression algorithm will find the coefficients $a_1, \ldots, a_{13}$ that fit the relationship created in point 2, by calling the following Matlab function:

$$(a_1, \ldots, a_{13}) = stepwise \left(\left[\left[\begin{array}{c} x_1 \\ \vdots \\ x_m \end{array} \right] \ldots \left[\begin{array}{c} \theta_{z_r 1} \\ \vdots \\ \theta_{z_r m} \end{array} \right] \right], \left[\begin{array}{c} q_1 \\ \vdots \\ q_m \end{array} \right] \right)$$

Where the function inputs are the matrix containing the variables vectors, and the vector of the corresponding motor coordinates. In output the function will give the values of the coefficients $a_1, \ldots, a_{12}$ that fulfill the Equation 3.3. The offset parameter, a_{13}, is calculated after the fitting outside the stepwise algorithm.

4. Points 2 and 3 have to be repeated for each motor coordinate.

5. The calibrated geometric model is formed by the system of equations found in 4.

Considering external sources of inaccuracy is done in this way: a measurement of a source of inaccuracy is treated like any other variable and is inserted in the multi-linear model that Stepwise Regression will have in input. This part of the calibration will be explained in detail for each case study.

From a mathematical point of view, we underline the following concepts:

1. Even if the variables of the multi-linear model are non linear, the model remains linear in the parameters. In fact the variables forming the multi-linear model can be linear (x) or non linear $\left(log \left(x \right) \right)$, or even a non-linear function of a linear variable $\left(x^2 \right)$.

2. In general, to find a unique solution of a system we need the same number of equations (in our case measures) than the number of variables. However, since here we are in the domain of statistics and because of the measuring incertitude, the more measures we use, the better model we find.

Seeing how the algorithm works, one could be tempted to provide the algorithm with a multi-linear model with as much variables as possible, thus hoping that the algorithm would be able to find the good parameters by itself. On the contrary the algorithm will be more likely

---

[3]For clarity purpose, this model does not include second order terms with mixed variables (like $a_i X_r Y_r$)

to be stuck in a local minimum. For this reason, while we are searching for a good equation to fit the system (Equation 3.3) we perform some regression iterations where we gradually augment the complexity of the model, until its prediction is no able to grow anymore. In this way we avoid falling in local minima and we keep the model as simple as possible. During the explanation of the case studies, we will mention the variables that we try to insert in the model, that do not improve the prediction of the model.

3.5   Step 4 - Implementing the Calibrated Model

Here the calibrated model found in the previous step is implemented in the robot controller. This model can be really complex, depending on the number of sources of inaccuracy considered. From a software point of view, robot inverse geometric models are calculated in a real-time process. To speed up its calculation it is possible to detach the thermal coefficient from the rest of the calculations. Thermal variations are very slow, so they can be calculated in a non-real-time process every 5-10 seconds; their contribution can thus be added in the real-time process (Figure 3.11). On the other hand, variations due to external forces must imperatively be compensated in real-time.

If a validation set has been acquired (section 3.3 on page 44), we suggest using it to evaluate the calibrated model accuracy *just after Step 3, before* implementing it in the robot controller. In this way it is possible to have a good evaluation of the model without performing verification measures. In our case studies, we test the model with the validation set automatically just after the Stepwise Regression parameters research. Only the models that have very good accuracy capability are finally implemented in the robot controller.
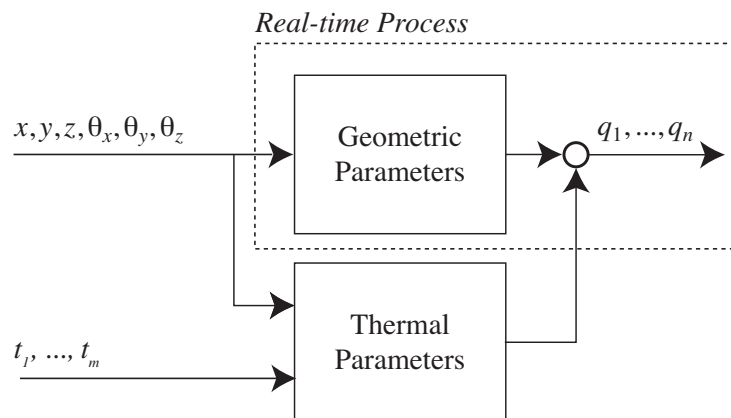

Figure 3.11: *Implementation of a calibrated model in the robot controller. The geometric part of the model is calculated in a real-time process, while the thermal part is calculated in a slower process.*

3.6 Step 5 - Validation and Closing the Loop

In this step the calibration is validated and the final accuracy of the robot is measured. The final accuracy can be evaluated in four ways:

1. *By using the validation set*: the validation set is inserted in the calibrated model and the model prediction is compared to the motor coordinates in the validation set. This is the fastest way to evaluate the capability of a model. The drawback of this evaluation is that the final accuracy is expressed in motor coordinates. As this evaluation does not need any further measurement, it is possible to implement it as a "pre-evaluation" during the execution of *Step 3*.

2. *By implementing the model in the robot controller* (*Step 4*), displacing the robot in some positions and using the calibration measuring system to read the real positions of the end-effector. This procedure provides an evaluation in terms of end-effector coordinates.

3. *By implementing the model in the robot controller* (*Step 4*), displacing the robot in some position and using a *different* measuring system to measure the real position of the end-effector. Even if this solution could seem the most elegant, we want to underline that for several measuring institutes around the world the nanometer could not measure the same [54]. This means that two ultra-high-precision measuring devices coming from two different companies (or calibrated by different measuring institutes) could measure the nanometer in a diverse way. This would cause a systematic error in the calibration evaluation.

4. *By manufacturing a piece with the robot and measuring the accuracy of the work-piece*. The clear advantage of this technique is that not only it evaluates the absolute accuracy of the robot but also the accuracy of the manufacturing process performed by the calibrated robot. The drawback of this validation lies in the fact that if the sources of inaccuracies between the end-effector frame and the tool-tip frame are not evaluated, a systematic error that has not been tackled during the calibration procedure could be measured.

Thanks to the validation, the final accuracy of the robot is evaluated. If it is equal or lower than the desired final accuracy, the robot calibration is terminated. Otherwise, one of the following steps has to be done:

- If some sources of inaccuracy have not yet been considered: return to *Step 1* and consider a new one.

- If all the sources of inaccuracy have been considered: the robot cannot reach the desired accuracy. It is necessary to come back to *Step 0* and reconsider the robot design.

3.7   Conclusions

In this chapter we have introduced the procedure developed to perform the calibration of ultra-high-precision robots while keeping in account external sources of inaccuracies. We have adapted the classic calibration procedure in order to take in account the measure, modeling and compensation of the most significant disturbances acting on the robot. The points that have to be retain from this chapter are the following:

- In the case of ultra-high-precision robots, the problem of calibration has to be kept in account already during the robot design phase.

- The ultra-high-precision measuring problem has to be considered from the beginning as well. Choosing the appropriate measuring devices and compensating the sources of inaccuracy acting on them have a fundamental importance.

- By using the Stepwise Regression and a multi-linear model we are able to fusion the modeling and identification phases. With this approach we are able to find a robot IGM by just having the correspondences between motor coordinates and end-effector coordinates.

In Chapters 5, 6 and 7 we will show how we used this calibration procedure in practice and the results that we have obtained.

In the next chapter we will introduce the robots, the measuring devices and other materials used to perform the case studies.

Chapter 4

Materials

This chapter is divided in four sections. In the first we will present the robots considered to perform the case studies. In the second, we will introduce all the measuring devices used to build the measuring system for each robot. In the third section we will lay out the description of other devices that we have developed to carry out the experiences for this thesis. Lastly we will end this chapter by laying out some conclusions.

4.1 The Robots Involved in this Work

For the practical demonstration of this thesis, we have considered 3 robots:

- *A Parallel Linear Axis,*

- The robot *Agietron Micro-Nano,*

- The 2-robot system *Agietron Micro-Nano* and *MinAngle.*

All the robots introduced here have been designed in the LSRO and built in collaboration with the companies AgieCharmilles SA and Mecartex SA (Losone, TI, Switzerland). Those robots will be presented in detail in the next sub-sections.

4.1.1 The Linear Axis

The first robot we have considered is an ultra-high-precision linear axis (Figure 4.1). A Linear Axis is a 1 DOF "building brick", used to create complex robotic systems. To respond to the ultra-high-precision building criteria seen in sub-section 1.2.4, it has the following features:

- Parallel kinematic: the robot arms are arranged to form a parallelogram (Figure 4.2).

- Flexure-hinges joints are used.

- Ultra-high-precision sensor: a Heidenhain® rule with resolution of 5 nm is used to measure its articular position.

- High-accuracy motor: a voice-coil motor is used to actuate the linear axis.
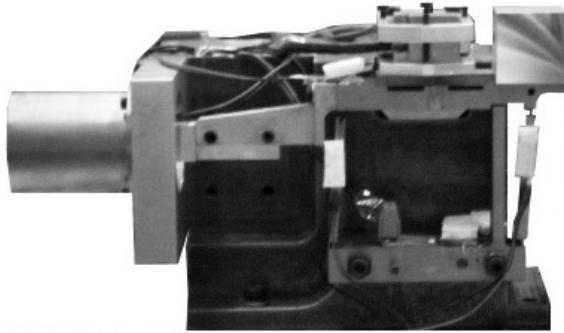
Figure 4.1: *A picture of the parallelogram.*
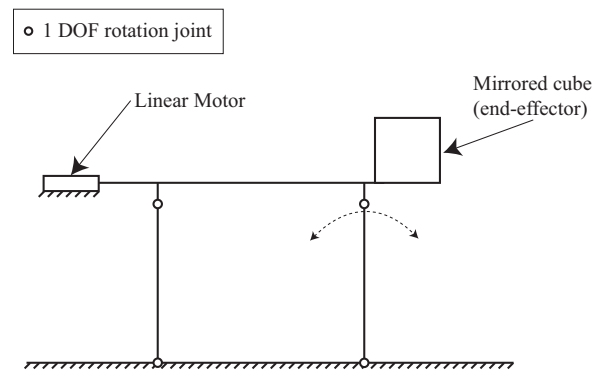
Figure 4.2: *The kinematic chain of the linear axis.*
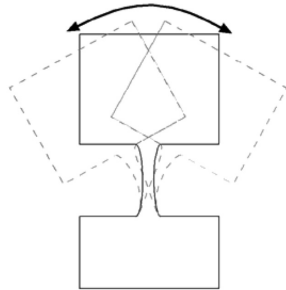
Figure 4.3: *A flexure hinge joint.*
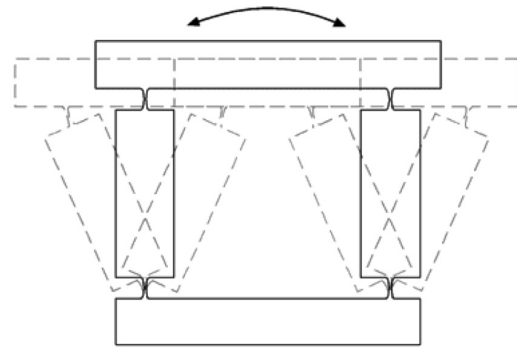
Figure 4.4: *The linear axis and its stroke.*

Flexure hinges [36] are thin-metal plates, flexed to obtain a rotational DOF (Figure 4.3). Typical flexure hinges thickness is between 100 μm and 500 μm. In this particular case the thickness is ~70 μm. In order to let the hinges work in their material elastic zone, their flexion is limited to some degrees. Due to this limitation, the linear axis inherits a course of 10 mm.

A flexure-hinges linear axis is designed to be machined from a monolithic block of material. It has been built using the wire-EDM[1] process from a single piece of titanium.

When actuated, the linear axis performs a horizontal translation along a parabolic trajectory (Figure 4.4). A parasitic translation along the vertical axis is generated as well. By arranging three parallelograms orthogonally and by connecting them together with three other parallelograms (like in the case of the *Delta Cube 2* robot - Figure 2.1 on page 18), it is possible to mutually compensate the parasitic translations of the three parallelograms.

Aim of the Linear Axis Calibration

We consider this case to study how environmental effects act on a simple robot structure. Furthermore, this is the first test to check if the calibration procedure proposed in Chapter 3 is reliable enough.

---

[1]wire-EDM: Wire Electric Discharge Machining.
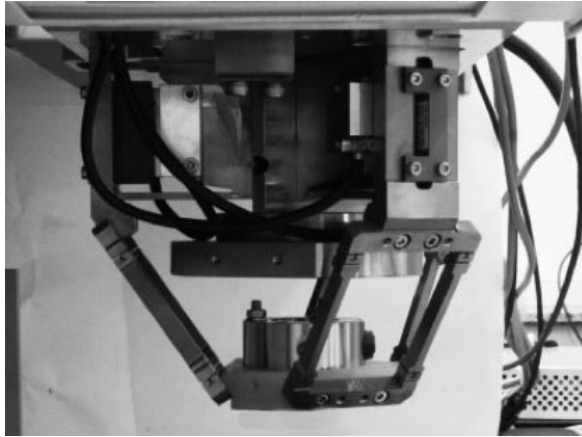
Figure 4.5: *A picture of the Agietron Micro-Nano robot (delta kinematic).*
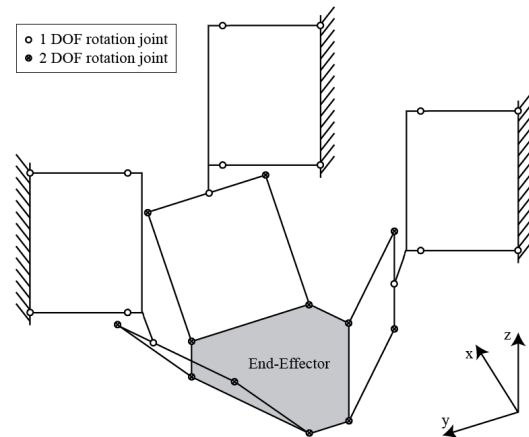
Figure 4.6: *Kinematic chain of the Agietron Micro-Nano.*

4.1.2 The Agietron Micro-Nano

The Agietron Micro-Nano (Figure 4.5) is an ultra-high-precision robot designed to perform μ-EDM process.

A modular concept has been used to design this robot: 3 structures similar to the linear axis seen before are arranged together vertically in order to actuate the robot. Thus, a secondary group of parallelograms is used to connect each linear axis to the robot end-effector (Figure 4.6). Each parallelogram has been built from a monolithic block of titanium, using the wire-EDM process. The kinematic of this robot is based on Clavel's Delta kinematic [10].

The robot inherits the resolution of the linear-axis sensors (5 nm) and the limited working volume due to flexure-hinges joints: ~1 cm³. Furthermore, it has a size of ~$20 \times 20 \times 25$ cm^3.

The robot has 3 DOF in translation and it performs parasitic rotations of maximum 50".

Thanks to all the characteristics described here, the robot is capable to position is end-effector with ultra-high level of precision.

The μ-EDM process

The μ-EDM process is used for cutting complex shapes and thin walled configurations without distortion. It is recommended for hard materials or for materials typically machined by grinding [14]. The process is suited for applications characterized by extremely exacting tolerances (accuracy ~1 μm). Since it is a contactless process, it is also well suited for making fragile parts that cannot take the stress of a normal machining process. To perform it, a wire-shaped electrode is mounted on the robot end-effector. A controlled electrical spark is used to erode away from the manufactured object any material that can conduct electricity. A series of discharges takes places between the electrode and the conductor while the robot is moving along the desired trajectory.

In a previous PhD thesis done at the LSRO [42], the μ-EDM process performed using an ultra-high-precision parallel robot has been characterized.
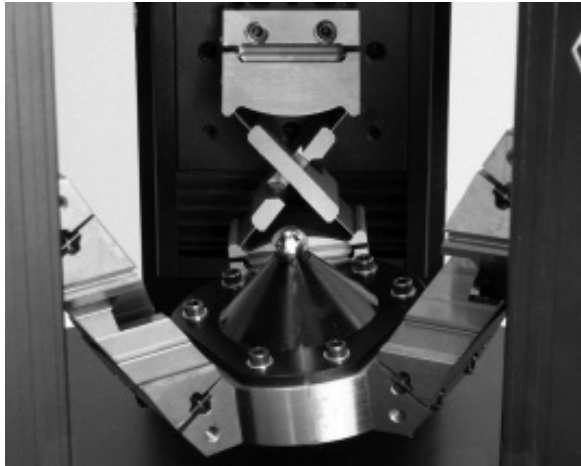
Figure 4.7: *A picture of the MinAngle Robot.*
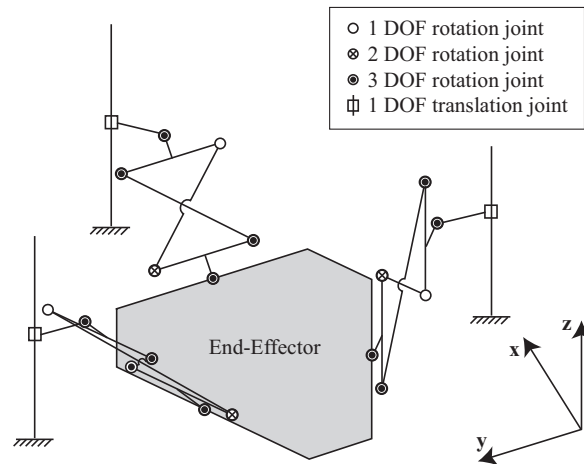
Figure 4.8: *Kinematic chain of the robot Min-Angle.*

Aim of the Agietron Micro-Nano Calibration

We consider this case to study how environmental effects act on a more complex robot. Moreover, we introduce the study of external forces acting on the robot. Finally, we will compensate both effects at the same time.

4.1.3   The System Agietron Micro-Nano and MinAngle

The robot MinAngle (Figure 4.7) has been developed to enhance the capabilities of the Agietron Micro-Nano. It has been designed to hold the piece on which the Agietron Micro-Nano will perform μ-EDM (left-hand right-hand system) [65].

Even if the MinAngle has flexure-hinges joints and parallel kinematic (Figure 4.8), it cannot be considered as an ultra-high-precision robot. This is due to its encoders that have a resolution of 0.25 μm, and to its actuators, DC motors with recirculating ball screws and ball bearing guides, which introduce friction in the system. In consequence, the MinAngle is categorized as a high-precision robot.

The MinAngle has 2 DOF in rotation (around the horizontal axes) and 1 DOF in translation (along the vertical axis). It has a rotation range of ±15° and a translation range of ±5 mm. Thanks to these features the robot is capable of compensating for the parasitic rotations of the Agietron Micro-Nano (only around the horizontal axes). On the other side, since the MinAngle performs parasitic translations along the horizontal axes, the Agietron Micro-Nano will have to compensate for them.

The two robots together form a robotic system that fills up a volume of ~$32 \times 32 \times 50$ cm^3 (Figure 4.9) and has a total of 5 DOF. Both robots have a vertical translation; this redundancy leads to an enlargement of the vertical stroke of the system.
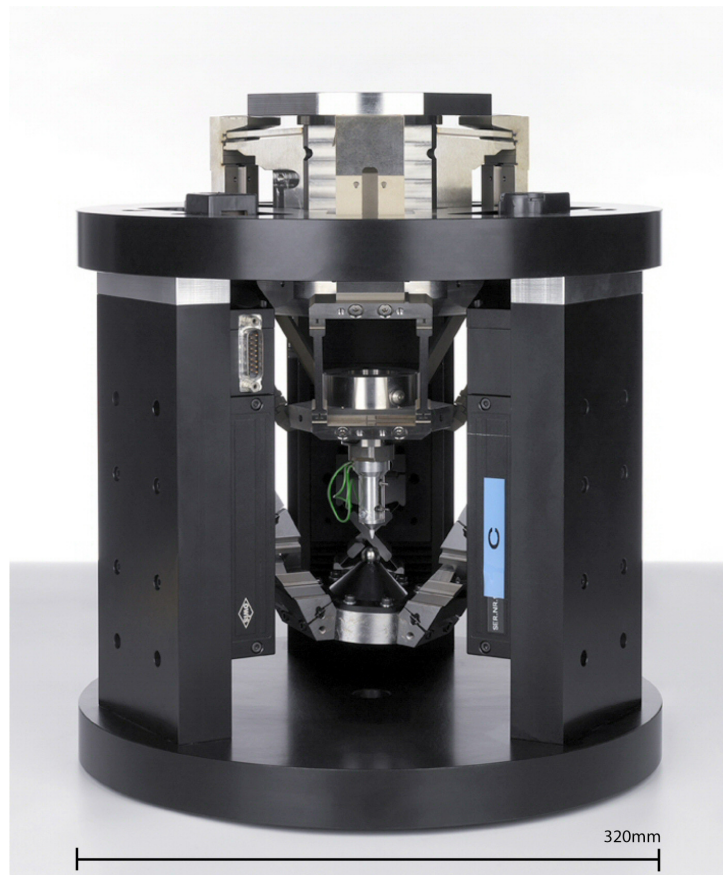
Figure 4.9: *A picture of the 2-robot system composed by the Agietron Micro-Nano (on top) and the MinAngle (down).*

Aim of the Agietron Micro-Nano and MinAngle Calibration

We consider this case to study how environmental effects act on a system composed by two robots. Furthermore, we will consider the issues linked to the incertitude in referencing a robot towards an other, and the incertitude linked to referencing the manufacturing process tool-tip.

Finally, we will use the system to perform the nano-indentation process with the aim of confirming the 2-robot system calibration.

4.2 Measurement Devices and Techniques

In this section we present the measuring devices that we have used in the practical part of this work. Since for each robot we have developed a different measuring setup, here we will introduce only the "bricks" that we employed to constitute each system and the measuring techniques common to the three cases.

We underline here that all the measurements and experiences illustrated in this thesis have been performed on a Newport® anti-vibration pneumatic table.
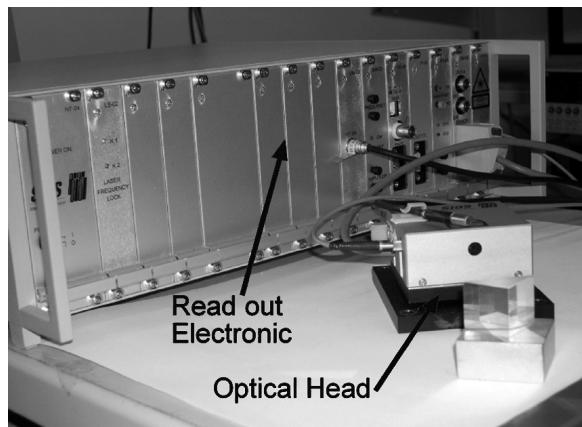
Figure 4.10: *The SIOS SP-2000 laser interferometer.*
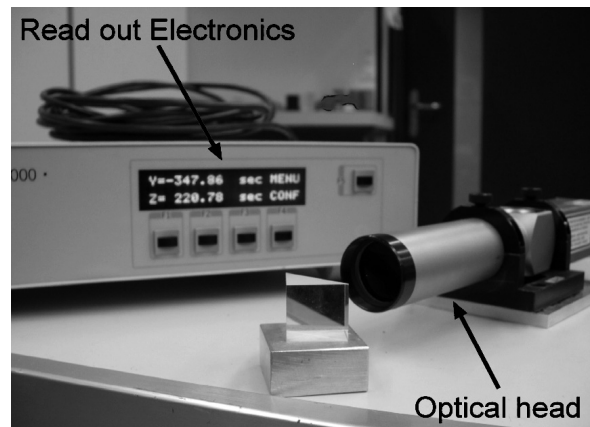
Figure 4.11: *The Newport LDS-1000 autocollimator.*

4.2.1   The Interferometer

In all the measurements done in this work, translations are measured using one or more SIOS® SP-2000 laser interferometers (Figure 4.10). The model that we used has a resolution of ~1.24 nm, wavelength of ~633 nm and a stroke of ~2 m. By nature the interferometer is a relative instrument, in the sense that it does not have a fixed origin. The working principle of the interferometer will be deepened in Appendix A.1 and A.3.

The measures performed with the interferometer are strongly influenced by changes of the air refraction index. Changes of the air temperature, pressure and humidity will generate a change in the air refraction index, which will cause a *drift* in the measure of the interferometer. Furthermore, those changes can be local: the refraction index of the air is different in any region crossed by the interferometer laser beam. For this reason, this instrument is extremely sensitive to air turbulence.

The following stratagems are employed to overcome the above-mentioned issues:

- The interferometer is equipped with a *pt100* thermal sensor. This sensor has to be placed near the laser beam, in order to monitor the temperature of the air crossed by the beam. The built-in electronics of the interferometer will use this reading to compensate the changes of the refraction index.

- The drift due to refraction index changes is proportional to the laser beam path length (also called the dead-path). Mounting the interferometer as near as possible to the surface that we want to measure will lower the influence of this effect. Moreover, it is possible to set the dead-path length to let the interferometer electronics compensate for this effect.

- We measured pressure and humidity with other devices, and we saw that such quantities vary very slowly in comparison with our measures, so we neglected them.

- We covered all the measuring system in order to limit the influence of air turbulence.

Active Thermal Stabilization of the Interferometer Base

As the interferometer is an instrument that is really sensitive to thermal drift, it is necessary to consider every detail when designing a setup in which it is used.

The problem of measuring at nanometer precision is that thermal expansion also affects the measuring device: environmental effects will deform the interferometer and move it, altering the measures. If the drift of the interferometer is not controlled or compensated, the acquired measurements will not represent the behavior of the robot alone, but the behavior of the system "robot + measuring device" subject to environmental effects. Even if it is possible to find a mathematical model that fits this data, it will not represent the robot behavior.

For this reason we actively stabilize the base of the interferometer, using the technique explained in sub-subsection 3.2.1.2 on page 39.

4.2.2 The Autocollimator

Rotations are measured using 2 Newport LDS-1000 autocollimators. Those devices have a resolution of 0.02" and a measuring stroke of ±400" (Figure 4.11). With them it is possible to measure 4 DOF (the vertical rotation axis is measured by both devices, and thus allow for measuring confirmation tests). Both devices have been calibrated by METAS[2].

In the case of the Agietron Micro-Nano measuring system, the principal aim of the rotation measurement is to keep into account the end-effector parasitic rotations of the Agietron Micro-Nano. These rotations affect the interferometer reading, adding the cosine error to measurements [27]. Errors due to parasitic rotations are corrected in real-time by using the technique explained in Appendix A.3.

For the MinAngle calibration, the autocollimators are used to measure a part of the rotation stroke of the MinAngle end-effector.

The working principle of the Autocollimator is detailed in Appendix A.2.

The autocollimators are mounted on a 2-DOF micrometric rotational stage, which allows an easy alignment of the device.

4.2.3 The Mirror Cube

A Zerodur® mirror cube has been mounted on the end-effector of each robot. It has an edge of 30 mm and a weight of ~68 g. This item has two purposes: firstly, the mirrored surfaces are used to reflect the laser beam of the optic measuring devices; then, the cube defines the frame of the robot end-effector and the 3 lines perpendicular to the mirror surfaces define the directions of the frame.

The mirror cube has only three mirror surfaces, orthogonal between them. The angles between those facets have been measured as well as the mirror surface accuracy, evaluated to better then ~30 nm ($\lambda/20$), especially in zones far from the cube borders. Those 3 surfaces are used to reflect the interferometer's laser beam.

---

[2]METAS: Swiss Federal Office of Metrology.
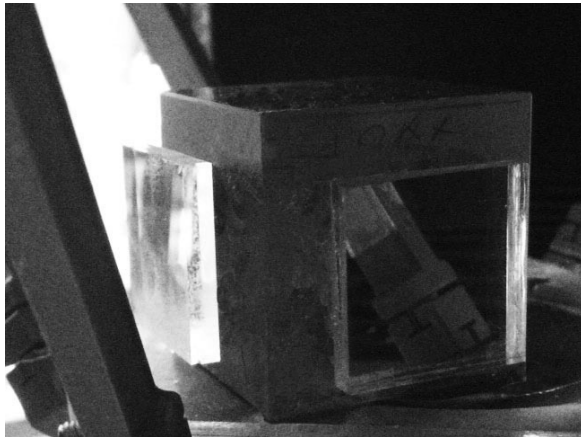
Figure 4.12: *A picture of the cube with the added mirrors, as mounted on the robot Agietron Micro-Nano.*
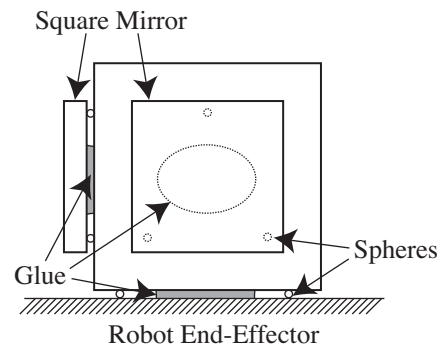
Figure 4.13: *Scheme of the gluing of the cube.*

One not-mirrored cube facet is used to glue the cube on the robot end-effector. The remaining two not-mirrored facets have been equipped with two squares mirrors[3] ($20 \times 20 \times 3$ mm^3) in fused silica, used to reflect the autocollimators' beams. In this way, with one cube we are able to use five measuring devices at the same time (Figure 4.12). The gluing of the two mirrors and the gluing of the cube on the robot is done using three spheres placed between the two surfaces to be glued (Figure 4.13). In this way, such surfaces are isostatically linked together. Thus the parallelism between the two surfaces is insured within the manufacturing tolerances of the spheres and the surfaces accuracy.

For the purpose of maintaining the accuracy reached *after* the calibration process, the cube must not be dismounted from the robot end-effector. Dismounting the cube will bring to a change of the end-effector weight and center of mass. This will cause a different deformation of the robot structure, invalidating the calibrated model.

4.2.4   The Touch Probe

For the measuring setup of the MinAngle, a touch probe has been used to complete the measures acquired with the interferometer and the autocollimator. This device has a stroke of 10 mm along one axis and a resolution of 5 nm. The device is built by the company RSF Electronik (Figure 4.14). As this type of measure is based on contact, its final accuracy is estimated to ~1 μm.

Devices of this kind have been already used to perform measuring tasks for calibration in previous LSRO theses [30, 64].

---

[3]The surface accuracy of those mirrors is 4-6λ per inch. For the working principle of the autocollimator, based on the different collimation of a defined pattern, the fact that the surface accuracy is at this level does not affect the measuring accuracy.

Figure 4.14: *The RSF Electronik touch probe.*

Figure 4.15: *The Schaevitz Sensors inclinometer.*

4.2.5 The Inclinometer

Still for the measuring setup of the MinAngle, an inclinometer has been used to enlarge the measuring range of the autocollimators. The inclinometer has a stroke of ±20° and a resolution of 0.01° (corresponding to 36"). A mounting in aluminum with three spheres on the base has been developed, in order to isostatically place it on a surface. The inclinometer is built by the company Schaevitz Sensors (Figure 4.15).

4.2.6 Thermal Sensors

To study how thermal effects deform the robots, we have installed on the system several *pt1000* thermal sensors (platinum resistance thermometers). Meanwhile, we monitor the air temperature near the laser interferometers beam: each interferometer has its built-in *pt100*[4] sensor to measure and compensate for thermal air changes (Figure 4.16 on the next page). Details about the position of each sensor will be given for each measuring setup.

The readings of the pt1000 sensors are acquired using a high-precision multi-channel A/D converter (Keithley 2700), while the readings of the pt100 sensors are available in the interferometer reading.

The pt1000 sensors are glued directly on the part to measure, using thermal conductive glue, while the interferometer pt100 is placed nearby the interferometer's laser path, in order to monitor the air temperature in proximity of the laser beam.

---

[4]Difference between pt100 and pt1000: even if both are platinum resistance thermometers and thus work on the same principle, they have two differences. The first consists in the fact that at 0 °C, a pt1000 has an ideal resistance of 1000 Ω, while a pt100 has a resistance of 100 Ω. The second lies in the fact that the pt1000 resistance grows of 3.85 Ω/°C, while the pt100 resistance grows of only 0.385 Ω/°C. A pt1000 has therefore a larger slope and thereby makes possible a higher resolution in measuring. On the other side, with a pt100 it is easy to develop thermometers for a large temperature range.
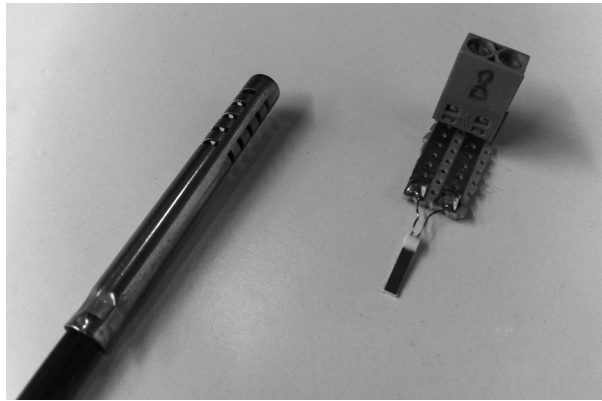
Figure 4.16: *On the left a pt100 thermal sensor ready to be used, on the right a pt1000 thermal sensor to be glued on the setup.*

4.3   Other Devices

Here we present two other devices that we have developed to carry out the force calibration and the nano-indentation process.

4.3.1   External Force Simulator

As we have seen in the state of the art, external forces acting on the robot can also cause a significant deformation in the robot geometry [68]. Their influence in terms of loss of accuracy depends on their order of magnitude and on the stiffness of the robot. For this reason it is necessary to evaluate their size and their effect on the robot structure.

In this work we consider the cutting-forces generated by the μ-EDM process on the Agietron Micro-Nano as an explicative case study. The considerations and the results that we obtain on this specific case can be extended to other kinds of external forces acting on robots (*e.g.* gravity), at condition that those are measurable and have repetitive effect on the robot geometry.

4.3.1.1   Force Calibration

In the case in which an external force is acting on the robot, we can use the calibration procedure proposed in Chapter 3 to compensate its effect. From a practical point of view we need the reading of the external force applied on the robot. This measure will be used to build a model capable of compensating for the force-induced deformation. Once the modeling is done, this measure is still used to calculate - thanks to the calibrated model - the positioning error due to the force, and compensate for it.

For example, to measure cutting forces we propose the following solutions:

1. Mounting a force sensor between the tool-tip and the end-effector,

2. Reading the force applied by the motors to keep the robot to a steady position, while the cutting-force is acting on the robot.
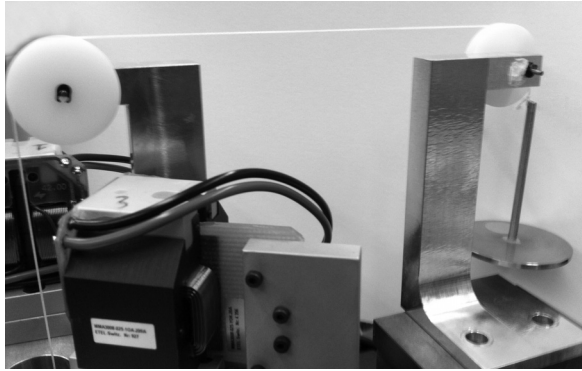
Figure 4.17: *A picture of the force simulator system.*
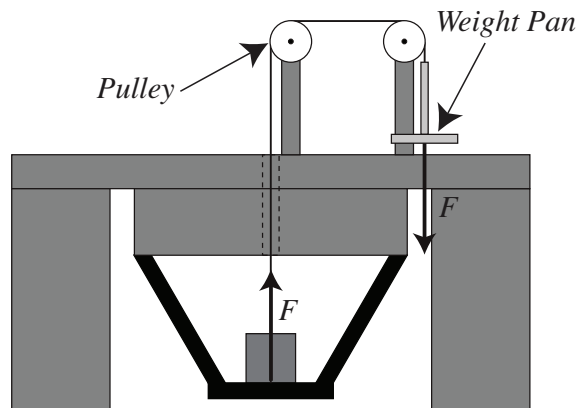
Figure 4.18: *Scheme of the force simulator.*

These methods are both effective, but they have the following drawbacks: force sensors are normally based on the deformation of certain components[5] . Since we are interested in evaluating the deformations caused by the force at nano-scale, we cannot use this solution: it will introduce some deformations in the system that we are not able to read. Reading the force at the level of the motors it is the most elegant solution. Nevertheless it is not applicable in our case, because the motors that we use have an important hysteresis regarding the force. In this case it would not be possible to build a model using a non-repetitive measuring system.

Since none of these solutions was appropriate, we decided to build a device to apply forces on the robot end-effector. In this way, since we are imposing a known force, we do not need to measure it. The role of this system is to apply a vertical force on the end-effector, opposed to the gravity, with a value of the order of magnitude of the forces generated during the μ-EDM process. In this way we have a "μ-EDM simulator" available on our measuring setup without having all the bulky material to perform μ-EDM.

4.3.1.2 The Force Simulator

We basically build a 2-pan balance (Figures 4.17 and 4.18). The first pan is the robot end-effector itself; the second pan is connected to the robot using a 0.5 mm thick UHMWPE wire[6] through a system of two pulleys. We use UHMWPE because it is a material with a high Young's modulus (116 GPa[7] [63]). In this way we practically eliminate the oscillation of the end-effector due to the elastic effect of the weight on the wire.

The cutting force generated during the μ-EDM has been measured in [42]: using an indirect measuring method, the author demonstrated that with a 149 μm diameter electrode, a vertical repulsive force of 0.5 N is generated.

---

[5]A common force sensor consists for example in two condensers plates, which are displaced when a force is applied on one of the two. This displacement changes the value of the capacity almost linearly, depending on the force. By reading the capacity it is possible to calculate the force applied on it.

[6]UHMWPE: Ultra-high-molecular-weight polyethylene.

[7]Axial tensile modulus.
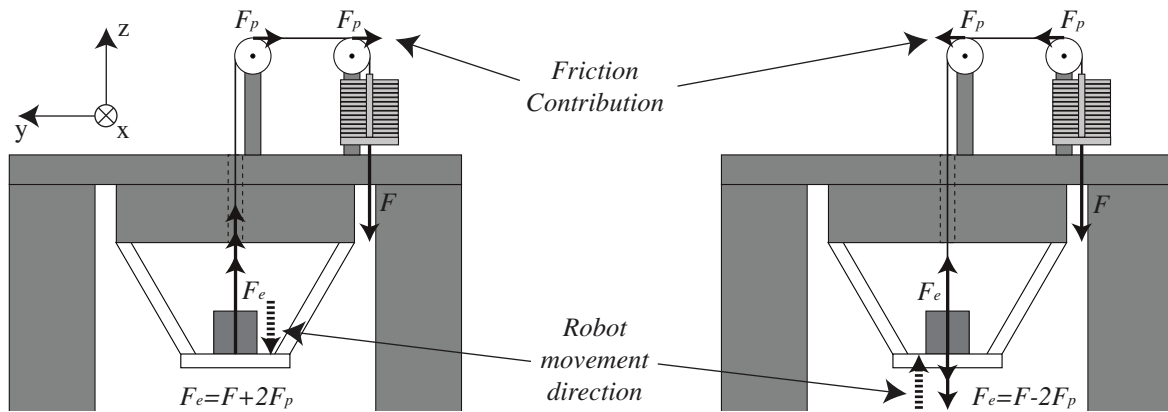
Figure 4.19: *The effect of the force generated by the weight versus the static friction while moving the robot along two different directions.*
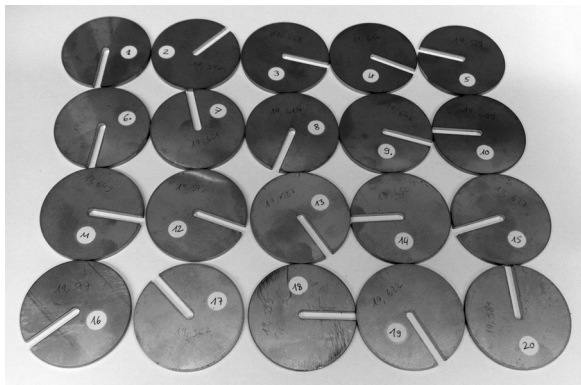
Figure 4.20: *A picture of the weights.*
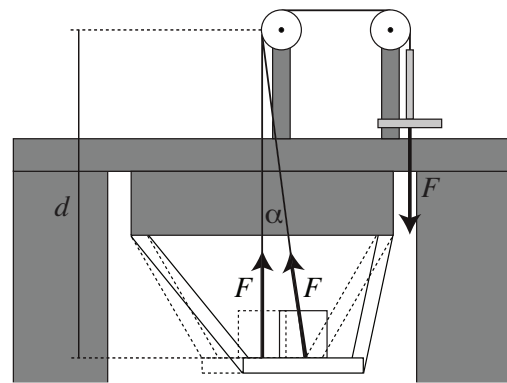
Figure 4.21: *Change of the force vector direction depending on the end-effector pose.*

To create a force of the same order of magnitude, we build a set of modular weights of ~20 g to be put on the balance's pan (Figure 4.20). We measured their weight with an high-precision balance (resolution of 1 mg) and we used this value to calculate the force that they will induce on the end-effector. In this way, we are capable of giving a force between 0 and ~4 N[8], with intervals of ~0.2 N, depending on the weight we are using. The weights are stainless-steel discs, with a diameter of 41 mm, a thickness of 2 mm and a 3 mm thick transverse slot to slide them on the pan.

We also performed an evaluation of the friction acting on the system. As we can see in Figure 4.19, the force F generated by the weight is not exactly transmitted to the end-effector. Depending on the direction of the end-effector movement, the friction of each pulley F_p has to be added or subtracted to F. F_p expresses the static friction between the pulley and the pivot.

To evaluate the effect of F_p, we charged the pan with the full load (392.25 g, correspond-

---

[8]The pan weight is 20.099 g. This means that a force of 0.197 N is always acting on the system. Since this force is constant, we consider it as the "zero" of the force system.

ing to 3.84 N), and we performed some repeatability tests, coming from different directions. We evaluated the effect of the friction to ±10 nm along the x axis, zero on y axis and ±5 nm on z axis. As this effect falls under the measuring standard deviation employed to measure this robot (20 nm) we decided to not consider it. For the difficulty related to measure of effects under the measuring standard deviation, those results have to be taken with caution.

Notice that the robot will change its end-effector pose while the system is in use. This means that depending on the robot pose - especially translations along the horizontal axes - the force direction will vary of a minimum amount. Referring to Figure 4.21, the distance between the end-effector and the pulley d is 38 cm. While moving the robot end-effector of 2 mm along the horizontal axis (at the limit of the workspace) we obtain an angle $\alpha = 24.555'$. By decomposing the force vector $F = 3.84209$ N along the horizontal and the vertical directions, we obtain a vertical contribution $F_v = 3.842$ N and an horizontal contribution $F_h = 0.027442$ N, corresponding to a weight of 2.8 g. Since the value of the horizontal contribution is low even in the case of the maximal weight, we assume that the force is completely vertical, consequently *the direction of the force F is not dependent on the position of the robot end-effector.*

By succeeding in the calibration of this force, we practically demonstrate that all the forces acting on the robot that are measurable and have a repetitive effect on it can be calibrated using the procedure proposed in Chapter 3.

4.3.2 Indentation System

Nano-indentation is a process that has been chosen to allow us solving the problem of referencing the two robots between their respective tool-tip and between each other.

By using it we will be able to evaluate the system final accuracy at the level of the robot tool-tip, performing de facto an alternative *Step 5* of the calibration procedure.

Indentation is a process normally used for determining the mechanical properties of materials [3] and has been already used in [27] to perform the calibration validation of the robot *Sigma6*.

In the next sub-subsections we will introduce the hardware that will be mounted on the robot to perform it, and the way we detect the contact between the two robots.

4.3.2.1 The Indentation Setup

We have equipped the Agietron Micro-Nano with a support holding a Vickers diamond (Figure 4.22) and the MinAngle with a simple cylindrical support, holding an Invar® substrate (Figure 4.23), Invar has been chosen for its very low thermal expansion coefficient.

The diamond support is simply screwed on the Agietron Micro-Nano end-effector. The diamond is mounted on a cylinder that can slide in a V rail. The cylindrical support of the substrate has its surface on the center of rotation of the MinAngle. In this way, when rotating the substrate, parasitic translations are limited.

After the calibration of the two robots, several marks will be indented in the substrate at well-known positions. The mark positions will finally be measured on a SEM microscope in order to evaluate the accuracy of the system at the level of the robot tool-tip.
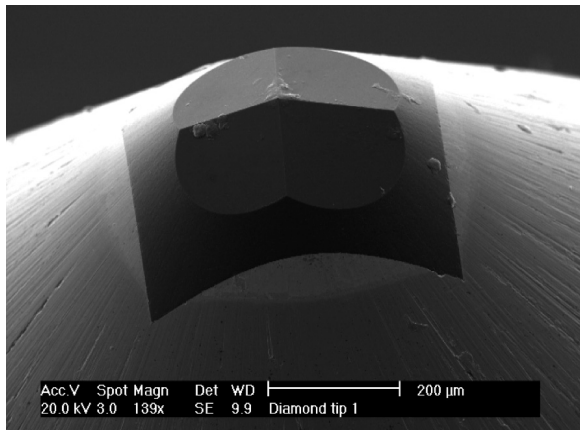
Figure 4.22: *A picture of the Vickers diamond taken with a SEM microscope.*
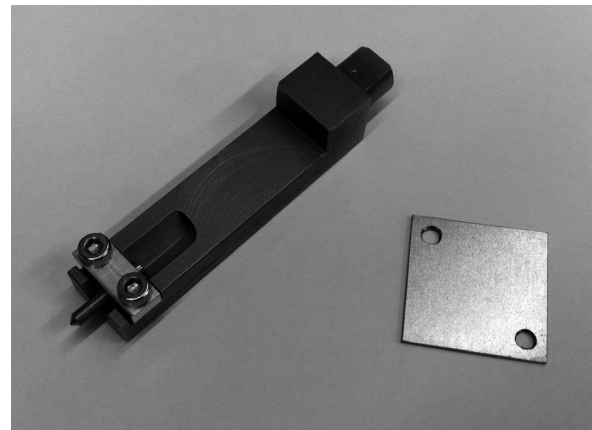
Figure 4.23: *The diamond support (left) and an Invar® indentation substrate (right).*
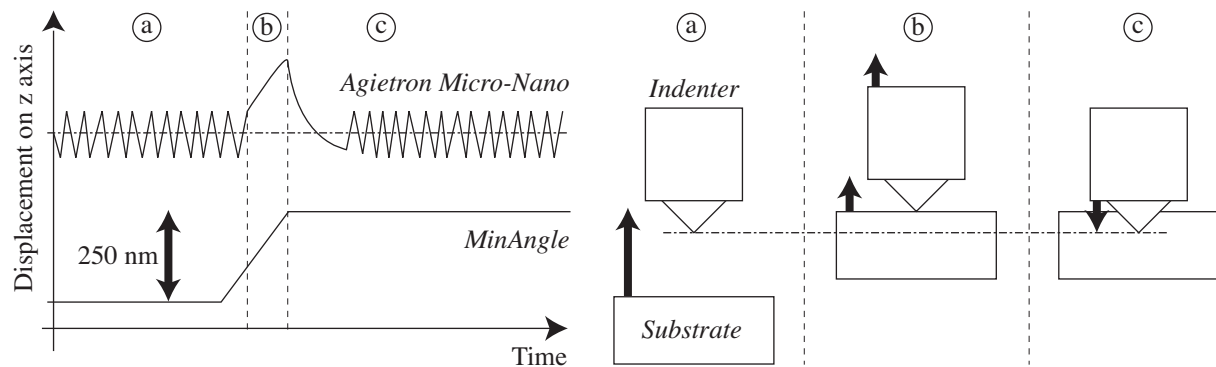
Figure 4.24: *Three phases of the contact detection using the Agietron Micro-Nano: in a) the MinAngle displaces towards the Agietron Micro-Nano indenter; in b) the contact between the diamond and the substrate happens and the Agietron Micro-Nano is pushed up; in c) the Agietron Micro-Nano reacts at the displacement by pushing back the robot and engraving an indent.*

The components used to do nano-indentation are mounted before the measurement for calibration: mounting them afterwards changes the center of gravity of the two end-effectors, invalidating the calibration.

4.3.2.2   Contact Detection

In [27], the author used a force sensor mounted under the substrate to monitor the force and to evaluate when the contact happens. In our case, we abandoned the idea of the force sensor (unstable, sensible to noise and subject to deformations) in favor of the *use of the robot as contact sensor*. In our procedure in fact, the Agietron Micro-Nano reaches the position in which the mark has to be indented. After that, the MinAngle start moving towards the Agietron Micro-Nano, by steps of 250 nm[9] until the contact is detected.

---

[9]Corresponding to the linear resolution of the robot. Dr. Fazenda used the same resolution to move the *Sigma6* robot during the nano-indentation process.

The contact is detected by observing the error plot of the Agietron Micro-Nano motors in real-time (Figure 4.24). Since this robot is steady, the error plot is between ±25-35 nm. When the MinAngle reaches the indenter and the contact happens, the MinAngle actually pushes the Agietron Micro-Nano, causing a step of 200-250 nm in the plot of the positioning error and forcing the robot controller to "react" to this displacement by giving more current to the motor. As a result of this event, an indent is produced.

After the contact detection, the MinAngle moves down away and the Agietron Micro-Nano moves to the next indentation position.

To perform indentation, we chose the horizontal plane of the Agietron Micro-Nano corresponding to z = 1 mm since is one of the widest.

4.4 Conclusion

In this chapter we have introduced the three case studies treated in this work, the measuring devices and techniques used to acquire the data. Furthermore, we have introduced two devices developed specifically for this work: a force simulator and a system to perform nano-indentation.

In the following part of this thesis we will demonstrate the reliability of the calibration algorithm introduced in Chapter 3. This will be done by presenting the calibration of the case studies, in order of complexity. We will show how the steps of the procedure are applied to each robot, starting from the *Step 1* of the procedure. Calibration results will be presented at the end of each corresponding chapter. Table 4.1 describes the sources of inaccuracy considered for each case.

Robot	*Sources of inaccuracy*
Linear Axis	Thermal
Agietron Micro-Nano	Thermal and External Forces
Agietron Micro-Nano and MinAngle	Thermal and Reference Incertitude

Table 4.1: *The case studies considered in this thesis in order of complexity.*

Part II

Case Studies and Results

Chapter 5

Case A: Linear Axis Calibration

We started testing the calibration procedure on the easiest case, a flexure-hinge linear axis. The aim of this study is to see how environmental effects act on a simple robot structure and to test the capabilities of the calibration procedure for the first time.

5.1   Step 1 - The Sources of Inaccuracy

In *Step 1* of the calibration procedure we have to consider the sources of inaccuracy acting on the system. The case of the linear axis is particularly interesting because we can study the effect of the thermal variations on an easy geometry. To do so, we glued a thermal sensor on each part of the parallelogram and on each part of the measuring system.

In this particular case, the influence due to the motor heat is limited, since the motor is outside the measuring loop and since it is mounted horizontally.

5.2   Step 2 - Measurements

5.2.1   Measurement System

The measurement system adopted for this case is illustrated in Figure 5.2. The parallelogram is equipped with a Heidenhain® linear optical sensor with a resolution of 5 nm. This optical rule will be used to measure the motor coordinate of the linear axis.

We equipped the linear axis with a mirror cube, in order to define the measuring frame and to reflect the beams of the measuring devices.

The interferometer reading is affected by parasitic rotations around the axes perpendicular to the laser beam. We measured them with an autocollimator: on the overall course of the parallelogram we obtained ±0.5" around y, and ±3" around z. The influence of such rotations on the measure of the interferometer is evaluated to less then 1 nm. As this value is lower than the sensor resolution we decided to ignore this effect, limiting our measuring system to one interferometer (Figure 5.1).

The aluminum support of the interferometer was actively stabilized (as explained in 3.2.1.2 on page 39) to avoid thermal drift. Ten *pt1000* temperature sensors were mounted on the entire measur-
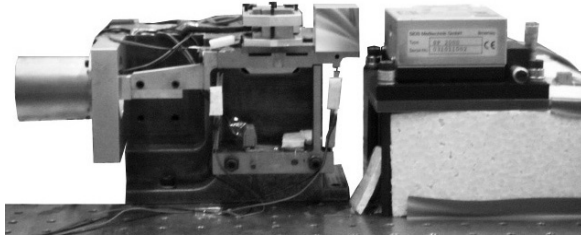
Figure 5.1: *A picture of the linear axis and its measuring system.*
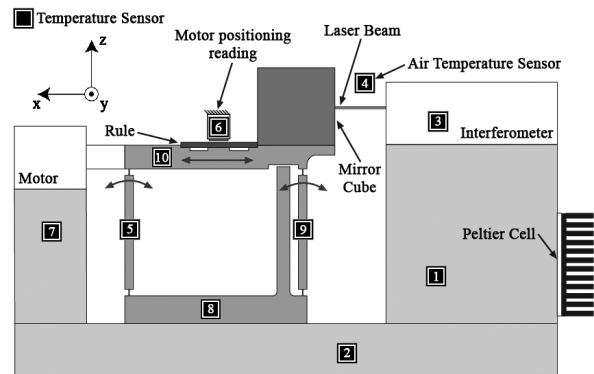
Figure 5.2: *The position of the sensors used to read the thermal drift.*

ing loop (refer to Figure 5.2 for the positions of the sensors). The thermal measurements are acquired through the use of a multi-channel A/D converter (Keithley 2700) connected to a computer.

As the interferometer is a relative instrument we need to define a zero for it. We define as zero the measure that we have on the interferometer when the optical rule measures zero as well. As we expect this zero to drift while the temperatures are changing, we coupled this measure to the reading of all the thermal sensors at that particular moment, defining in this way a "thermal initial condition".

5.2.2   Measurement Procedure

Step 2 of the calibration procedure consists of measuring different end-effector poses in the robot's entire workspace while the sources of inaccuracy are acting on the robot. Since we are not using an inverse geometric model to move the system, we will displace the linear axis using an identity model (end-effector coordinates = motor coordinates).

The measurements have been taken during 1 day, while the room temperature was changing from 20.5 °C to 21.5 °C. We used the air conditioning (AC) to simulate the free oscillation of an industrial environment in the following way: before starting the measuring session, the AC consign has been putted to the minimum temperature level possible (~20 °C). We started the measurements when the room reached the lowest temperature. After that, a higher consign has been imposed to the AC device (~22 °C). Therefore, the measurements have been collected while the air temperature was varying. To minimize the thermal drift due to operators entering in the robot's room, the measures have been acquired during the weekend and all the equipment were controlled remotely.

The robot workspace is a line of 10 mm length. Measurements have been taken for the following motor coordinates: 0.0 -4.0 -3.5 -3.0 -2.5 -2.0 -1.5 -1.0 -0.5 0.0 0.5 1.0 1.5 2.0 2.5 3.0 3.5 4.0 mm (18 points – the origin is placed in the center of the rule).

For each of those points the interferometer acquired 4 separate measurements. Each single measurement in actually an average of 2048 measurements, but the interferometer controller only communicates the average to the computer. As seen in sub-subsection 3.1.2.3,
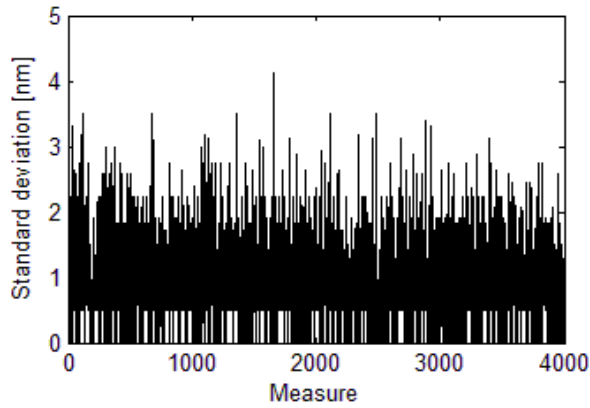
Figure 5.3: *Plot of the measurement standard deviation, used to test the quality of the measures.*
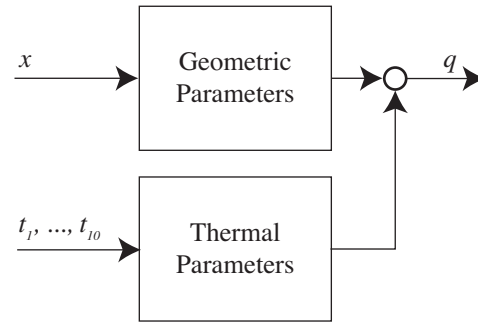
Figure 5.4: *The model scheme to control the linear axis position.*

the purpose of measuring the same point 4 times is the quality control of the measurements. We can detect if something went wrong in the measurement by calculating the standard deviation of those 4 measurements. If the value of it is superior to 5 nm all four points will be rejected (see Figure 5.3 for the plot of the standard deviations). Otherwise they will be averaged and kept for the next phases of the experiment.

During 24 hours, a total of 15844 measures have been taken (3961 groups of 4 measures). Since all groups of 4 had a standard deviation below 5 nm all the points were considered. For the next phase, only the data collected in the first four hours of the experiment was considered, because the temperature variation occurred in this period. The graph in Figure 5.5 shows the evolution of the air temperature during the first 4 hours of measurements. The first 4032 measurements have been considered, and after merging each group of 4 measurements together, only 1008 points remains. This data set has then been divided in two different sets, the first composed of 560 points (that we will call the "calibration" set), the second of 448 (the "validation" set). The calibration set is composed of all the measures done in integer position (*i.e.* 0.0 -4.0 -3.0 -2.0 -1.0 0.0 1.0 2.0 3.0 4.0) while the validation set is composed by all the remaining measures. The calibration set will be used to find the model parameters, while the second one will be used for validation and to calculate the error after calibration.

5.3 Step 3 - Modeling

We used the stepwise regression algorithm (Matlab®, Statistics Toolbox™) to perform *Step 3* of the calibration procedure. The parametric model that has been used during the experiment is the following:

$$q = \alpha x^2 + \beta x + \gamma + a_1 t_1 + \ldots + a_{10} t_{10} \tag{5.1}$$

In this equation, x is the position measured with the interferometer (so the end-effector coordinate); q is the position measured on the robot rule and $t_1, \ldots, t_{10}$ are the reading of the 10 temperature sensors. This model can be divided into two parts: the coefficients α, β and γ are dependent on the robot geometry, while the coefficients $a_1, \ldots, a_{10}$ are dependent on the

thermal readings. In short, the model is composed of 13 parameters, 3 purely geometrical and 10 dependent on thermal behavior (Figure 5.4).

In order to find the parameter values with Stepwise Regression, we have assembled the measuring data in this way:

$$Q = \alpha X^2 + \beta X + \gamma + a_1 T_1 + \ldots + a_{10} T_{10} \tag{5.2}$$

Where Q is a vector of motor coordinates corresponding to the measured positions vector X, and the measured temperatures vectors $T_1, \ldots, T_{10}$. X^2 is a vector containing the square of each element of X. By making explicit each measure in 5.2 we obtain:

$$\begin{bmatrix} q_1 \\ \vdots \\ q_m \end{bmatrix} = \alpha \begin{bmatrix} x_1^2 \\ \vdots \\ x_m^2 \end{bmatrix} + \beta \begin{bmatrix} x_1 \\ \vdots \\ x_m \end{bmatrix} + \gamma + a_1 \begin{bmatrix} t_{1,1} \\ \vdots \\ t_{1,m} \end{bmatrix} + \ldots + a_{10} \begin{bmatrix} t_{10,1} \\ \vdots \\ t_{10,m} \end{bmatrix} \tag{5.3}$$

Stepwise Regression will process the data in this way:

$$(\alpha, \beta, \gamma, a_1, \ldots, a_{10}) = stepwise \left(\left[\begin{bmatrix} x_1^2 \\ \vdots \\ x_m^2 \end{bmatrix} \begin{bmatrix} x_1 \\ \vdots \\ x_m \end{bmatrix} \begin{bmatrix} t_{1,1} \\ \vdots \\ t_{1,m} \end{bmatrix} \ldots \begin{bmatrix} t_{10,1} \\ \vdots \\ t_{10,m} \end{bmatrix} \right], \begin{bmatrix} q_1 \\ \vdots \\ q_m \end{bmatrix} \right) \tag{5.4}$$

In Appendix C we show how the Stepwise Regression algorithm selected the first three parameters to fit this model.

As we said, the advantage of this algorithm lies in its ability of deleting useless variables. A variable is considered useless if it not correlated to the data to fit, or if a variable already inserted in the model has the same correlation with the data.

In the tentative of increasing the results obtained with the model 5.1, more complex models with more parameters have been tested. Specifically, we tested a model that implies the interaction between geometric and thermal coefficients (considering the interaction between geometry and temperatures will generate 20 new coefficients), a model including first and second derivative of the temperatures and a model with up to 4th order geometrical coefficients. In the first two cases, the algorithm has deleted the new coefficients, proposing as solution the same model 5.1. In the third case, the algorithm stuck in a local minimum, proposing a solution that was not fitted enough to the data. We can extrapolate the following conclusions from this event:

- The exclusion of all the thermal and geometric cross parameters suggests that the thermal deformation is not dependent of the end-effector position. The fact that we can clearly detach the geometric part of the model from the thermal part (Figure 5.4) suggests that the thermal part of the model acts as a "moving offset" on the geometric model. This means that the geometric model alone can guarantee a good accuracy of the linear axis if the temperatures do not vary. In a way, this is confirmed by Fazenda's calibration procedure [27].
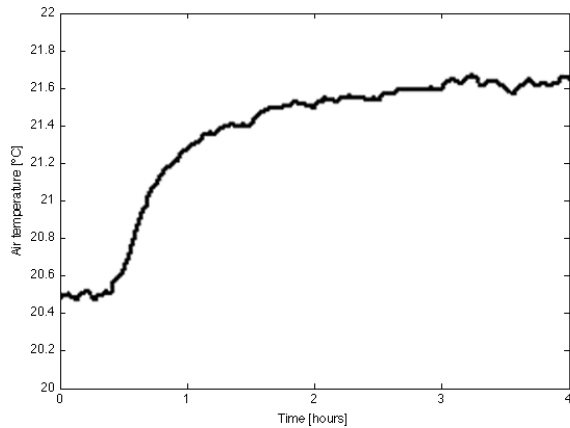
Figure 5.5: *Plot of the air temperature during the measurements (sensor 4 in Figure 5.2).*
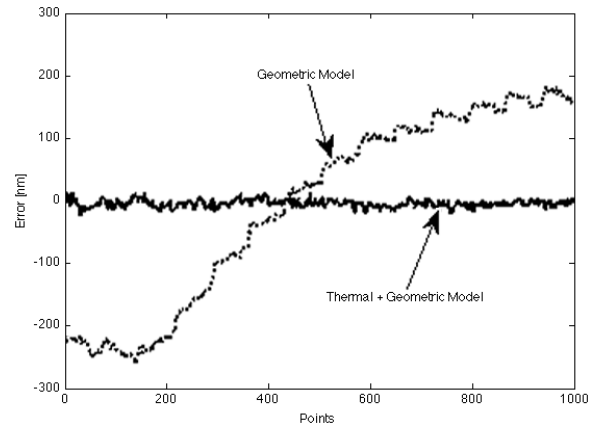
Figure 5.6: *Positioning error using a model with geometric parameters and a model with thermal and geometric parameters, while the thermal drift of Figure 5.5 took place.*

- First and second derivative of the temperatures do not contain any information on the deformation caused by the thermal effects. This is due to the fact that temperatures changes are really slow. Consequentially their derivatives are almost flat (so without information).

5.4 Step 4 and 5 - Results

The Stepwise Regression algorithm has been launched using the calibration data set and the model described by the equation 5.1. The data processing took 21 seconds (the Stepwise Regression found a solution in only 0.08 seconds). The algorithm has excluded from the model two temperatures: the temperature of the interferometer base (stabilized, so almost constant) and the temperature of the down part of the parallelogram.

The parameters found have been used to validate the calibration (in order to fulfill *Step 5*). In both calibration and validation sets, a final absolute error of ±9 nm for 90% of the points was obtained.

From a mathematical point of view, the model found is linear in the parameters and non-linear in the variables. Furthermore, referring to Figure 5.4, the geometric part of the model alone is time-dependent. By modeling the behavior of the robot towards the time-evolution of the temperatures, we obtain that the complete model is time-independent.

To demonstrate the importance of the temperature prediction we tested a model that considers only the geometric parameters of the robot (model with 3 parameters). In this case we have an error of ±206 nm for the 90% of the points. Figure 5.6 shows a comparison of the two models in all the measures. It is interesting to compare how the geometric model error follows the plot of the air temperature of Figure 5.5. Furthermore, notice how the error does not change for small amounts of time. This demonstrates the "moving offset" characteristic of the thermal drift.

Using a smaller data set for the parameter search was also tested. The input set has been cut in order to have only the first 300 points, representing the first hour of measurement, the one in which the most thermal variation happens. The stepwise regression converged, but in this case the error in the validation set was ±40 nm for 90% of the points.

Supposing a practical use of the linear axis, the thermal readings linked to the measure have been excluded by the model: only six thermal readings have been used (sensors 5-10 of Figure 5.2). A new parameter research has been launched and a final absolute error of ±15 nm for 90% of the points was obtained. In comparison with the result obtained with all the sensors, we can see that ±6 nm of error is related to the drift of the measuring device.

From the point of view of the robot end user it is important to underline that the thermal sensors reading must be active also during the normal usage of the robot: such information has to be read to feed the thermal part of the model, in order to compensate the linear-axis thermal drift.

5.5 Conclusions

We summarise here the most important conclusions related to this case:

- We obtained a prediction error of ±9 nm on poses not used for the calibration, using 1008 measures, acquired in ~4.5 hours (considering half an hour for the stabilization of the interferometer base).

- The complete data processing took less than one minute, while the parameters research took less than one second.

- A model containing geometric parameters up to the 2nd order and 8 thermal readings is sufficient to reach the ±9 nm of accuracy.

- Geometric parameters of higher orders, mixed geometric and thermal parameters and derivative of the temperatures are not needed to reach such accuracy.

- The thermal error is not dependent on the robot position and has the effect of displacing the offset of the model.

- We detached the drift due to the measuring device and it has been evaluated to ±6 nm.

In the next case we will use the experience gathered in the calibration of the linear axis to perform the calibration of a 3 DOF ultra-high-precision robot.

Chapter 6

Case B: Agietron Micro-Nano Calibration

In this chapter we introduce the second case study: the calibration of the robot *Agietron Micro-Nano*. The purpose of this experience is to study the influence of different sources of inaccuracy on the robot, namely geometric errors, thermal effects and an external force acting on the robot. This lead to confirm that the algorithm presented in Chapter 3 is also able to handle complex cases (multiple degrees of freedom and multiple sources of inaccuracy).

6.1   Step 1 - The sources of Inaccuracy

Also in this case, geometric and thermal issues play the predominant role in deforming the robot structure. Furthermore, as the robot is employed to perform μ-EDM, we will handle deformations coming from external forces.

As this is the first "industrial case" we consider in this thesis, we underline here that at nano-scale ultra-high-precision robots are really sensitive to any change in the structure and any change of the end-effector center of mass position. For this reason, we discourage removing or displacing the mirror cube from its position on the end-effector. For the same reason we recommend also to perform all the calibration measures with the manufacturing tool already mounted on the robot end-effector. Mounting the end-effector tool *after* the calibration process will result in a change of the center of mass position and in the end-effector weight, invalidating the calibration process.

To apply external forces on the robot, we will use the force device described in 4.3.1 on page 60. This device has been developed to produce deformations caused by a vertical repulsive force (such as the one generated by μ-EDM); it has not been developed to be a close-to-reality representation of such an industrial process, but rather to study the deformation caused by forces of the same order of magnitude and to prove that the calibration algorithm *is able to compensate any measurable source of inaccuracy having a repeatable effect on the robot.*
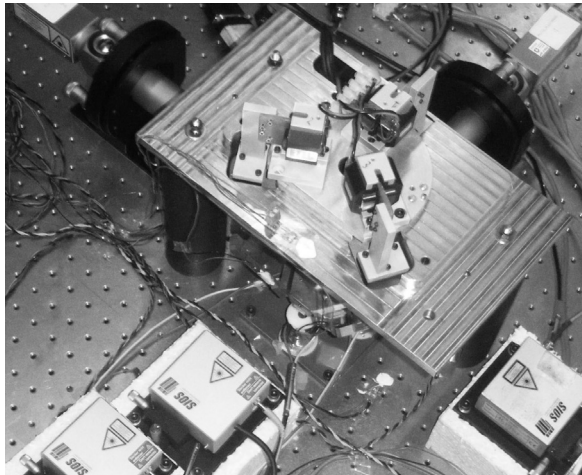
Figure 6.1: *Top-view picture of the robot and its 6 DOF measuring system.*
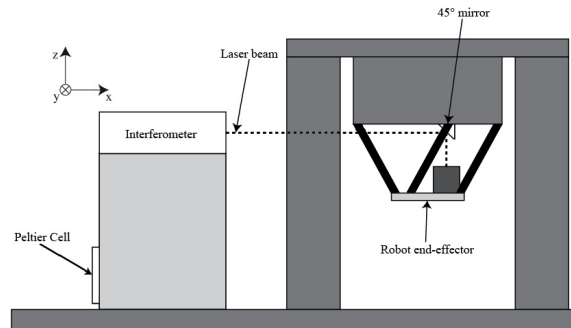
Figure 6.2: *Scheme of vertical axis measurement.*

6.2   Step 2 - Measurements

Here we introduce the measuring system we have used to perform the *Step 2* of the calibration procedure. The system is capable of measuring all the translations and all the rotations of the robot while measuring the temperatures of several parts of the system. Furthermore, the force simulator described in sub-section 4.3.1 on page 60, was used in order to apply forces on the end-effector.

Further details about the system configuration and the data-acquisition software are given in Appendix B on page 137.

6.2.1   Measurement System

A 6 DOF measuring system has been developed to measure the pose of the robot end-effector (Figure 6.1). To use it, the mirror cube has been glued on the robot end-effector. The cube has been mounted in the center of the end-effector while observing it from the x axis. This has been not possible in the perpendicular direction, because the parallelograms would have covered the cube (Figure 6.2).

Translations are measured using 3 interferometers; all of them are mounted horizontally. To measure the vertical axis, a 45° mirror has been glued on the robot top support (Figure 6.2). To avoid measuring the drift of the measuring system, we thermally stabilize the interferometers supports at 23.00±0.01 °C using the reading of the sensors 1, 2, and 3 of Figure6.3, we use the built-in compensation of the light wavelength in the air and we have inserted the approximate length of the dead-path in the interferometers' configuration (those settings are accurately explained in Appendix A.1).

Rotations are measured using 2 autocollimators. The reading of the autocollimators is used to correct the cosine error of the interferometers in real-time.

Temperature measurements are acquired using a total of 13 platinum resistance ther-
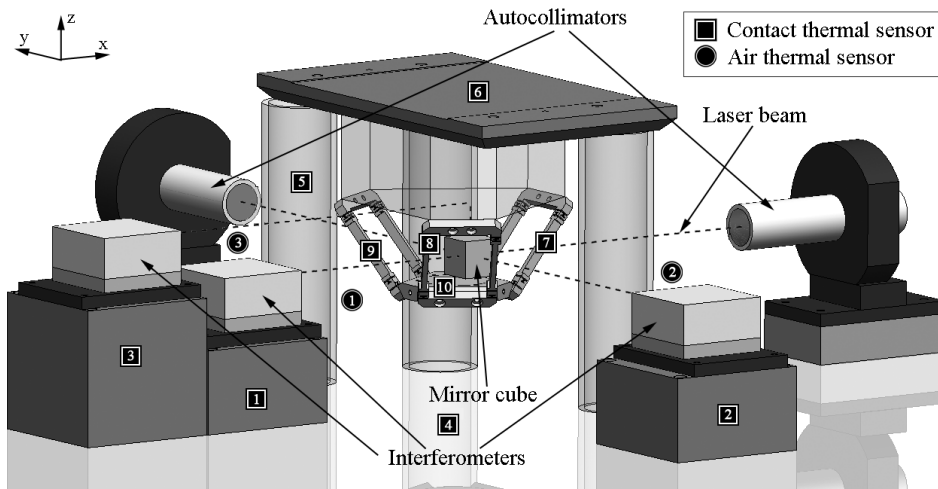
Figure 6.3: *Thermal sensors position.*
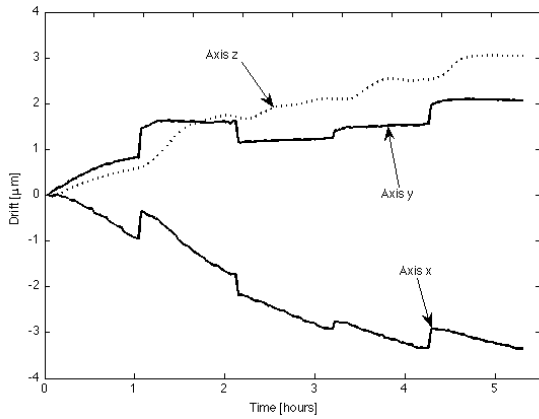
Figure 6.4: *The evolution of the zero during the measures.*
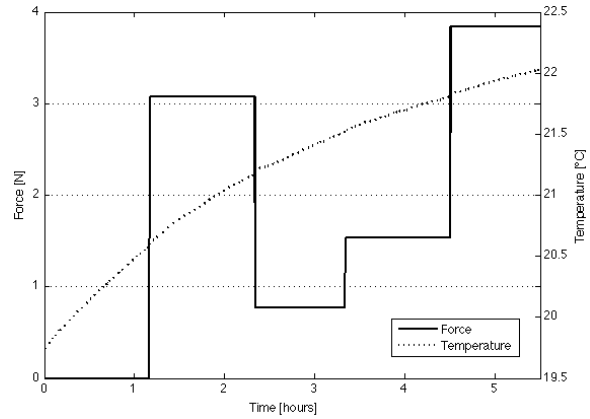
Figure 6.5: *The inaccuracies acting on the robot during the measures (the temperature refers to the reading of sensor 10, Figure 6.3).*

mometers: 3 sensors measure the air temperature near the interferometers beams and 10 sensors are glued on the system, along the measuring loop and on the robot (Figure 6.3); 3 of them are used for the stabilization of the interferometers bases; since their reading is practically constant their measure is not used for the calibration.

Finally, a pasteboard box covers the entire system. The box does not hermetically seal the system and it is not thermally insulated. The only purpose of the box is avoiding air turbulences, responsible of instability in the reading of the interferometers.

6.2.2   Measurement Procedure

To study the thermal behavior of the robot, we have measured the robot pose while the environmental temperature was changing. Also in this case, we used the air conditioning (AC) to

simulate the free oscillation of an industrial environment in the following way: before starting the measuring session, the AC set point was adjusted 19 °C. When this low temperature was reached we turned off the AC and started acquiring the measurements. In a period of 5.5 hours the robot temperature augmented by ~3°C (Figure 6.5).

We generate two regular grids of end-effector poses:

- The calibration grid, composed by 252 positions. A grid of $6 \times 6 \times 6$ motor coordinates (in 0, 0.5, 1.0, 1.5, 2.0, 2.5 mm) and a return to zero when every line is completed (36 return to zero in total).

- The validation grid, composed by 150 positions. A grid of $5 \times 5 \times 5$ motor coordinates (in 0.25, 0.75, 1.25, 1.75, 2.25 mm) and a return to zero when every line is completed (25 return to zero in total).

We used the force system to apply different forces on the robot end-effector in the following order (we considered $g = 9.81 \, m/s^2$):

1. The calibration grid, without any force (no weight on the pan);

2. The calibration grid, with a force of 2.305 N (12 weights: 235.280 g);

3. The validation grid, with a force of 0.768 N (4 weights: 78.391 g);

4. The calibration grid, with a force of 1.536 N (8 weights: 156.783 g);

5. The validation grid, with a force of 3.842 N (20 weights: 392.250 g);

In total we acquired 1056 positions. We used the data acquired in points 1, 2 and 4 to build the *calibration set* (composed by 756 points). The measures collected in points 3 and 5 will be respectively used to build a validation set *inside* and *outside* the calibration range (to see if the model have a good prediction capability even for forces/temperatures outside the calibration data range). The plot of the force is displayed in Figure 6.5. Notice that we do not augment the force progressively, because the calibration algorithm would find a wrong correlation between the effect of the growing force and the effect of the growing temperature.

The return to zero is used with the purpose of monitoring how the sources of inaccuracy act on a single point during the measurement. A plot of the zero drift is shown in Figure 6.4. Notice how the zero evolution follows the sources of inaccuracy illustrated in Figure 6.5.

With the purpose of checking the quality of the data, also in this case we acquired four interferometer measurements for each point and we calculate the standard deviation. This value is never superior to 20 nm.

6.3 Step 3 - Calibration

The next step (*Step 3*) consists in finding a model that accurately fits the relationship between end-effector coordinates *and* sources of inaccuracies towards corresponding motor coordinates. Once again, the Stepwise Regression algorithm will be used to find the coefficients to fit such relationship.

With the purpose of evaluating how every source of inaccuracy acts on the robot, we will build 4 different models that consider a part or the overall readings of the sources of inaccuracy. In the next subsections we will detail the variables kept in account for each of those models.

6.3.1 Pure Geometric Model
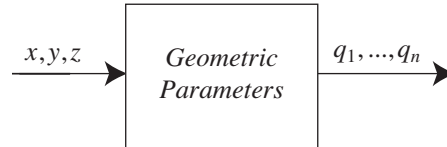
Figure 6.6: *The pure geometric model.*

We consider at first a pure geometric model (Figure 6.6). It has in input the measured end-effector poses (x, y, z) - the interferometers readings - and in output the corresponding motor coordinates:

$$q_1, q_2, q_3 = f(x, y, z) \tag{6.1}$$

To simplify the problem, we will divide the model 6.1 in three different equations:

$$\begin{cases} q_1 = f(x, y, z) \\ q_2 = f(x, y, z) \\ q_3 = f(x, y, z) \end{cases} \tag{6.2}$$

In this way we will perform the calibration axis by axis.

After that we need to generate new correlation variables. To do so we multiply element by element[1] the three vectors of interferometers measures (X,Y,Z, terms of 1st order) and we obtain new terms of 2nd and 3rd order:

- 1st order: X, Y, Z

- 2nd order: $X^2, Y^2, Z^2, XY, XZ, YZ$

- 3rd order: $X^3, Y^3, Z^3, XYZ, X^2Y, X^2Z, Y^2X, Y^2X, Y^2Z, Z^2X, Z^2Y$

To calibrate the axis q_1, Stepwise Regression will have to find the coefficients $a_1, \ldots, a_{21}$ to fit the following model:

---

[1]Element-by-element multiplication is a mathematical operation performable between two arrays having the same dimension. For example, if $A = \begin{bmatrix} a_1 & \ldots & a_n \end{bmatrix}$ and $B = \begin{bmatrix} b_1 & \ldots & b_n \end{bmatrix}$, the vector representing their element-by-element multiplication C will be $C = \begin{bmatrix} a_1 b_1 & \ldots & a_n b_n \end{bmatrix}$.

$$Q_1 = a_1 X + a_2 Y + a_3 Z + a_4 X^2 + a_5 Y^2 + a_6, Z^2 + a_7 XY + a_8 XZ + a_9 YZ +$$
$$+ a_{10} X^3 + a_{11} Y^3 + a_{12}, Z^3 + a_{13} XYZ + a_{14} X^2 Y + a_{15} X^2 Z + a_{16} Y^2 X + \quad (6.3)$$
$$+ a_{17} Y^2 X + a_{18} Y^2 Z + a_{19} Z^2 X + a_{20} Z^2 Y + a_{21}$$

The algorithm is called in Matlab in the following way:

$$(a_1, \ldots, a_{21}) = stepwise \left(\left[\begin{bmatrix} x_1 \\ \vdots \\ x_m \end{bmatrix} \begin{bmatrix} y_1 \\ \vdots \\ y_m \end{bmatrix} \begin{bmatrix} z_1 \\ \vdots \\ z_m \end{bmatrix} \cdots \begin{bmatrix} z_1^2 y_1 \\ \vdots \\ z_m^2 y_m \end{bmatrix} \right], \begin{bmatrix} q_1 \\ \vdots \\ q_m \end{bmatrix} \right)$$

Where m = 756 is the number of measurements composing the calibration set. To completely calibrate the robot, the parameters $a_1, \ldots, a_{21}$ have to be identified also for the remaining two motor axes.

As already mentioned in section 3.4 on page 44, notice that this way of finding a pure geometric representation of the robot geometry is original. In fact in the classic calibration procedure, it is the task of the robot developer to find a function describing the model 6.1; furthermore, as manufacturing and mounting tolerances corrupt this representation, an error identification phase is still needed. With this novel way of considering the calibration problem, modeling and identification are faced at the same time. The advantages are evident: the model found in this way has less parameters than a model found with the classic calibration algorithm, and thus the robot developer do not need anymore to build a mathematical function of the robot geometry, saving a great amount of time.

6.3.2   Geometric and Force Model
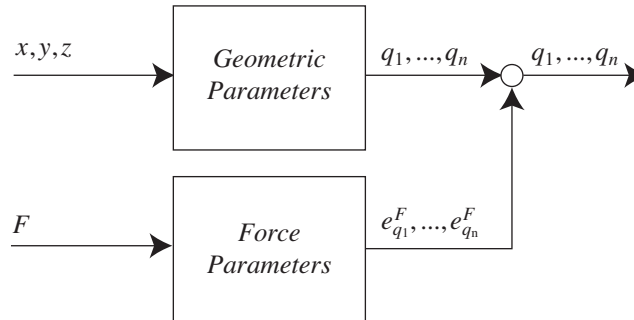
Figure 6.7: *The geometric and force model.*

The second model we consider will keep in account also the external force applied on the end-effector (Figure 6.7). To build it, we need to introduce the value of the force[2] (*F*) in

---

[2]As we do not measure directly the force applied on the end-effector, we use the value of the force generated by the weight to calibrate the robot. In a real case application, this value will be substituted by the measure of the external force applied on the robot.

the Pure Geometric Model seen in the last sub-section; this value will "represent" the force in the model. We use the vector of forces $\bar{F}$ to generate a 2$^{\text{nd}}$ and a 3$^{\text{rd}}$ order variables:

- Force variables: $\bar{F}, \bar{F}^2, \bar{F}^3$.

The model that Stepwise Regression has to fit becomes:

$$Q_1 = pureGeom + b_1\bar{F} + b_2\bar{F}^2 + b_3\bar{F}^3 \tag{6.4}$$

Where $pureGeom$ is the model 6.3 and b_1, b_2, b_3 are the new coefficients that Stepwise Regression has to find. In total, this model has 24 parameters. Also in this case, the parameter search must be done for the three motor axes of the robot. The complete model is described by the following equation:

$$q_1, q_2, q_3 = f(x, y, z, F) \tag{6.5}$$

Stepwise Regression is launched in the following way:

$$(a_1, \ldots, b_1, b_2, b_3) = stepwise\left(\left[\begin{bmatrix} x_1 \\ \vdots \\ x_m \end{bmatrix} \cdots \begin{bmatrix} F_1 \\ \vdots \\ F_m \end{bmatrix} \cdots \begin{bmatrix} F_1^3 \\ \vdots \\ F_m^3 \end{bmatrix}\right], \begin{bmatrix} q_1 \\ \vdots \\ q_m \end{bmatrix}\right)$$

Also here $m = 756$.

6.3.3 Geometric and Thermal Model
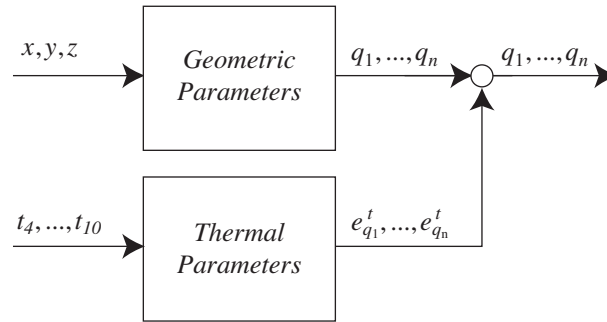
Figure 6.8: *The geometric and thermal model.*

We introduce here the third model considered for this case study (Figure 6.8). Here, we added the 7 vectors of thermal sensor readings to the Pure Geometric Model 6.3, as we did for Case A (compare with the model in subsection 5.3 on page 71, for the sensors numbering refer to Figure 6.3):

$$q_1 = pureGeom + c_4 t_4 + \ldots + c_{10} t_{10} \tag{6.6}$$

This model has a total of 28 parameters. A matter of discussion is still the number and the position of the thermal sensors added to the model. We choose to use the maximum

number of sensors capable of bringing *information* to the model without the presence of the measuring devices. In a real industrial application for example, the sensors measuring the air temperature would not be available, since they are linked to the interferometers. So we decided to not include their reading in the model. For the same reason, we excluded also the reading of the interferometers bases (moreover, once the stabilization is done the reading of t_1, t_2, t_3 is a noise largely included within $\pm$ 0.01°C). In addition to this, the temperature of the table (t_4) could be irrelevant, depending on the manufacturing process performed by the robot and on the position where the manufactured piece is fixed. Retaining only the seven sensors $t_4, \ldots, t_{10}$ we obtained a model described by the following equation:

$$q_1, q_2, q_3 = f(x, y, z, t_4, \ldots, t_{10}) \tag{6.7}$$

For one motor axis, the equation that Stepwise Regression has to fit is the following:

$$Q_1 = pureGeom + c_4 T_4 + \ldots + c_{10} T_{10} \tag{6.8}$$

To do so, Stepwise Regression is launched in this way (also in this case $m = 756$):

$$(a_1, \ldots, c_4, \ldots, c_{10}) = stepwise \left(\left[\left[\begin{array}{c} x_1 \\ \vdots \\ x_m \end{array} \right] \ldots \left[\begin{array}{c} T_{4,1} \\ \vdots \\ T_{4,m} \end{array} \right] \ldots \left[\begin{array}{c} T_{10,1} \\ \vdots \\ T_{10,m} \end{array} \right] \right], \left[\begin{array}{c} q_1 \\ \vdots \\ q_m \end{array} \right] \right)$$

6.3.4   Geometric, Force and Thermal Model

Figure 6.9: *The geometric, force, and thermal model.*

This model will describe the complete behavior of the robot (Figure 6.9). It will have as input the desired end-effector position (x, y, z), the value of the for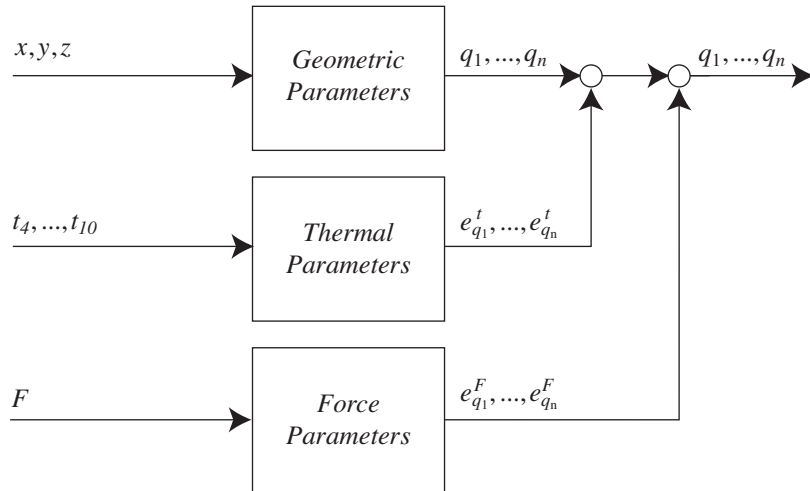ce applied on the end-effector (F) and the temperatures ($t_4, \ldots, t_{10}$). As output, it will return the motor coordinates (q_1, q_2, q_3) corresponding to the desired position (Equation 6.9):

$$q_1, q_2, q_3 = f(x, y, z, F, t_4, \ldots, t_{10}) \tag{6.9}$$

The model built in such way will take into account the geometric features of the robot, the deformations caused by the external force and the thermal effects.

All the variables seen in the previous cases are kept in account:

- Geometric variables: $a_1 X + a_2 Y + a_3 Z + \ldots + a_{21}$ (also called *pureGeom*),

- Force variables: $b_1 \bar{F} + b_2 \bar{F}^2 + b_3 \bar{F}^3$,

- Thermal variables: $c_4 T_4 + \ldots + c_{10} T_{10}$.

In total, this model has 31 coefficients to be found for each axis. Stepwise Regression will be launched in this way to fulfill the parameter research for the motor axis q_1:

$$(a_1, \ldots, b_1, \ldots, c_{10}) = stepwise \left(\left[\begin{bmatrix} x_1 \\ \vdots \\ x_m \end{bmatrix} \cdots \begin{bmatrix} F_1 \\ \vdots \\ F_m \end{bmatrix} \cdots \begin{bmatrix} T_{10,1} \\ \vdots \\ T_{10,m} \end{bmatrix} \right], \begin{bmatrix} q_1 \\ \vdots \\ q_m \end{bmatrix} \right)$$

The value $m = 756$ represents also in this case the number of measures in the calibration set. The calibration scheme proposed here is illustrated in Figure 6.9.

6.4   Step 4 - Implementing the Calibrated Model

In this step, we implemented the calibrated model described in subsection 6.3.4 in order to perform an online calibration confirmation. Notice that to work properly the model needs the reading of the thermal sensors and the value of the force applied on the end-effector. As those information are not available in the controller computer (all the measuring devices are connected to the measuring computer, refer to Figure B.1 for further details), we implemented the model in the measuring computer. The motor coordinates will be calculated here then sent to the controller computer via a TCP/IP connection.

For a commercial solution, the readings of the thermal sensors and the force have to be available on the robot controller computer. Regarding the thermal sensors, using an analog signal card reader could do this. Regarding the reading of the force, we propose two solutions already mentioned in subsection 4.3.1.1 on page 60:

1. Using a force sensor mounted between the end-effector and the tool-tip (Figure 6.10, a),

2. Using the reading of the force applied by the robot's motors as a force reading (Figure 6.10, b).
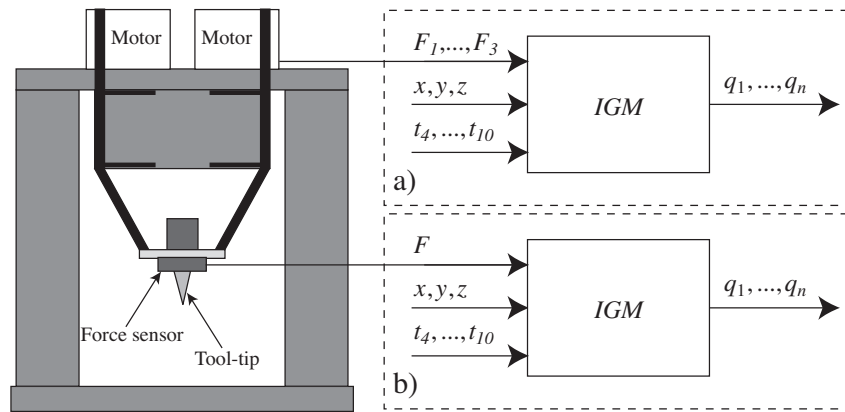
Figure 6.10: *Two ways to obtain a force reading suitable for a commercial solution.*

The first solution is the easiest to implement. On the other side, there is the drawback that the force sensor measuring principle is based on its deformation. For this reason, it will introduce an error in the system proportional to the force.

The second solution is the most elegant and reliable. Nevertheless, to make use of the force reading in a model, it is necessary that the force applied by the motors is repeatable. In our case, the robot has linear motors with moving magnets. Those are known for their hysteresis. It would be possible to use this technique by using voice-coil motors.

6.5   Step 5 - Results

The calibration results are illustrated in the following subsections. At first, we introduce a comparison of the offline results obtained with the the four models. After, we show the measured final accuracy obtained by using the *Geometric, Force and Thermal model* to control the end-effector pose.

6.5.1   Offline Calibration Results

For each model introduced in section 6.3, we used the Stepwise Regression algorithm to find the coefficients to fit the calibration set. Afterwards, we use the first validation set (in which temperatures, forces and poses are inside the calibration range) to fill Table 6.1 with the calibration results. Notice that the values used for the confirmation are not used to find the value of the coefficients. The results are presented for each axis in motor coordinates considering an interval of confidence of 90 % ($1.645\,\sigma$); we also give the number of parameters employed to allow such prediction. Finally, we show the computational time needed to calculate each complete model. In comparison with Case A, we improved the data processing performed before launching the Stepwise Regression algorithm. For this reason, even if we have a more complex model to find, the total computational time is lower than in the first case study.

For the pure geometric model we obtained a final accuracy in motor coordinates around ±0.5 μm on the three axes. This means that without keeping into account external forces and

Model →	G	G + F	G + T	G + T + F
q_1	±449 nm	±360 nm	±449 nm	±41 nm
$param_{q_1}$	13	18	13	22
q_2	±572 nm	±390 nm	±173 nm	±42 nm
$param_{q_2}$	12	21	24	24
q_3	±533 nm	±192 nm	±274 nm	±49 nm
$param_{q_3}$	12	19	25	27
Computational time	1.60 s	3.51 s	3.84 s	4.82 s

Table 6.1: *Error in predicting the validation set inside the calibration range using a pure geometric model (G), a geometric + force model (G + F), a geometric + thermal model (G + T) and a complete model (G + T + F). The number of parameters used to obtain this result for each axis and the computational time for each complete model is also indicated.*
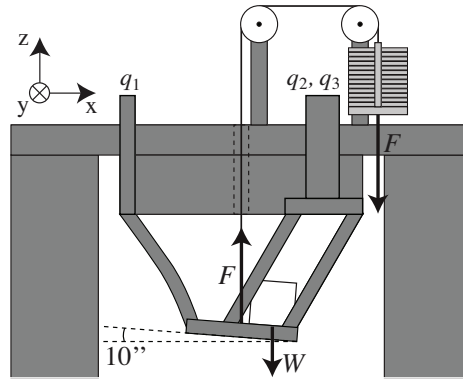
Figure 6.11: *Effect of the force on the robot geometry, when F=3.84 N and W=0.67 N.*

thermal effects, we can guarantee an end-effector positioning precision up to 1 μm.

For the models G + F and G + T, the explanation of the results need further investigation. As expected, the effect of the force is different on each axis. This happens because the force acting on the end-effector deforms the robot in a non-symmetric way. In fact, the cube mounted asymmetrically in respect to the center of mass and the force creates a momentum on the end-effector, which deforms the robot structure between the end-effector and the motor and causes a rotation of the end-effector of 10" around y axis (Figure 6.11). For example, notice that the prediction of q_1 for the model G + T is at the same level of model G. As the model G + T has no access to the force reading, it is not capable of handling such interaction. Also on q_3 we can find a way similar effect, but with reduced consequences. An effect on those results is also imputable to the Stepwise Regression algorithm falling in a local minimum.

The model G + T + F expresses the full predictive power of the calibration algorithm proposed in this thesis. By allowing the use of all the readings of the sources of inaccuracy, the Stepwise Regression is capable of predicting the set of data with an error under ±50 nm. In Figure 6.12 we plot the error in predicting the first validation set for the three axes. Finally, we tested this model on the second validation data set (having temperatures and forces out-

Figure 6.12: *Plot of the error in predicting the first validation set (points inside the calibration range).*
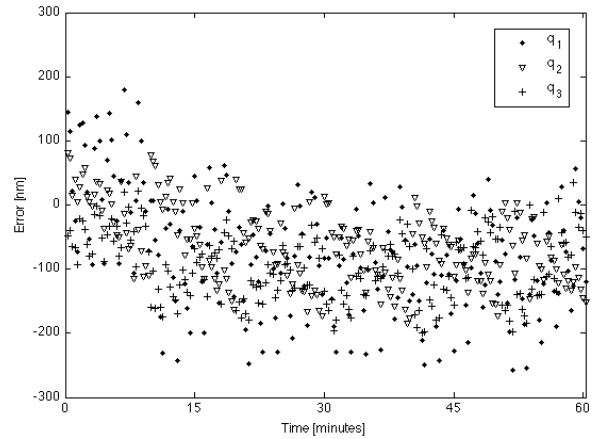
Figure 6.13: *Plot of the error in predicting the second validation set (points outside the calibration range).*

Axis	Force inside the calibration range	Force outside the calibration range
q_1	±41 nm	±164 nm
q_2	±42 nm	±97 nm
q_3	±49 nm	±93 nm

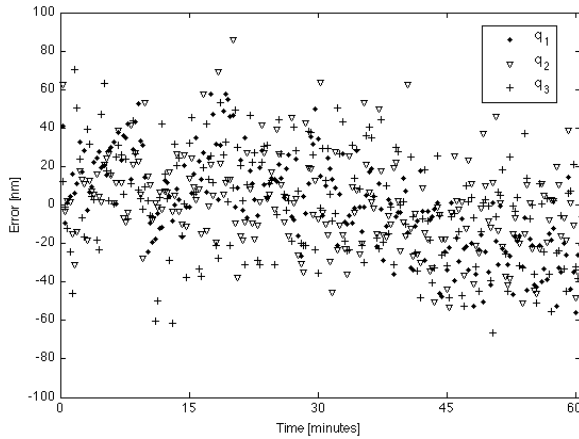Table 6.2: *Comparison of the error in motor coordinates obtained while applying a force inside the calibration range with an error outside the calibration range.*

side the calibration range). Logically, we expected a worse result than the previous one. In fact, we obtained an error in predicting the motor coordinates of ±164 nm on q_1, ±97 nm on q_2 and ±93 nm on q_3, considering a confidence interval of 90 % (Figure 6.13 and Table 6.2). With such results we demonstrate that the model is also effective outside its range, as the parametric approaches as the Stepwise Regression algorithm are known to be good in finding general solutions.

Also in this case, all the models considered here are linear in the parameters and non-linear in the variables. As the thermal behavior is responsible for changing the robot geometry during the time flow, the models G and G + F are time variant. On the other side, the thermal compensation cancel this effect, making the models G + T and G + T + F time invariant.

As done for Case A, cross parameters relevant to each case have been tested as well: cross thermal and geometric parameters have been tested for the model G + T and G + T + F, while cross force and geometric parameters have been employed for the model G + F and G + T + F. Also in this case all the cross parameters have been excluded by all the models suggesting once again that the thermal compensation act as a "moving offset", shifting the geometric model prediction dependently by the thermal changes. For this specific case, the force compensation behaves exactly like the thermal compensation, shifting the geometric model prediction dependently by the force applied on the end-effector.

Figure 6.14: *End-effector final positioning error.*

For a practical use of the robot, we can draw the following conclusions:

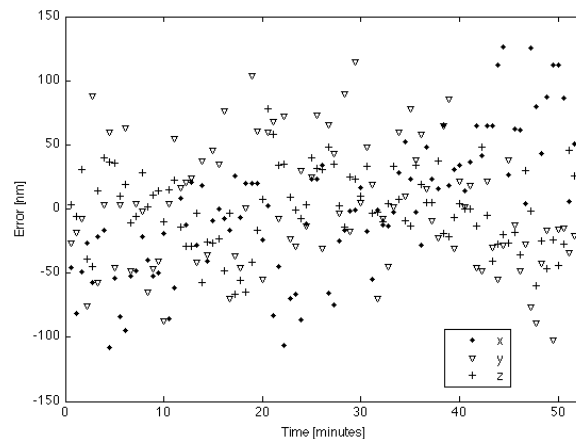- Forces acting on the robot can dramatically affect the final accuracy of a robot. They have to be compensated for depending on their value, the final accuracy required and the stiffness of the robot.

- Thermal effects must be imperatively compensated for applications that produce heat or for applications that last in time. In the case where a robot performs a fast industrial process without generating heat, it is possible to avoid thermal compensation by initializing the zero of the robot before starting each process, initializing *de facto* the offset due to thermal drift.

6.5.2 Online Calibration Results

To complete the evaluation of the model G + T + F and to allow a comparison between error in motor coordinates and error in end-effector coordinates, we performed the final online evaluation: we generated a trajectory file with 94 positions, we displaced the robot in each on them and we measured the end-effector position with the measuring system. A weight of 40 g was placed on the pan to simulate a force of the same order of magnitude of the μ-EDM process. Moreover, during the measurement the air temperature varied of ~0.6°C.

We obtained as a result an error of ±98 nm along x, ±81 nm along y and ±52 nm along z (Figure 6.14). This result represents the final accuracy reached by the system, while two sources of inaccuracy are acting on the robot. This result also proves that there is approximately a factor 2 between the error in motor coordinates and the corresponding error in end-effector coordinates. Furthermore we can see that with a complete calibration procedure, the ratio between motors resolution and final accuracy in motor coordinates is 1:10, while the ratio between motors resolution and final accuracy in end-effector coordinates is 1:20. This information will be useful for the development of new ultra-high-precision robots.

For this case only we can do a comparison with the results obtained by Dr. Fazenda in his thesis: as explained in the State of the art, in [27] the calibration of the Delta Cube 2 robot

(similar to the Agietron Micro-Nano) has been obtained after a measuring phase of 28 hours and a calibration time of 4 hours (for the fastest technique, the parameters research). The final accuracy obtained is in the order of ±100 nm, but concerns only the robot's geometric errors. In the current thesis for the Agietron Micro-Nano we obtained the same final accuracy, but after a measuring phase of 6 hours and a calibration time of only 5 seconds.

Even when two sources of inaccuracy deform the robot, we reached the same results attained by Dr. Fazenda in his thesis. By using our new calibration procedure we have been able to reduce the measuring time of 79% and the computational time of 99.97%, making the data processing time practically not influent on the overall calibration time.

In conclusion, thanks to those improvements *it is finally possible to use ultra-high-precision robots in an unsteady industrial environment while preserving the calibration accuracy*.

6.6 Conclusions

In this chapter we have demonstrated that the calibration algorithm proposed in this thesis is effective and capable of handling several sources of inaccuracy on robots with a complex structure. Specifically, we underline the following conclusions:

- In comparison with the classic robot calibration algorithm, we are able to perform the modeling and identification phases at the same time, saving time and by finding a simple model that already keeps in account the geometric errors of the robot.

- We tested four different models that keep in account one or more sources of inaccuracy acting on the robot. Such sources of inaccuracy have to be considered accordingly to the desired level of accuracy, the robot final application, its working environment, and its mechanical and physical properties.

- By using a complete model developed to compensate geometric, thermal and force effects, we obtained an absolute accuracy of less than ±50 nm in motor coordinates and ±100 nm in end-effector coordinates. The model is composed of 73 parameters.

- The calibration data has been collected in ~6 hours (considering half an hour for the stabilization of the interferometer base) and the data processing for the calibration took ~5 seconds. The measuring phase now represents the bottle-neck to shorten the calibration time.

- As underlined in the last section, in comparison with Dr. Fazenda *Delta Cube 2* calibration, we obtained the same accuracy even when 2 further sources of inaccuracy are acting on the robot. Moreover, we reduced the measuring time of 79% and the computational time of 99.97%.

- The calibration procedure proposed in this thesis allows the use of ultra-high-precision robots in unsteady industrial environments.

In the next chapter we will introduce the last case treated in this thesis: the calibration of a multiple robot system.

Chapter 7

Case C.1: 2-robot System Calibration

In this section we introduce the last and most complex case considered in this work: the calibration of the left-hand right-hand system composed by the robots Agietron Micro-Nano and MinAngle. The interest of this case lies in the fact that the calibration of a multiple ultra-high-precision robot system has never been performed before. We believe that the interaction of several ultra-high-precision robots is a crucial aspect to allow scaling of fabrication processes to the nanometer. We demonstrate that the calibration procedure introduced in Chapter 3 is suitable also for this case. To keep the explanation clear we splitted the description in two parts:

- Here we will describe the calibration of the two robots without keeping into account their interaction.

- In Chapter 8 we will complete the description of the calibration of the 2-robot system by adding the details regarding the nano-indentation process.

In both chapters we will discuss each step of the calibration procedure singularly. From a practical point of view, it is possible to perform the calibration in the same order as illustrated here, or by doing each same step of the two chapters at the same time (merging *Step 1* of Chapter 7 with *Step 1* of Chapter 8, and so on).

7.1 Step 1 - The Sources of Inaccuracy

The sources of inaccuracy are considered dependently on the robots characteristics and their final application. Additionally to geometric errors, for the case of *the Agietron Micro-Nano and the MinAngle performing nano-indentation* the next issues could play a role:

- Thermal effects,

- Parasitic degrees of freedom,

- External forces,

- Reference issues.

As we have seen in the other case studies, thermal issues play the predominant role in deforming the robot. In the next subsection, we will explain how we handle them as we did for the previous experiences.

We will also evaluate the parasitic rotations of the Agietron Micro-Nano and the parasitic translations of the MinAngle in order to mutually compensate for them. We will show in subsection 7.3 that - as soon as we can measure them - we can consider the parasitic DOF of a robot as any other source of inaccuracy: by seeing the problem in this way, we can use the calibration algorithm proposed in this thesis to compensate for this effect as well.

External forces and reference issues will be tackled in the next Chapter.

7.2   Step 2 - Measurements

In this subsection we will describe the measuring systems employed to perform the calibration of the two robots. The system proposed for Case B has been adapted to measure the two robots poses separately: a modular support system that allows mounting the three interferometers and the two autocollimators in two configurations has been developed. Furthermore, for the measuring of the MinAngle pose we developed a secondary measuring system able to enlarge the measuring stroke of interferometers and autocollimators, to the detriment of the measuring precision.

7.2.1   Common Parts

The measures on the two robots have be done in two separate experiences. Nevertheless, some parts of the measuring system are common to both cases.

First of all, each robot end-effector is equipped with a cube introduced in 4.2.3 on page 57. The cubes are glued before the measurement and they remain mounted on the system even after the end of the measuring phase. Since between the two robots we will mount the indentation system, the Agietron Micro-Nano's cube is mounted *on* the end-effector, while the MinAngle's cube is mounted *under* the end-effector. To allow the use of the modular supports, the cube of the MinAngle robot has been also mounted asymmetrically as the one of the Agietron Micro-Nano (Figure 7.9 on page 94).

Furthermore, in order to measure the MinAngle with the autocollimators, we added three parts to raise all the system of 50 mm. Thus, to allow gluing a 45° mirror for measuring θ_y for the Agietron Micro-Nano, we added three other parts that increase the distance between the two robots of 14 mm (Figure 7.1). In total the system has four 45° mirrors. Their position will be detailed in the following subsections.

Seven *pt1000* thermal sensors have been glued on selected parts of the system to monitor their temperature (Figure 7.1): sensors *5, 6,* and *7* are glued on the three supports of the robots. These parts are important because they sustain the two robots and the screws of the MinAngle motors. Sensors *4* and *8* are respectively mounted on the bottom base and the top base of the system. Those parts are also significant, since they support the system. Furthermore, the top base is close to the six motors of the robots, so it is very important to monitor
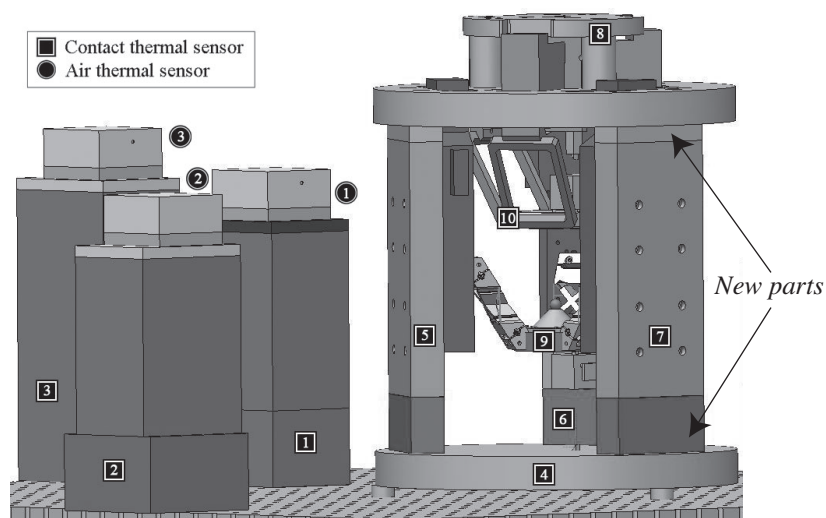
Figure 7.1: *Position of the thermal sensors on the system and parts added to allow using the measuring devices.*

its temperature. Finally sensor *9* and sensor *10* are respectively fixed on the structure of the MinAngle and on the structure of the Agietron Micro-Nano.

Three other *pt1000* sensors (two in the case of the MinAngle) are used to measure the temperature of the interferometers supports. As their measure is used to stabilize the supports and their information do not express the drift of the robots, their reading will not be used for calibration.

Finally, three *pt100* thermal sensors are placed to measure the air temperature near each interferometer and are used to correct the measuring drift caused by changes in the air refraction index.

As for Case B, even if each robot has only 3 DOF, we measure all the 6 DOF, in order to compensate for the systematic errors and to evaluate and model the parasitic DOF of each robot.

7.2.2 MinAngle Measuring System

The MinAngle has an angular stroke of ±5°. The measuring system used for case B is not able to cover such rotations; in fact the autocollimator has an angular stroke of only ±400" (corresponding to ±0.11°). Furthermore, the interferometer loses the signal when rotations over 200" are performed[1]. For those reasons, we used a secondary measuring device to enlarge the stroke of the measuring system, to the detriment of the measuring precision. The idea is to build two calibrated model of the MinAngle, one that covers all the working volume with

---

[1]Since the interferometer has a relative zero, this is a major problem. In fact, after losing the signal, it is not enough to return to a measurable position to have a good measure again. It is necessary to re-initialize the zero and start the measure again. As in our case the zero of the system is "visible" only at the beginning of the measures (since it is coupled to the thermal sensors reading), a signal lost will result in restarting the measures from the beginning. This problem does not concern measuring instruments with an absolute zero, such as the autocollimator, the touch probe or the inclinometer.
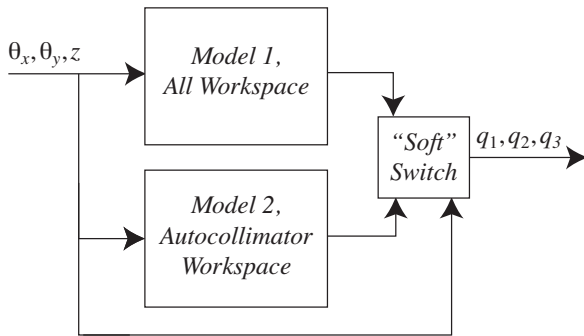
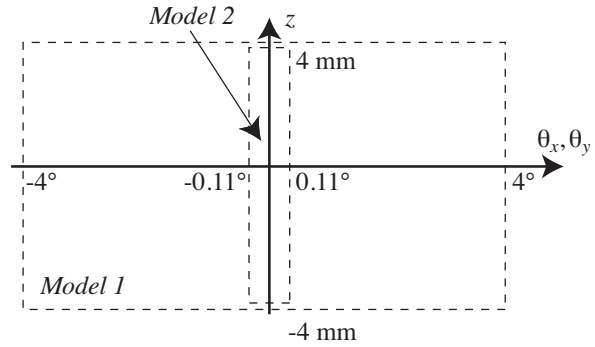Figure 7.2: *The different models used to control the MinAngle end-effector pose.*

Figure 7.3: *The covering of the two models on the MinAngle's workspace.*

an average precision, and another to move the robot with ultra-high-precision in a limited working volume (Figures 7.2 and 7.3). A "soft switch" will be programmed to perform a gentle transition between both models.

We will describe the two systems in the order in which they have been used.

7.2.2.1   Large Stroke Measuring System

With this measuring system we acquire the pose for only the controllable DOF of the robot: θ_x, θ_y and z, measured once per time. The data acquired with this system will allow us to build an averagely calibrated model of the robot, covering all the robot workspace.

We use the touch probe to measure translations along the vertical axis (Figure 7.4). As it is not possible to perfectly align the touch probe frame with the frame of the interferometer that will measure the vertical axis, we rectify the measure acquired with the touch probe. To do so, in some previous measurements we established a coordinate transformation to "align" the touch probe frame to the interferometer frame (Figure 7.6).

Even if the touch probe has a resolution of 50 nm, the measures acquired with it are corrupted with an error of 1-2 μm. The source of this error is the dry friction generated by the contact between the tip of the measuring device and the robot end-effector.

Rotations are measured in two times using the inclinometer (Figure 7.5). The inclinometer is simply installed on the robot end-effector, once to measure the rotations around axis x, and once again to measure rotations around axis y. We acquired some preliminary measurements with the autocollimators to see as well if a "rectification" was needed. In this case this is not necessary, since the measuring differences between the two instruments fell under the resolution of the inclinometer.

7.2.2.2   Ultra-High-Precision Measuring System

This system is similar to the one used for Case B. In fact, it also includes 3 interferometers and 2 autocollimators (Figure 7.7). The only difference with the previous case lies in the use of a new 45° mirror to reflect one autocollimator beam (Figure 7.8). This is done because the facet of the cube needed to measure θ_y in not directly accessible, as the structure of the
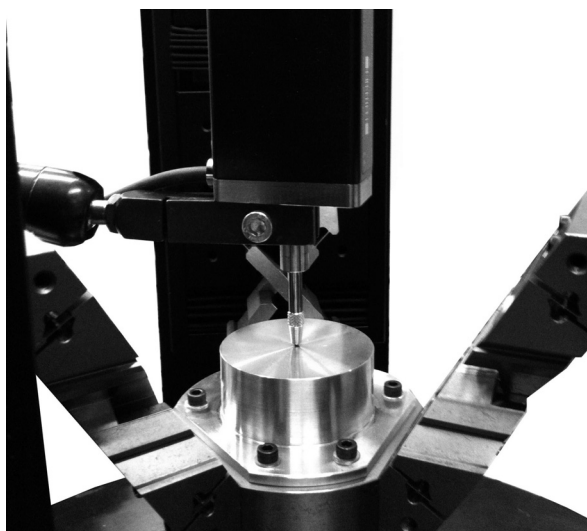
Figure 7.4: *A picture of the touch probe while measuring the translations along the vertical axis.*
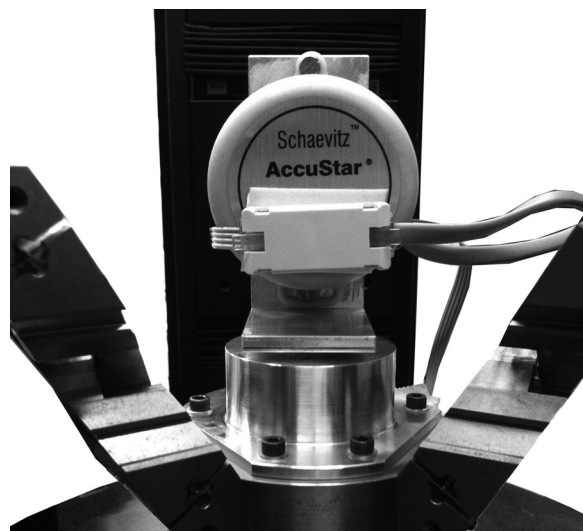

Figure 7.5: *The Inclinometer mounted on the MinAngle end-effector to measure rotations around y axis.*

MinAngle and its linear motors are in the way. The introduction of this mirror, which causes a longer path that the light has to cover to reach the cube, is responsible for the appearance of a small thermal drift in the reading exclusively of θ_y. This drift is completely linked to the measuring system and not to the robot, so it can be easily suppressed.

Also in this case all the interferometers are mounted horizontally; another 45° mirror is used to reflect the interferometer beam and measure the vertical axis (Figure 7.9).

We will use the autocollimators to perform a "fine" calibration of the rotations, while we will use the interferometers only to characterize the parasitic translations of the robot.

7.2.2.3 Measurement Procedure

The measuring procedure for this case is the most complex of this thesis. This is due to the fact that the measurements taken with different instruments must be consistent enough to be used together and because calibration is performed twice, one of which is done between two measurements. The complexity of this phase underlines the lack of ultra-high-precision measuring devices with large strokes and capability of measuring multiple DOF on the market.

The procedure is divided in three parts:

1. *Model 1* - All-the-workspace calibration:

   (a) A trajectory grid of motor coordinates[2] is generated and measured firstly with the touch probe, then with the inclinometer towards θ_x, and finally with the inclinometer to measure θ_y.

---

[2]The motor coordinates explored are the following: -4 -2 0 2 4. The points generated in this way are: -4 -4 -4, -4 -4 -2, -4 -4 0, ... , 4 4 4.

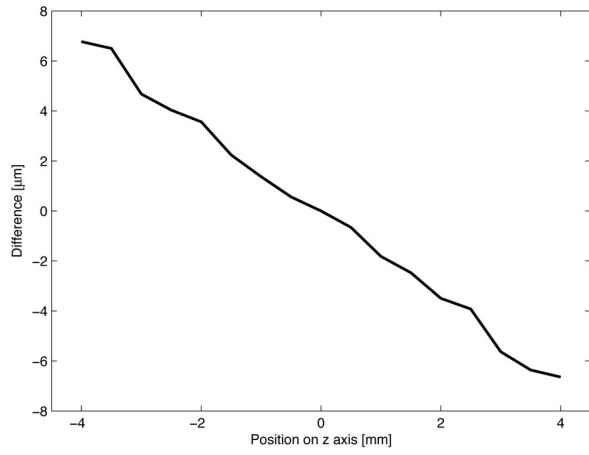Figure 7.6: *Difference in measuring the MinAngle vertical translation with the interferometer and with the touch probe.*
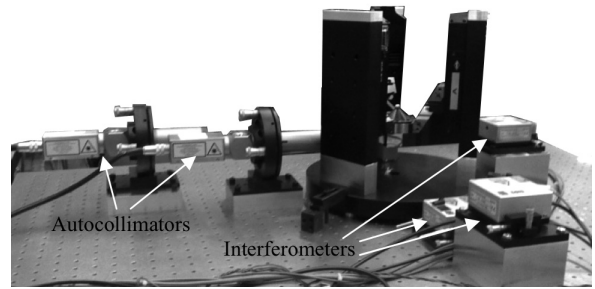

Figure 7.7: *A picture of the measuring system for the MinAngle (in this picture the Agietron Micro-Nano is not mounted).*
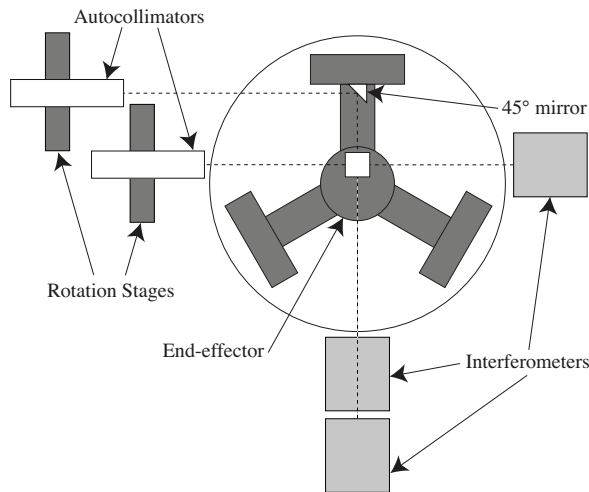

Figure 7.8: *Top view of the MinAngle measuring system with the laser beam paths.*
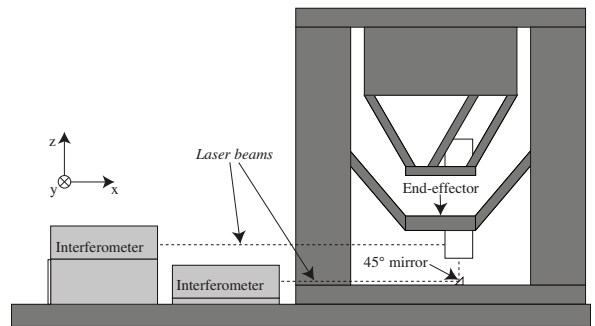

Figure 7.9: *Right view of the MinAngle measuring system with the laser beam paths.*

(b) The interferometer is used to rectify the measure of the touch probe[3].

(c) The data gathered is used in Matlab to build a geometric model of the robot, *Model 1*.

(d) The model is implemented in the controller and a validation measure[4] is performed.

2. *Model 2* - Autocollimator workspace calibration:

(a) While using *Model 1*, we explore a regular trajectory file of 343 positions (rotations limited to ±300"). Afterwards, we measure a validation set of 216 positions. The measures in this phase are performed using the two autocollimators and the touch probe.

(b) The data gathered is used in Matlab to build a new geometric model of the robot - *Model 2* - with a smaller working volume but more accurate in rotations.

(c) The validation set is calculated with *Model 2* and used to move the robot in such points, in order to measure the final accuracy of the robot.

(d) The "soft switch", which will handle the transition between the two models, is implemented and activated. For angles that are higher than ±400" *Model 1* is used. For angle that are smaller than ±400" *Model 2* is used. For angles between 350" and 300", -300" and -350" the "soft switch" will balance the two models by using a weight coefficient.

3. *Parasitic Model* - Parasitic translations modeling:

(a) Using *Model 2*, the MinAngle is displaced along z axis performing "pure" translations (on a trajectory file of 17 points). This trajectory is repeated many times during some hours, in order to measure the thermal drift due to the environmental thermal changes. The interferometers and the autocollimators measure the end-effector pose.

(b) A model of the parasitic deformation towards the z position of the end-effector and the temperature is established.

Notice that if a system capable of measuring translations with ultra-high precision while performing rotations in the order of 1-2° existed, this procedure would have been easier and faster. This experience underlines the lack of ultra-high-precision measuring devices capable of handling several DOF.

---

[3]A trajectory of vertical translations have been generated for this purpose (-4 -4 -4, -3.5 -3.5 -3.5, ... , 4 4 4). The difference in the measurement of the interferometer and the touch probe can be seen in Figure 7.6. Two coefficients have been identified to transpose the reading of the touch probe in the frame of the interferometer measuring the vertical axis.

[4]We built a trajectory file of rotations around the point 0, with intervals of 0, ±1.5° and ±3° on the angular axes, obtaining a 25 points validation set.
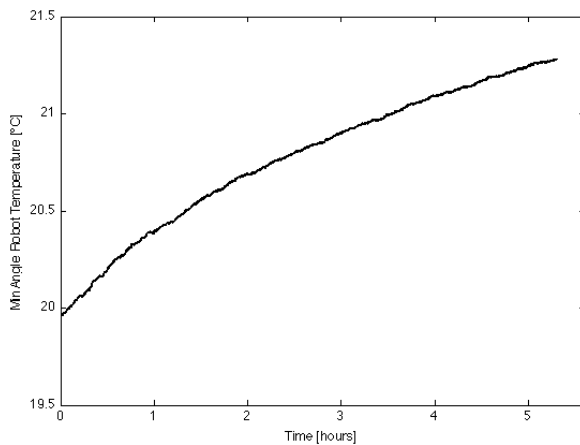
Figure 7.10: *Evolution of the MinAngle temperature during the measurement (thermal sensor 9 in Figure 7.1).*
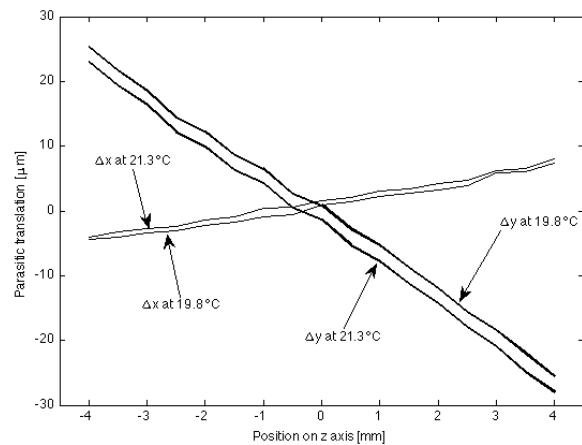
Figure 7.11: *Plot of the parasitic translations along x and y axes, at 19.8°C and 21.3°C.*

Notice also that in point 2.(a) we decided to use the touch probe and not the interferometer to measure the vertical axis position. This is due to the fact that our rotations performed here were already too wide in comparison with the one accepted by the interferometer.

An evaluation of the time cost of each part is given:

- Part 1 took in total 2.5 hours: 2 hours for the two measurements with the inclinometer, 20 minutes for the measurements with the touch probe and less than 10 minutes for measuring with the interferometer.

- The overall time cost to acquire the whole dataset of part 2 is 3 hours; 1.5 hours for the measure with the autocollimators and 1.5 hours for the measure with the touch probe.

- The dataset of Part 3 has been acquired during 5 hours of measurement.

Finally, we underline some details about Part 3. In Figure 7.10 we show the evolution of the robot temperature during the 5 hours of measurement (corresponding to the measure of sensor 9 in figure 7.1). During this time interval, the temperature varies from ~19.8°C to ~21.3°C. In Figure 7.11 and Table 7.1 we show the parasitic translations of the robot, extended between ±7 μm along the axis x and ±27 μm along y. Notice that the parasitic translations are temperature related; again in Figure 7.11, we show the parasitic translations at 19.8°C and at 21.3°C. On a thermal change of ~1.5°C, we have a difference in the parasitic translation of ~1 μm along axis x and ~2.5 μm along axis y. This proves that the thermal effects have to be kept in account while modeling the parasitic translations of the MinAngle.

7.2.3 Agietron Micro-Nano Measuring System

The measuring system used here is very similar to the one of Case B (Figure 7.12). As for the MinAngle case, the only difference lies in the use of a 45° mirror to measure the rotations around θ_y (Figure 7.13). The motivation that brought us to this solution is the lack of free

	Parasitic translations	Drift due to ~1.5°C thermal variation
Axis x	±7 μm	~1 μm
Axis y	±27 μm	~2.5 μm

Table 7.1: *Parasitic translations and drift depending on the thermal variations on each horizontal axis of the MinAngle.*
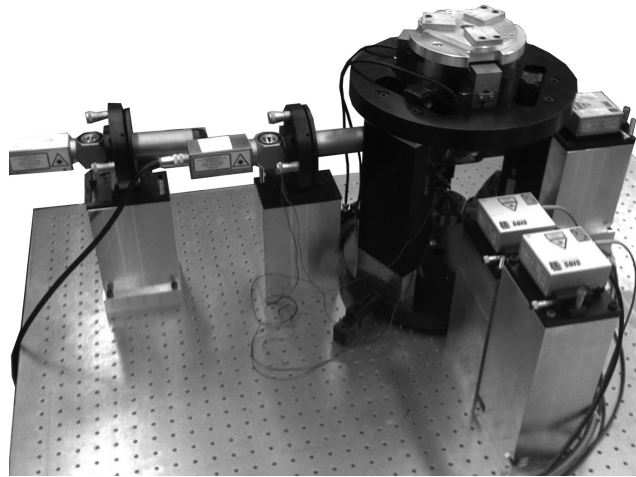
Figure 7.12: *The measuring system used for the Agietron Micro-Nano.*
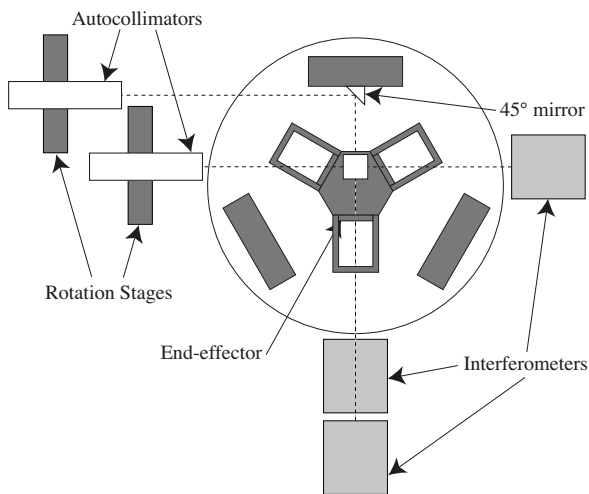
Figure 7.13: *Top view of the Agietron Micro-Nano measuring system with the laser beam paths.*
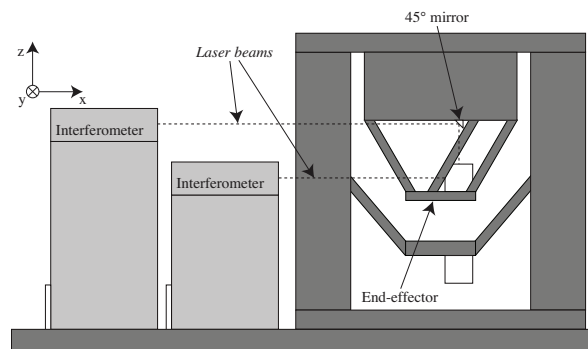
Figure 7.14: *Right view of the Agietron Micro-Nano measuring system with the laser beam paths.*

space around the robot. Also in this case we found a small thermal drift in the reading of θ_y, that is easily suppressed.

The 45° mirror to measure the vertical axis of the robot is also used in this case (Figure 7.14).

7.2.3.1   Measurement Procedure

Also the measuring procedure employed here is similar to the one introduced in subsection 6.2.2 on page 77. The only difference lies in the fact that no weights have been changed during the measurements.

To study exclusively the thermal behavior of the robot, we have measured the robot pose while the environmental temperature was changing. Also in this case, we used the AC to simulate the free oscillation of an industrial environment in the following way: before starting the measuring session, the AC setpoint was adjusted to 20 °C. When this low temperature was reached we turned off the AC and started acquiring the measurements. In a period of 5.5 hours the robot temperature augmented by ~1.5°C (Figure 7.15).
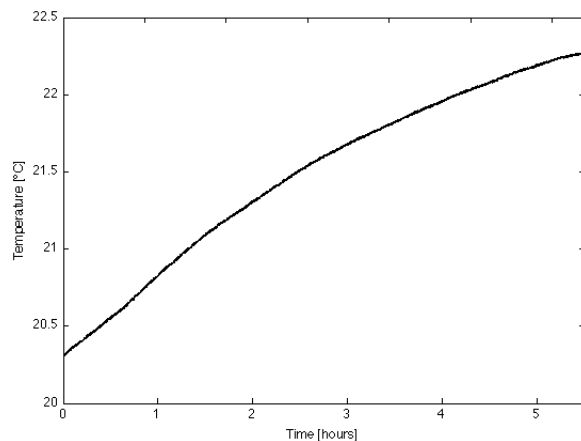
Figure 7.15: *Temperature of the Agietron Micro-Nano during the measuring (thermal sensor 10 in Figure 7.1).*
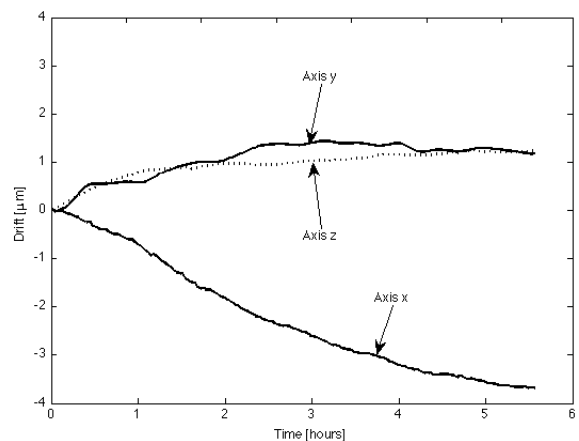
Figure 7.16: *Evolution of the zero drift during the measuring of the Agietron Micro-Nano.*

We generate two regular grids of end-effector poses:

- The calibration grid, composed by 252 positions. A grid of $6 \times 6 \times 6$ motor coordinates positions (in 0, 0.5, 1.0, 1.5, 2.0, 2.5 mm) and a return to zero when every line is completed (36 return to zero in total).

- The validation grid, composed by 150 positions. A grid of $5 \times 5 \times 5$ motor coordinates positions (in 0.25, 0.75, 1.25, 1.75, 2.25 mm) and a return to zero when every line is completed (25 return to zero in total).

We measured two calibration grids, a validation grid, and again two calibration grids. In total we acquired 1158 positions during a time lapse of 6.5 hours. We used the four calibration

grids to build the *calibration set* (composed by 1008 points) and the remaining points (150) to build the *validation set*.

With the purpose of checking the quality of the data, also in this case we acquired four interferometer measurements for each point and we calculated the standard deviation. This value was never superior to 20 nm.

In Figure 7.16 we show the evolution of the zero while measuring translations.

7.3 Step 3 - Calibration

Unlike Case A and Case B, here we will obtain several models that – used together – will allow the operation of the 2-robot system with ultra-high precision. Specifically, we will see in the order three models derived from the MinAngle measures (the large stroke model, the ultra-high-precision model and the parasitic translations model) and two models derived by the Agietron Micro-Nano measures (the ultra-high-precision model and the parasitic rotations model).

7.3.1 MinAngle Calibration

As we have seen in sub-subsection 7.2.2.3, because of the lack of measuring devices on the market, the calibration procedure for the MinAngle is complicated. We follow here the steps of the procedure introduced previously and we show the models that have been used for the calibration.

7.3.1.1 Large Stroke Calibration

This is the first model that will allow a calibrated use of the MinAngle (Figure 7.17). From a mathematical point of view, it is very similar to the "pure" geometric model introduced in 6.3.1. The difference lies in the input of the model that is composed of 2 rotations and one translation (θ_x, θ_y, z) instead of three translations (x, y, z):

$$q_1, q_2, q_3 = f(\theta_x, \theta_y, z) \tag{7.1}$$

$$\theta_x, \theta_y, z \quad \longrightarrow \quad \boxed{\begin{array}{c} Model \\ MinAngle \end{array}} \quad \xrightarrow{q_1, q_2, q_3}$$

Figure 7.17: *The Large Stroke MinAngle model.*

Also in this case, we separate the model 7.1 in three parts and we calibrate each axis separately:

$$\begin{cases} q_1 = f(\theta_x, \theta_y, z) \\ q_2 = f(\theta_x, \theta_y, z) \\ q_3 = f(\theta_x, \theta_y, z) \end{cases} \tag{7.2}$$
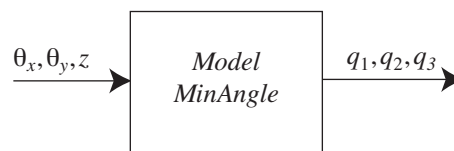
For each axis we generate new correlation variables, obtained by element-by-element multiplication of the three vectors of measures (Θ_x, Θ_y, Z, terms of 1st order measured respectively with the inclinometer for the first two vectors and the touch probe for the last one). We obtain the following new terms of 2nd and 3rd order:

- 1st order: Θ_x, Θ_y, Z

- 2nd order: $\Theta_x^2, \Theta_y^2, Z^2, \Theta_x\Theta_y, \Theta_x Z, \Theta_y Z$

- 3rd order: $\Theta_x^3, \Theta_y^3, Z^3, \Theta_x\Theta_y Z, \Theta_x^2\Theta_y, \Theta_x^2 Z, \Theta_y^2\Theta_x, \Theta_y^2\Theta_x, \Theta_y^2 Z, Z^2\Theta_x, Z^2\Theta_y$

The model that Stepwise Regression has to fit to calibrate the axis q_1 is the following:

$$\begin{aligned} Q_1 = \ & a_1\Theta_x + a_2\Theta_y + a_3 Z + a_4\Theta_x^2 + a_5\Theta_y^2 + a_6, Z^2 + a_7\Theta_x\Theta_y + a_8\Theta_x Z + a_9\Theta_y Z + \\ & + a_{10}\Theta_x^3 + a_{11}\Theta_y^3 + a_{12}, Z^3 + a_{13}\Theta_x\Theta_y Z + a_{14}\Theta_x^2\Theta_y + a_{15}\Theta_x^2 Z + a_{16}\Theta_y^2\Theta_x + \\ & + a_{17}\Theta_y^2\Theta_x + a_{18}\Theta_y^2 Z + a_{19}Z^2\Theta_x + a_{20}Z^2\Theta_y + a_{21} \end{aligned} \tag{7.3}$$

Stepwise Regression will find the $a_1, \ldots, a_{21}$ values to fit the relation 7.3:

$$(a_1, \ldots, a_{21}) = stepwise\left(\left[\begin{bmatrix} \theta_{x,1} \\ \vdots \\ \theta_{x,m} \end{bmatrix}\begin{bmatrix} \theta_{y,1} \\ \vdots \\ \theta_{y,m} \end{bmatrix}\begin{bmatrix} z_1 \\ \vdots \\ z_m \end{bmatrix}\cdots\begin{bmatrix} z_1^2\theta_{y,1} \\ \vdots \\ z_m^2\theta_{y,m} \end{bmatrix}\right], \begin{bmatrix} q_1 \\ \vdots \\ q_m \end{bmatrix}\right)$$

Where $m = 125$ corresponds to the number of measurements used in this case. An additional set of 8 confirmation points has been taken for offline validation.

Also in this case, to completely calibrate the robot, the parameters research has to be done for each motor axis.

The data processing to perform this phase took less than one second.

7.3.1.2   Ultra-high-precision Calibration

The model described in the last sub-subsection is here used to displace the robot within the course of the autocollimators (±400"). Results about the calibration of the previous model will be shown in 7.5.1.1 on page 104.

Two dataset has been established: a calibration set composed of 343 points (rotations in 300, 200, 100, 0, -100, -200, -300", vertical translation in 3, 2, 1, 0, -1, -2, -3 mm) and a validation set composed of 216 points (rotations in 250, 150, 50, -50, -150, -250", vertical translation in 2.5, 1.5, 0.5, -0.5, -1.5, -2.5 mm).

Rotations are measured using the autocollimators while translations are still measured using the touch probe (as said before, because of the rotations the interferometer will loose the signal).

The mathematical model used to fit the data is exactly the same as on the large stroke calibration case (Equation 7.3 and Figure 7.17).

Regarding computational time, also in this case the calibration took less than one second.

7.3.1.3 Model of Parasitic Translations

Here the goal is to find a model that, given the vertical position of the end-effector z and the robot temperature, is able to predict the parasitic translation of the end-effector along the two horizontal axes, Δx and Δy (Figure 7.18). We can express such model in this way:

$$\Delta x, \Delta y = f(z, t_{MinAngle}) \tag{7.4}$$
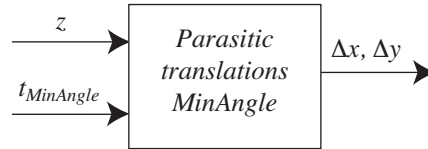
Figure 7.18: *The MinAngle parasitic translation model.*

We split again the model in two separate equations:

$$\begin{cases} \Delta x = f(z, t_{MinAngle}) \\ \\ \Delta y = f(z, t_{MinAngle}) \end{cases} \tag{7.5}$$

For each axis, the model that Stepwise Regression will fit is the following:

$$\Delta x = a_1 z + a_2 z^2 + a_3 z^3 + a_4 + a_5 t_{MinAngle} \tag{7.6}$$

The algorithm will be called in this way:

$$(a_1, \ldots, a_5) = stepwise \left(\left[\begin{bmatrix} z_1 \\ \vdots \\ z_m \end{bmatrix} \cdots \begin{bmatrix} t_{MinAngle1} \\ \vdots \\ t_{MinAnglem} \end{bmatrix} \right], \begin{bmatrix} \Delta x_1 \\ \vdots \\ \Delta x_m \end{bmatrix} \right) \tag{7.7}$$

To perform the measures to find this model we used the ultra-high-precision model obtained in the previous phase. Before starting the measures we turned on the AC and waited to reach the lowest temperature. Then, during a period of 5 hours we displaced the robot on the vertical axis without rotating, by moving the three motor axes at the same articular coordinates: 4.0, 3.5, 3.0, 2.5, 2.0, 1.5, 1.0, 0.5, 0.0, -0.5, -1.0, -1.5, -2.0, -2.5, -3.0, -3.5, -4.0. The rotations around the three axes are never superior to ±5".

In total, 664 measures have been acquired and divided in a calibration set (composed by 332 points with the following articular coordinates: 4.0, 3.0, 2.0, 1.0, 0.0, -1.0, -2.0, -3.0, -4.0) and a validation set (corresponding to the remaining ones).

The data processing to perform to find this model took 0.26 seconds.

7.3.2   Agietron Micro-Nano Calibration

7.3.2.1   Geometric and Thermal Ultra-high-precision Calibration

To perform the calibration of the Agietron Micro-Nano we used the model G + T introduced in 6.3.3 on page 81. We recall here the Equation 6.7 that describes the calibrated model:

$$q_1, q_2, q_3 = f(x, y, z, t_4, \ldots, t_{10})$$

The only difference in comparison with what has been seen in Chapter 7 is that the thermal sensors are placed in the configuration shown in Figure 7.1.

7.3.2.2   Model of Parasitic Rotations

We use a part of the data used for calibration to find a model that describes the parasitic rotations of the robot (Figure 7.19). In this case we do not consider the temperatures, since they have a negligible influence on the measure of rotations:

$$\Delta\theta_x, \Delta\theta_y, \Delta\theta_z = f(x, y, z) \tag{7.8}$$
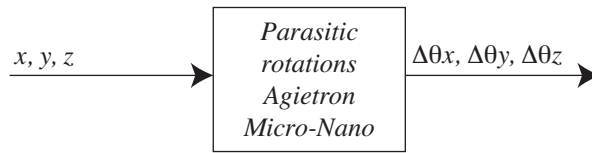
Figure 7.19: *The Agietron Micro-Nano parasitic rotations model.*

Even if the rotations around θ_z cannot be compensated by the MinAngle, we will predict them as well for the sake of the argument.

We split again the model described by Equation 7.8 in three parts:

$$\begin{cases} \Delta\theta_x = f(x, y, z) \\ \Delta\theta_y = f(x, y, z) \\ \Delta\theta_z = f(x, y, z) \end{cases} \tag{7.9}$$

For each rotational axis, the Stepwise Regression will fit the following relationship:

$$\begin{aligned} \Delta\theta_x \;=\; & a_1 X + a_2 Y + a_3 Z + a_4 X^2 + a_5 Y^2 + a_6, Z^2 + a_7 XY + a_8 XZ + a_9 YZ + \\ & + a_{10} X^3 + a_{11} Y^3 + a_{12}, Z^3 + a_{13} XYZ + a_{14} X^2 Y + a_{15} X^2 Z + a_{16} Y^2 X + \quad (7.10) \\ & + a_{17} Y^2 X + a_{18} Y^2 Z + a_{19} Z^2 X + a_{20} Z^2 Y + a_{21} \end{aligned}$$

Stepwise Regression will be called in Matlab in this way:

$$(a_1,\ldots,a_{21}) = stepwise\left(\left[\begin{bmatrix} x_1 \\ \vdots \\ x_m \end{bmatrix}\begin{bmatrix} y_1 \\ \vdots \\ y_m \end{bmatrix}\begin{bmatrix} z_1 \\ \vdots \\ z_m \end{bmatrix}\cdots\begin{bmatrix} z_1^2 y_1 \\ \vdots \\ z_m^2 y_m \end{bmatrix}\right], \begin{bmatrix} \Delta\theta_{x,1} \\ \vdots \\ \Delta\theta_{x,m} \end{bmatrix}\right) \quad (7.11)$$

We use the first calibration grid to find the parameters (252 points, therefore $m = 252$) and the validation set to confirm the calibration (150 points).

7.4 Step 4 - Model Added to the Robot Controller

In our case, the same real-time computer controls both robots. This makes synchronization between the two robots easier. The motor coordinates for the two robots are generated in the measuring computer using the complete model of Figure 7.20.

After that, the motor coordinates are sent to the controlling computer. In an industrial application, the model will be implemented directly in the controlling computer. In this case, the calculations related to geometric parameters and parasitic compensation will be done in a real-time process. Meanwhile, the contribution of the error coming from the thermal effects will be calculated in a standard process.
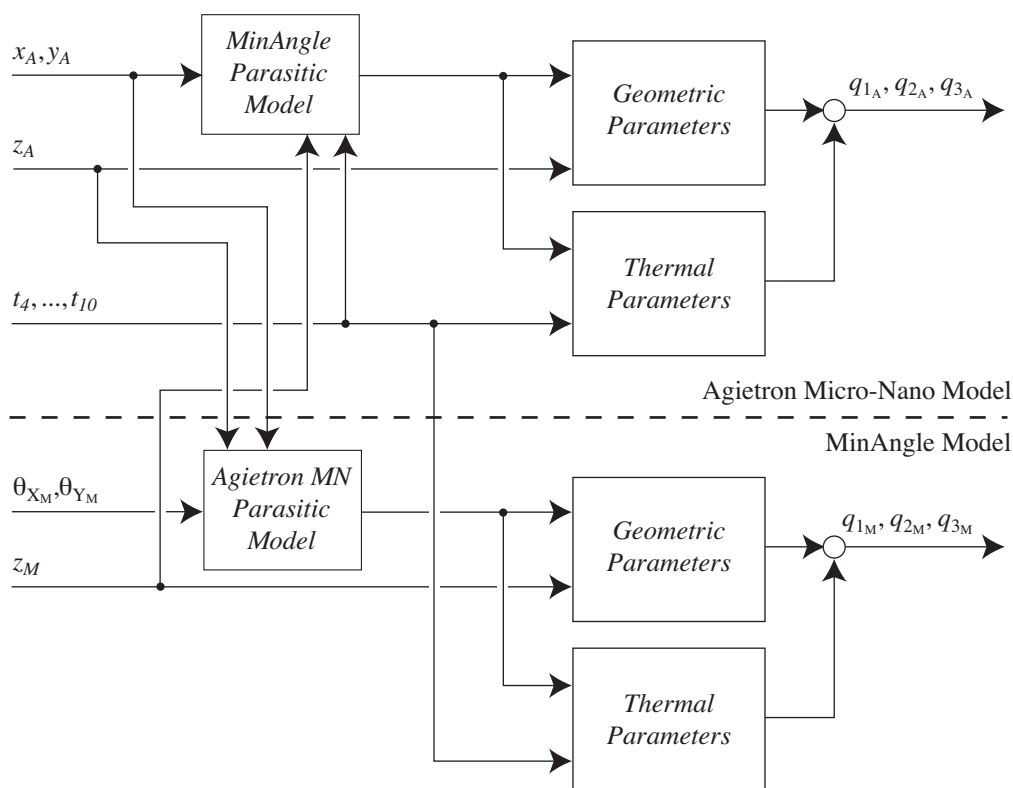
Figure 7.20: *The overall calibrated model used to control the 2-robot system.*

The *MinAngle parasitic model* takes in input the end-effector position of the MinAngle $(\theta_{X_M}, \theta_{Y_M}, Z_M)$, the current horizontal pose of the Agietron Micro-Nano (X_A, Y_A) and the reading of the MinAngle's temperatures. By using those entries the model is able to calculate the Agietron Micro-Nano horizontal values in order to compensate the parasitic translations (*e.g.* the MinAngle end-effector is displaced to $\theta_{X_M} = 0$, $\theta_{Y_M} = 0$, $Z_M = 3$. The MinAngle parasitic model calculates a parasitic displacement of the end-effector of 3 μm along x axis and a displacement of -2 μm along y axis. Those two values are added to the current position of the Agietron Micro-Nano).

The *Agietron Micro-Nano parasitic model* works exactly in the same way but it returns the angles along the horizontal axes that the MinAngle has to add to its actual pose to correct the parasitic rotations of the Agietron Micro-Nano. Notice that the rotations along the vertical axis are not correctable.

7.5   Step 5 - Calibration Results

In this section we present the calibration results for the two robots separately. As said before, the models implemented here are capable of compensating for thermal effects and issues related to parasitic DOF. The interaction between the two robots, the nano-indentation system and the final accuracy reached by the system will be presented in Chapter 8.

7.5.1   MinAngle Calibration Results

7.5.1.1   Large Stroke Model
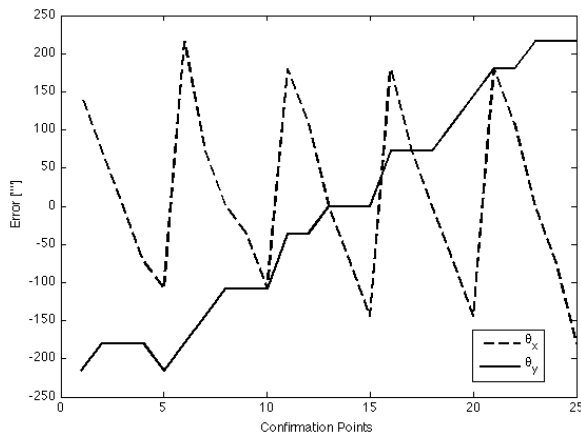
Figure 7.21: *MinAngle rotation error while performing rotation between ±3° around the zero.*
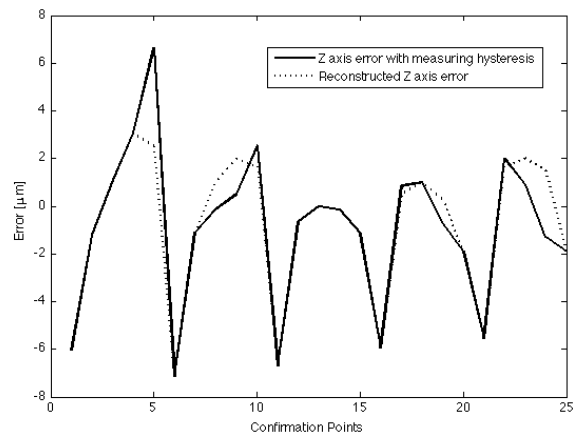
Figure 7.22: *MinAngle vertical translation error when rotating between ±3° around zero.*

In order to have an online validation, the large stroke model has been implemented in the controller and 25 rotations around the zero have been performed: a combination of rotations of -3, -1.5, 0, 1.5 and 3° have been measured with the inclinometer and the touch probe. The

results are a rotation error up to ±200" (Figure 7.21) around both rotation axes and a vertical translation error of around ±5 μm (Figure 7.22).

Notice how the error in Figure 7.21 is regular. Regularity in the error is a typical sign of a calibration that has not been completely concluded. Especially for θ_y we can see that the measured error forms a line. This means that there is some information that has not been used to calibrate the robot. To find the reason why the Stepwise Regression was not able of better fitting the data, it is enough to observe Figure 7.22. Notice that here the data is no more regular, suggesting the reason why the algorithm could not converge anymore. The hysteresis caused by the touch probe reading starts to be too important at this level, not allowing a closer description of the robot geometry. As we have explained in 3.3 on page 43, it is possible to visually check the quality of data. In Figure 7.22 we observe peaks that prove the low quality of this measure: all the variables in the model that are multiplied by the Z column inherit a similar error, which in the end limits the convergence of the Stepwise Regression algorithm. The dotted line represents a reconstruction of the measure without the hysteresis (i.e. how the data should have been to obtain better results).

This again justifies the use of a secondary model, more precise than the first.

7.5.1.2 Ultra-high-precision Model

The calibration data has been used to fit the model, while the validation data is used to confirm its prediction capability. We show here the online results of the calibration: we displaced the robot in the points of the validation set and we measured with the autocollimators and the touch probe the pose of the end-effector.
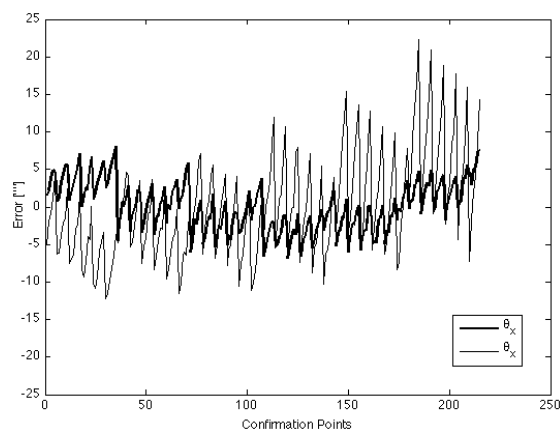
Figure 7.23: *MinAngle rotation error while rotating ±350" in the vertical positions 2.5, 1.5, 0.5, -0.5, -1.5, -2.5 mm.*
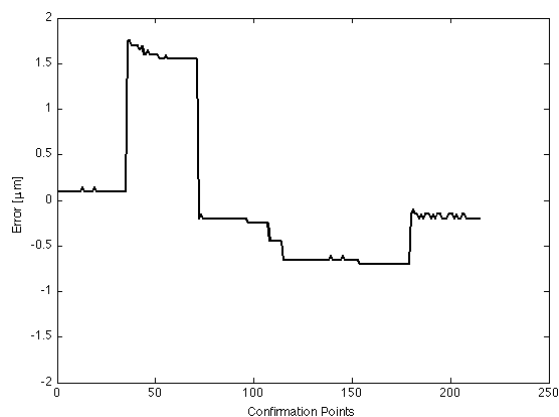
Figure 7.24: *MinAngle vertical translation error while performing rotation between ±350" in the vertical positions 2.5, 1.5, 0.5, -0.5, -1.5, -2.5 mm.*

Figure 7.23 shows the error in rotations. We have ±5" error for θ_x and ±11" error for θ_y. In comparison with the large stroke model, rotational accuracy has been improved of a factor 20 (see Table 7.2). Nevertheless, also in this case we can see some regular paths in the data, suggesting that the model cannot converge at the maximum of its capabilities. Once again,

the cause of this are the measures with the touch probe: Figure 7.24 illustrates the error in translation while rotation around the points 2.5, 1.5, 0.5, -0.5, -1.5, -2.5 mm. Also in this case we can clearly distinguish the measuring error due to the contact friction (the error measured ideally would have been 5 straight lines), compromising the prediction capability of the entire model. The measured error in translation along the vertical axis in the 90% of the dataset is ±1.1 μm, corresponding to a factor 5 improvement in comparison with the large stroke model.

Axis	Large Stroke Model	Ultra-high-precision Model
θ_x	±200"	±5"
θ_y	±200"	±11"
z	±5 μm	±1.1 μm

Table 7.2: *Overall MinAngle calibration results.*

7.5.1.3   Parasitic Translations Model

Stepwise Regression was able to find the 10 parameters to fit the model of Equation 7.6. For the calibration set, the parasitic rotations were predicted with a maximum error of ±390 nm along axis x and ±293 nm along axis y, on the 90% of the points. Regarding the validation set, the error was ±417 nm along x axis (Figure 7.25) and ±403 nm along y axis (Figure 7.26) on the 90% of the points. A comparison of the two errors is given in Table 7.3.
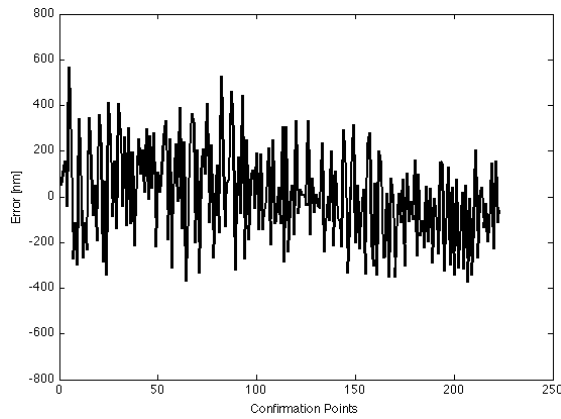
Figure 7.25: *Error in predicting the MinAngle parasitic translations along* x *axis.*
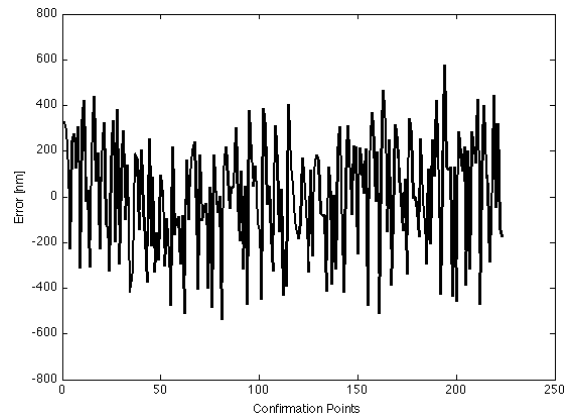
Figure 7.26: *Error in predicting the MinAngle parasitic translations along* y *axis.*

Axis	Calibration Set	Validation Set
x	±390 nm	±417 nm
y	±293 nm	±403 nm

Table 7.3: *Error in predicting the MinAngle's parasitic rotations in two data sets.*

7.5.2 Agietron Micro-Nano Calibration Results

7.5.2.1 Ultra-high-precision Model

The Stepwise Regression algorithm has been launched and a solution has been found in 5.43 seconds.

The offline results obtained in this case are similar to the ones shown in subsection 6.5 on page 84. As this time, the force is not considered at all, the results are better: regarding the prediction of the validation set (Figure 7.27), the error in predicting q_1 is ±41 nm, q_2 is ±42 nm and q_3 is ±49 nm (for the 90% of the points).

The model found in this way has been implemented in the system and a trajectory file has been imposed. The measured error in such positions is plotted in Figure 7.28. Here we obtained an error of ±58 nm for x axis, ±75 nm for y axis and ±62 nm for z axis (with a confidence interval of 90%).
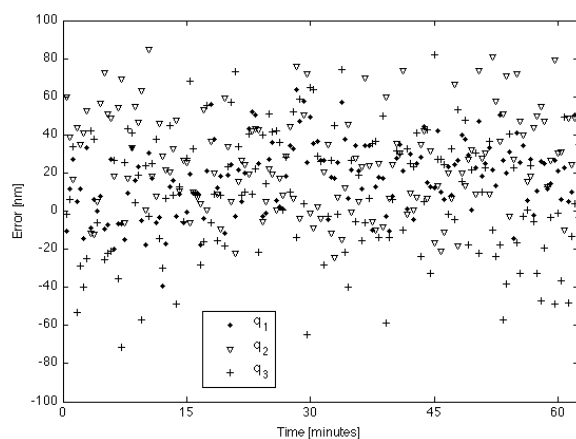
Figure 7.27: *Error in predicting the Agietron Micro-Nano validation set.*
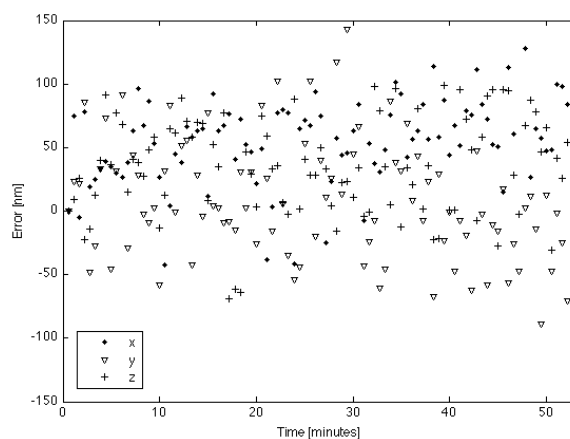
Figure 7.28: *Agietron Micro-Nano measured final positioning error.*

	q_1	q_2	q_3	x	y	z
Error	±41 nm	±42 nm	±49 nm	±58 nm	±75 nm	±62 nm

Table 7.4: *Comparison of the Agietron Micro-Nano calibration results in motor coordinates and end-effector coordinates.*

7.5.2.2 Parasitic Rotations Model

In 1.5 seconds, Stepwise Regression algorithm found the coefficients to fit the Agietron Micro-Nano parasitic rotations model (Figure 7.29 and Table 7.5).

The error in predicting the parasitic rotations around θ_x is ±0.5", θ_y is ±1.2", θ_z is ±0.4". The model has in total 34 parameters, respectively composed by 11, 13 and 10 parameters for each axis. Notice that the results on axis θ_y are worst than the other axes. This is due to a lower quality of measure on this axis caused by the presence of a 45° mirror on the laser beam path.
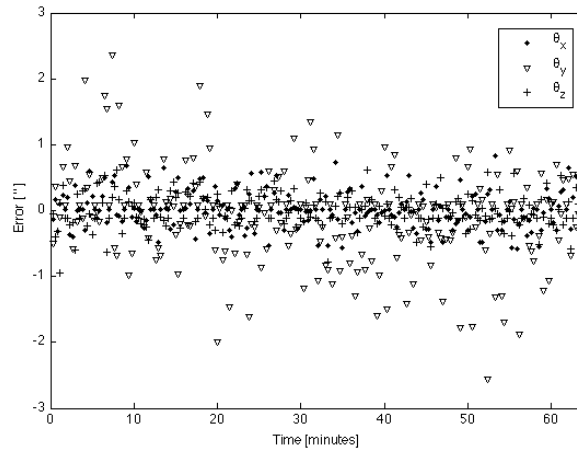
Figure 7.29: *Prediction of the Agietron Micro-Nano parasitic rotation on the validation set.*

	θ_x	θ_y	θ_z
Error	±0.5"	±1.2"	±0.4"
Parameters	11	13	10

Table 7.5: *Error in predicting the parasitic rotations of the Agietron Micro-Nano.*

7.6 Conclusions

In this chapter we covered the calibration of the Agietron Micro-Nano robot and the MinAngle robot. We also suggested a strategy to mutually compensate for their parasitic DOF. The issue in calibrating the MinAngle comes from the lack of appropriate measuring devices. To allow the calibration of this robot in all its workspace we had to develop a complicate calibration procedure.

We summarize here the most important results and conclusions of this experience:

- The modeling and identification procedure already used in subsection 6.3.1 on page 79 has also been used to identify the parameters of the Large Stroke MinAngle model and Ultra-high-precision MinAngle model. As those three models are different, this demonstrates the universality of this approach.

- The robot Agietron Micro-Nano has been calibrated with a final accuracy better than ±75 nm for the three axes at the level of the end-effector, while thermal effects are acting on it.

- A model of the Agietron Micro-Nano parasitic rotations has been established. Those are predicted with a maximum error of ±1.2".

- The MinAngle has been successfully calibrated. In a restricted workspace a maximum error of ±11" in rotations and ±1.1 µm in translation has been obtained.

- A model to predict the parasitic translations of the MinAngle along the vertical axis and the robot temperature has been established. The model is able to predict the parasitic translations with a maximum error of ±400 nm.

- For each model described in this chapter, the data processing took less then 6 second to converge.

- The overall calibration time is 17 hours.

This experience once again underlines the limitation imposed by the measuring devices, in terms of:

- Lack of ultra-high-precision measuring devices having a large course (e.g. the autocollimator).

- Sensitivity to movements along others DOF (e.g. the interferometer).

- Time consumption of the measuring phase.

In this sense, we can say that the final accuracy of a robot not only is limited by its intrinsic characteristics, but also by the measuring devices used for its calibration.

In the next chapter we will complete the calibration of the 2-robot system introducing the nano-indentation process.

Chapter 8

Case C.2: Indentation

The Vickers hardness test or indentation is a process developed to evaluate the hardness of materials. It consists in engraving a mark by pushing a diamond tip in a test material with a known force. It is then possible to calculate the hardness by measuring the mark's diagonal.

In [27] nano-indentation has been used for the first time as a calibration verification tool for ultra-high-precision robots. The idea behind this adaptation is simple: here we are not anymore interested in measuring the diagonal of the indent, but in the relative distance between the marks. The calibrated robot is used to engrave the marks on a substrate in well-known positions. Then the distance between the indents is evaluated using an electronic microscope. As the work of Dr. Fazenda represents the state of the art on this matter, for each issue we will cite the solution adopted in [27] to compare it with the current case.

The nano-indentation concept could seem very simple on paper, but we will see that it is complex to accomplish. In fact, it implies a deep knowledge of many aspects, namely: the robot and the indentation setup geometry, the measuring principles and devices used for calibration and for measuring the indent positions. Every element that is not kept in account while developing the indentation system and procedure will irreparably add more incertitude to the final error budget.

With this preliminary remark in mind, we are going to introduce each step of the calibration procedure applied to this case. Finally, we will close this chapter with the indentation results and with the conclusion to retain from this experience.

8.1   Step 1 - The Sources of Inaccuracy

The sources of inaccuracy arising from the concurrent use of the two robots and by the nano-indentation process are the following:

- Reference issues,

- External forces,

- Parasitic degrees of freedom,

- Incertitude in the measure of the indents.

The effect of the Agietron Micro-Nano parasitic rotations is amplified by the setup for the nano-indentation. A strategy to compensate for this effect is proposed.

For reference issues we consider the loss of accuracy due to the misalignment of the two robots frames. We will solve this issue by evaluating the misalignment and compensating for it. Afterwards, a common zero for the two robots will be established.

The external forces in this case are generated by the contact between the indenter and the substrate, at the moment when the indent is engraved.

The incertitude in the measure comes from the resolution of the SEM microscope employed for the measures, the incertitude in locating the center of the indent and the misalignment between the microscope and the indent substrate.

In the next section we will discuss all those topics in detail.

8.2   Step 2 and 3 - Measurements and Calibration

In the next subsection we analyze the sources of inaccuracy coming from the indentation process and by the concurrent use of the two robots. To clarify the explanation, for each issue we will present how we evaluated it (*Step 2)* and how we modeled it (*Step 3)*. Notice that here we show them all together.

While performing the indentation process, we performed different iterations of the calibration algorithm before identifying all the sources of inaccuracy. Referring to Figure 3.2 on page 35, the conditional block after *Step 5* allows the return to *Step 1* in case the desired accuracy is not reached. In this way the algorithm allows investigating further sources of inaccuracy. In case all the sources of inaccuracy have been identified and compensated but the results are still over the desired accuracy, a return to *Step 0* represents the final solution.

8.2.1   Robot Frames Alignment

While for standard robots it is easy to fix a common coordinate system in the workspace by touching a reference common to all the robots and defining its position as the zero (closed-loop calibration method [23]), in the case of multiple ultra-high-precision robots it is not possible to follow this procedure. In fact, due to the limited course of such robots, it could be not possible to touch a common reference. Thus, the reference of the system will drift and move in time, dependently on thermal effects acting on it.

To solve those problems, we will use the surface of the work-piece as common reference: the indentation substrate.

Before defining a point on it as the zero, we need to align the two robot frames, in order to minimize the error due to misalignment. To do so we use the nano-indentation process. The indenter is used to touch the substrate mounted on the MinAngle in three points (Figure 8.1, the points A(1 mm, 1 mm, 1 mm), B(1 mm, -1 mm, 1 mm) and C(-1 mm, -1 mm, 1 mm) in Agietron Micro-Nano coordinates[1]). The MinAngle vertical coordinates (z) on which the

---

[1]We perform nano-indentation on the Agietron Micro-Nano horizontal plane z = 1 mm, because such plane is wide enough to allow an important horizontal displacement of the end-effector.

contact happens are recorded (z_A, z_B and z_C). Then, using the following equation system we calculate the angular difference between the Agietron Micro-Nano frame and the substrate frame:

$$\begin{cases} \Delta\theta_x = \frac{180}{\pi} arctan\left(\frac{z_B - z_A}{2}\right) \\ \Delta\theta_y = \frac{180}{\pi} arctan\left(\frac{z_C - z_A}{2}\right) \end{cases} \tag{8.1}$$

Notice that this formula is valid only when the distance between the considered points is 2 mm.

Notice also that the Agietron Micro-Nano frame is aligned with the substrate frame and not with the MinAngle frame. This because at nano-scale, it is not possible to know the relationship that links the MinAngle frame to the substrate frame. For the purpose of performing nano-indentation, it is anyway not necessary to know such relationship. Furthermore, the possible error coming by the misalignment of the MinAngle frame and the substrate frame is limited by the manufacturing tolerances of the components. Finally, defining a common zero for the two robots will act as an "offset parameter", making this error negligible.

Once found the angular values $\Delta\theta_x$ and $\Delta\theta_y$, it is enough to displace the MinAngle of $-\Delta\theta_x$ and $-\Delta\theta_y$ to align the two frames. Thus, it is possible to verify the alignment by performing indentation in some other points: if the contact happens to the same MinAngle z value, then the frames are aligned.

By doing those operations practically we obtained $\Delta\theta_x = 0.15°$ and $\Delta\theta_y = 0.36°$. We performed three indents in the points A, B, and C (shifted of 100 μm along y axis, in order to not false the confirmation by engraving on the old indents) and we obtain z_A, z_B and z_C with maximum differences of 500 nm between them.

To finish the frames alignment, a common zero has to be defined. We displace the Agietron Micro-Nano in the point $Z(0, 0, 1 \text{ mm})$ and we perform indentation in this point. Now, the zero of the 2-robot system is composed by the end-effector coordinates of the two robots during the contact and the set of 7 temperature readings acquired in that moment.

8.2.2 Force Evaluation

Since in this case we do nott have a force sensor to evaluate the force used to engrave the indent, we used the Vickers hardness test formula to obtain it:

$$H_V = \frac{F}{A} \approx \frac{0.1891 \cdot F}{d^2} \tag{8.2}$$

Where H_V is the hardness evaluated using the Vickers test, F is the force used to produce the indent, A is the area of the indent and d is the diagonal of the indent (in mm). To calculate the force we have:

$$F \approx \frac{H_V \cdot d^2}{0.1891} \tag{8.3}$$

The hardness of the Fe64/Ni36 Invar claimed by the manufacturer is $H_B = 160$ [32], corresponding to $H_V \approx 170$ [21]. The indent size depends on how deeply the indent entered in the
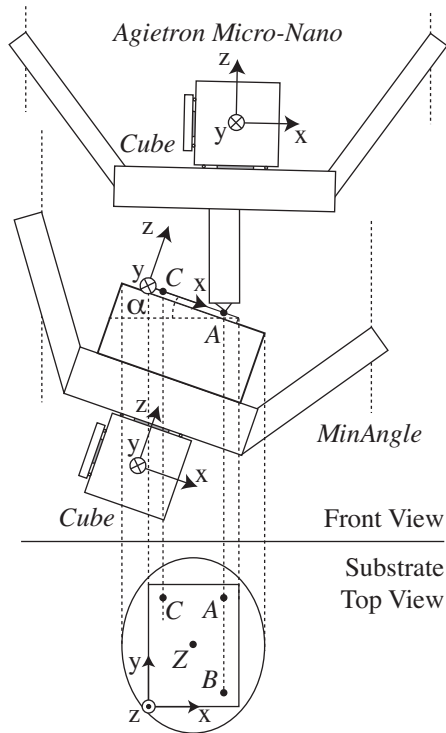
Figure 8.1: *Representation of the alignment of the two robots frames.*
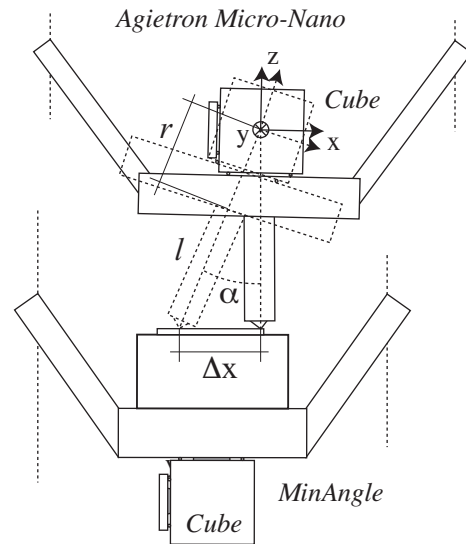
Figure 8.2: *Indentation error caused by the Agietron Micro-Nano parasitic rotations.*

material: by performing 250 nm steps, for example it is possible that the indent entered of 150 or 200 nm in the matter. Those differences produce indents of different sizes. Typically we have indents with diagonals between 5 and 10 µm (Figure 8.3), corresponding to a force between 20 mN and 90 mN.

To evaluate the drift caused by a force of this type, we implemented again the model G + T + F described in 6.3.4. We moved to the point $Z(0, 0, 1\text{ mm})$ and we measured the position of the end-effector. Then, we inserted in the model a force value F = 0.09 N and we measured the difference in displacement. For the three axes, this was difficultly measurable, since it fell under 20 nm, the measuring standard deviation. Consequentially, we decided to neglect this effect and to retain 20 nm in the error budget coming from this incertitude.

8.2.3   Indenter Parasitic Rotations

One of the tasks of the MinAngle is to compensate for the parasitic rotations of the Agietron Micro-Nano. To do so, the model of the parasitic rotations of the Agietron Micro-Nano is inserted in the MinAngle model as explained in section 7.4 on page 103. As the MinAngle center of rotation is on the substrate, and the one of the Agietron Micro-Nano is on the cube, this compensation will basically act by keeping the two end-effectors always parallel.

To allow the contact between the diamond and the substrate, the indenter has a length of 70 mm. As the Agietron Micro-Nano performs parasitic rotations while moving, the diamond tip will perform a parasitic displacement as well. As the indenter is very long, this
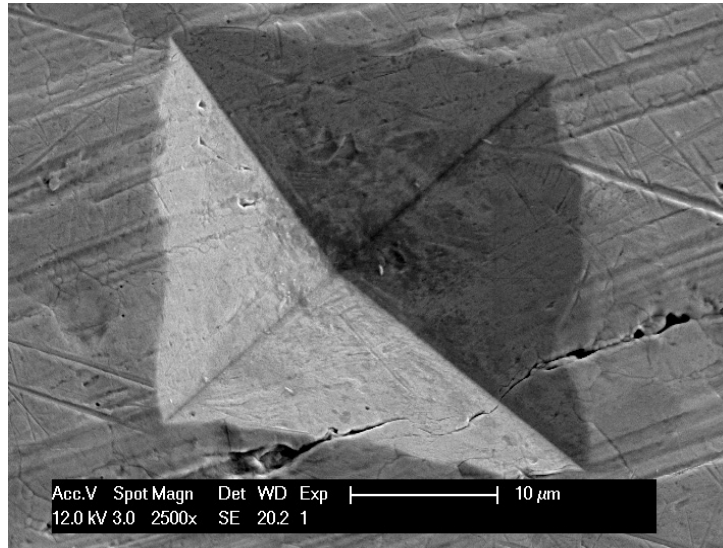
Figure 8.3: *One of the first indents engraved using the 2-robot system.*

displacement is important (maximum 25 μm, in the robot workspace extremes) and has to be compensated.

For this reason, the model of parasitic rotations used to compensate for such effect cannot be used in the way explained before, since this model is able to predict only the rotations at the level of the cube, and not the parasitic translations of the tool-tip caused by the parasitic rotations: as the two robots have two different centers of rotation, this model will only introduce more error to the indentation process (Figure 8.2).

The Agietron Micro-Nano parasitic rotations model is simply adapted in order to predict the parasitic translations of the diamond: we use the output of such model to calculate the parasitic translation of the indenter by using a simple coordinate transformation.

To have the most precise coordinate transformation, it is necessary to identify the distance between the center of the cube and the diamond tip with the maximum precision (a difference of 1 mm in the evaluation of the length will cause an error of ~200 nm in the extremes of the substrate). Since we cannot directly measure it, we perform some indents to identify the four coefficients of the following relationship:

$$\begin{cases} \Delta x = a \cdot (l + r) \cdot sin(\theta_y) + b \\ \Delta y = c \cdot (l + r) \cdot sin(\theta_x) + d \end{cases} \tag{8.4}$$

Where *a, b, c,* and *d* are the parameters to be identified, θ_x and θ_y are the parasitic rotations of the Agietron Micro-Nano, *l* is the length of the indenter and *r* is the distance between the center of the cube and the fixation of the indenter to the end-effector (evaluated to ~30 mm). The coefficients *a* and *c* have the task of "adjusting" the $l + r$ value to the real one, while *b* and *d* are simple offsets.

The MinAngle is no longer used to compensate for the parasitic rotations of the Agietron Micro-Nano, since now are now interested in the indenter tool-tip parasitic translations.

In Dr. Fazenda's thesis [27], the problem of the indenter parasitic translations was not present, since a 6 DOF robot performing pure translations has been employed to do indentation.

8.2.4   Comparison Between Interferometer and SEM Microscope

As we will use the measure capability of a SEM microscope to confirm the calibration of the robots, in first instance we have to evaluate the difference in measuring between the SEM microscope and our 6 DOF measuring system. As doubt on the definition of the nanometer between different institutes has been raised in [54], we decide to perform a practical comparison.

In [27] this is done by measuring a standard calibrated by Metas to correct the measure of the SEM. As a matter of fact, this operation validates the measure of the SEM but does not establish a link between the measure of the interferometers and the measure of the microscope.

To allow a direct comparison between the two systems, we performed the following steps:

- The two robots frames are aligned.

- Three indents are engraved in the positions Z(0, 0, 1 mm), A(100 µm, 0, 1 mm) and B(0, 100 µm, 1 mm). We used the interferometers to place the Agietron Micro-Nano end-effector in closed-loop in such points with an error between ±20 nm. We limited the distance between those points in order to limit the effects of the parasitic rotations.

- We measured the distance between the three points using the SEM microscope and we established a comparison.

8.2.5   Incertitude in Measuring the Indents

The incertitude in measuring the indents comes from the fact that at a certain level of zoom it is not possible to correctly identify the pixel containing the center of the indent. For this reason, we prefer to keep a confidence interval, dependent on the magnification we are using in the microscope. For the measures we used two levels of zoom, having the following incertitude:

- Zoom x2000; 1 pixel = 140 nm; ±2.5 pixel of incertitude corresponding to an incertitude of ±350 nm (Figure 8.4).

- Zoom x800; 1 pixel = 352 nm; ±1.5 pixel of incertitude corresponding to an incertitude of ±528 nm (Figure 8.5).

For a lower zoom, fewer pixels are needed to identify the center of the indent. Nevertheless as expected, at higher zoom corresponds a higher precision, even while using more incertitude points.
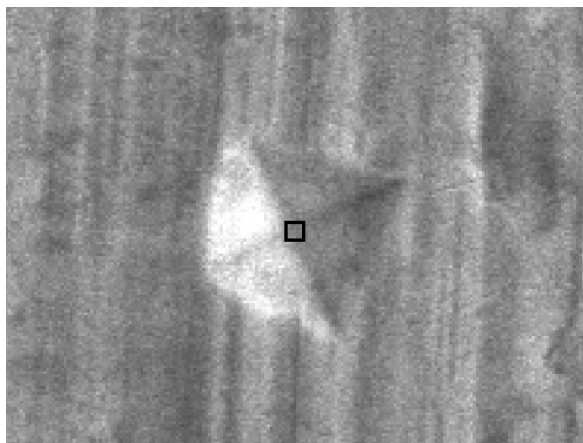
Figure 8.4: *The Zero indent, with its pixel confidence interval ±2.5 pixel, while measuring at x2000 (1 pixel = 140 nm).*
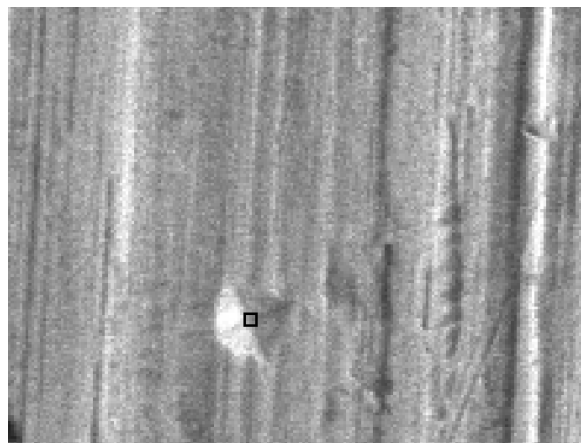
Figure 8.5: *The Zero indent, with its pixel confidence interval of ±1.5 pixel, while measuring at x800 (1 pixel = 352 nm).*

Even if the SEM microscope has the capability of measuring at "1 pixel = 1 nm" resolution, we cannot use this level of zoom because we need to have at least two indents in our field of vision to measure their relative distance.

The second source of incertitude comes from the picture-merging algorithm, used to "attach" the seven SEM pictures before evaluating the distance between the zero indents versus the others. The algorithm automatically find similar pattern in each picture, rotate and attach the pictures together in order to fit such similar patterns. We estimate the error in this process to ±0.5 pixel. This means that for each image added to the first, we will have to add an incertitude of ±176 nm (with a zoom of x800).

By adding the two sources of inaccuracy considered until now, we have a final incertitude between ±528 nm and ±1056 nm with a zoom of x800, depending on the distance of the indents.

Finally, the last source of incertitude in measuring the indents relative distance comes from the *misalignment between the substrate and the measuring frame of the SEM*. Unfortunately, it is not possible to measure the vertical axis or to ensure the parallelism of the measured surface to the substrate.

8.3   Step 4 - Model Added to Robot Controller

The model used to perform indentation at the best of its capabilities is shown in Figure 8.6. As we do not know the exact length of the indenter, we cannot yet use the indenter model to compensate for the parasitic rotations of the indenter.
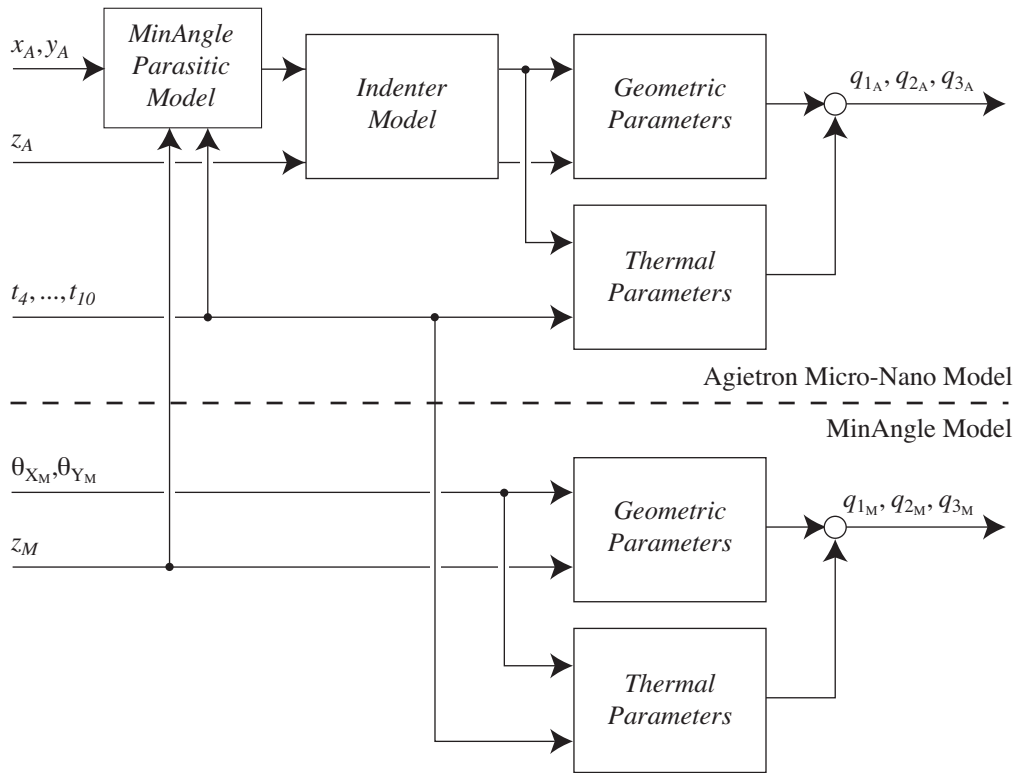
Figure 8.6: *The overall model used to perform indentation.*

8.4   Step 5 - Indentation

As already underlined before, this *step 5* actually represents the results of several iterations of the calibration algorithm. Nano-indentation and the measure of the indents have been done several times in order to identify all the possible sources of inaccuracy. In the following subsections we describe the outcome of such iterations.

8.4.1   Preliminary Measures

The first measure performed consisted in evaluating the difference between the interferometers and the reading of the SEM microscope. In Figure 8.7 we observe the measure done at the microscope. In this case, the pixel length is 120 nm. Considering an incertitude in marking the center of the indent of ±2.5 pixels, we have a total incertitude in the measure of a segment of the double, corresponding to ±700 nm. As explained in 8.2.4, those indents have been engraved at a relative distance of $100.00 \pm 0.02 \, \mu m$ moving the robot in closed-loop with the interferometers.

We obtained an error of 2.96 μm along x axis and 1.39 μm along y axis. This difference is caused by the misalignment of the substrate with the frame of the SEM and by the parasitic rotations of the indenter. In fact, to perform both points the rotations are in the order of 1-2" around the three axes. Such parasitic rotations cause a parasitic translation of the tool-tip in
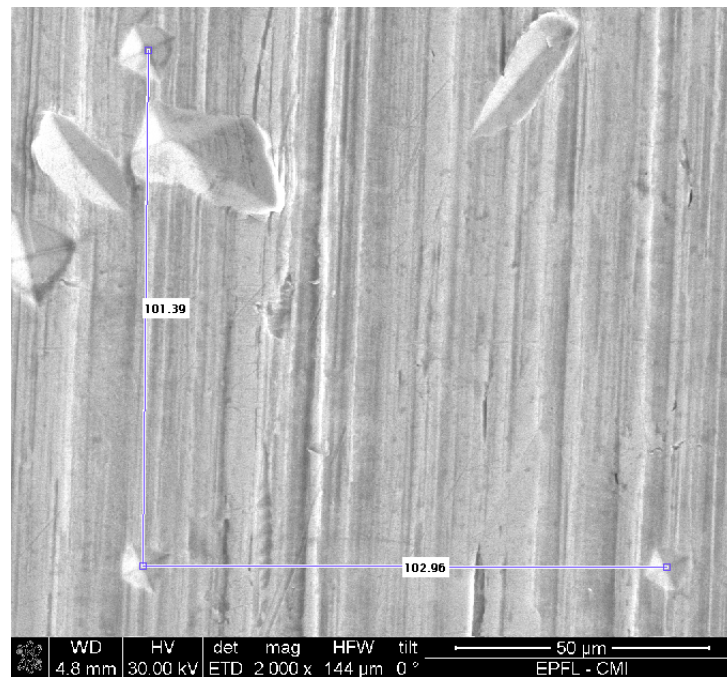
Figure 8.7: *The three indents used to perform the comparison between the interferometers and the SEM measure.*

the order of 0.5-1 μm (for a distance cube-indenter of 100 mm and an angle of 1-2") along the two horizontal directions.

The effect of parasitic rotations is significant and we have no strategies to detach it from the error caused by the misalignment between the substrate and the SEM; in other words, we have only one measure to identify two sources of inaccuracy. This means that it is not possible to establish a real alignment between the frame of the SEM microscope and the frame of the robot.

As the two effects are present at the same time *it is not possible to establish with certitude in which amplitude this difference is due to one cause or another.* For the sake of the argument, we will anyway measure the rest of the points and evaluate the overall remaining error.

8.4.2 Indentation Measure

Indentation has been performed along two lines, in order to evaluate the calibration of the two horizontal axes (Figure 8.8). The following points have been engraved and measured:

- On the x axis: $C(250\,\mu m, 0)$, $D(500\,\mu m, 0)$, $E(750\,\mu m, 0)$, $F(1000\,\mu m, 0)$.

- On the y axis: $G(0, 250\,\mu m)$, $H(0, 500\,\mu m)$, $I(0, 750\,\mu m)$, $J(0, 1000\,\mu m)$.

Using the SEM microscope, a set of 7 images has been taken. The images have been attached together using a merging algorithm. In this case, the pixel length is 352 nm. By considering

Points	θ_x ["]	θ_y ["]	Effect of rotations [µm]	Measuring Incertitude [µm]	Measure [µm]	Error [µm]
A(100 µm, 0)	-1.6	-0.8	±0.86	±0.70	102.96	2.96
C(250 µm, 0)	-4.3	-2.2	±2.34	±1.06	255.90	5.90
D(500 µm, 0)	-8.6	-4.4	±4.68	±1.23	511.80	11.80
E(750 µm, 0)	-12.0	-6.8	±6.68	±1.41	768.41	18.41
F(1000 µm, 0)	-15.4	-8.9	±8.62	±1.58	1205.02	25.02
B(0, 100 µm)	1.8	2.6	±1.53	±0.70	101.39	1.39
G(0, 250 µm)	4.3	7.1	±4.02	±1.06	250.62	0.62
H(0, 500 µm)	8.4	13.1	±7.54	±1.23	504.76	4.76
I(0, 750 µm)	12.8	18.3	±10.82	±1.41	759.26	9.26
J(0, 1000 µm)	17.2	25.4	±14.87	±1.58	1013.76	13.76

Table 8.1: *Measures of the indents and their incertitude.*

an incertitude of ±1.5 pixels in marking the center of the indents, we have an incertitude of ±3 pixels, corresponding to ±1.06 µm in measuring the distance between two indents.

In Table 8.1 we show the measuring results for those points. The effect of parasitic rotations is an estimation calculated considering the distance "center of the cube - tool-tip" as 100 mm. The measuring incertitude is calculated depending on the matters seen before. We remind here that the results presented in this table do not keep in account the error caused by the SEM frame misalignment and the parasitic rotations of the indenter. Furthermore, as the error is always greater than the measuring incertitude, we decided that it was not necessary to measure the position of the indents with greater precision.

8.4.3   Indentation Results

To prove that the indentation error is systematic and easy to handle (once it is possible to split the effects of the two sources of inaccuracy), we imported the data in Matlab and tried to find a model capable of predicting such error.

Using a simple curve-fitting tool, we were able of finding the relationship useful to predict the indentation error:

$$\begin{cases} x_c & = 0.9756x + 0.275 \\ y_c & = -8.857 \cdot 10^{-6} y^2 + 0.9947 y + 0.395 \end{cases} \tag{8.5}$$

This correction function takes in input the desired indent coordinates (x, y) and returns the corrected coordinates to insert in the Agietron Micro-Nano model to obtain them (x_c, y_c). Notice that this function is able to correct the error only for the indentation measured in this case. As we are not able to split the influence of the indenter parasitic rotations from the misalignment of the SEM frame to the substrate, using this model to engrave new indents will not improve the results. Therefore, this test is exclusively given to prove that there is still
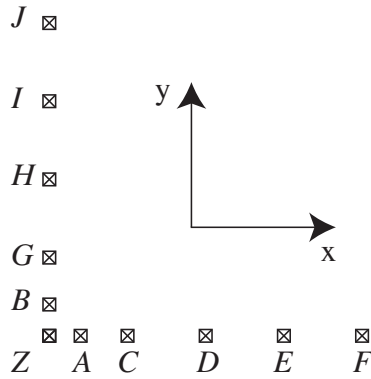
Figure 8.8: *Indents arrangement.*
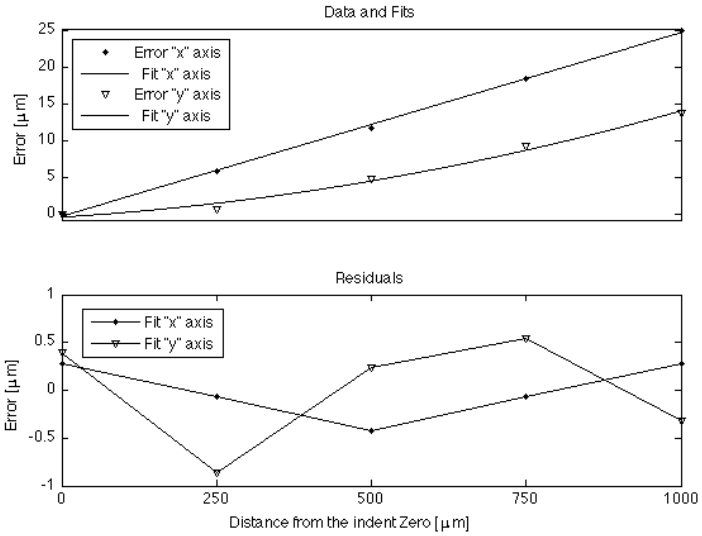
Figure 8.9: *Prediction of the indentation error using Equation 8.6.*

some easily modelable error that we cannot compensate with the system in our possession.

As a second test, we tried to model exclusively the indentation error, in the idea of building a function to add to the Agietron Micro-Nano model able to correct the systematic error between the cube and the nano-indentation tool-tip. We used again Equation 8.5, but we found new coefficients:

$$\begin{cases} \Delta x & = 0.02502x - 0.2816 \\ \Delta y & = -9.253 \cdot 10^{-6} y^2 + 0.005211 y - 0.3922 \end{cases} \tag{8.6}$$

In Figure 8.9 top, we show how this function predicts the indentation error (the lines represent the error prediction, while the "points" represent the indents). In Figure 8.9 down, we see the residual error. The RMS[2] residual error in predicting x is ±340 nm (a result in the same order of magnitude of the indentation done in [27]), while the error in predicting y is ±822 nm. It would still be possible to improve such results by adding more parameters to this model, but it would be a nonsense in this case, since with those results we already surmounted the measuring incertitude.

8.5 Step 0 - Remaining Sources of Inaccuracy

As we have seen, the remaining issues limiting the accuracy of the nano-indentation process are the parasitic rotations of the indenter and the misalignment of the SEM frame relatively to the substrate frame.

The calibration algorithm described in Chapter 3 suggests the return to *Step 0* in case some sources of inaccuracy cannot be compensated for. As a matter of fact, a radically dif-

---

[2]We use the RMS error because the confidence interval of 90% is not accurate when having only 4 points.

ferent design of the system could improve its final accuracy at the level of the tool-tip. To achieve this goal, we propose the following strategies:

- Carefully adjust the robot parallelograms in order to limit the parasitic rotations.

- Redesign the robot or some parts of the robot.

- Use of a robot with 6 DOF, in order to perform "pure translations" (as Dr. Fazenda used for its indentation procedure in [27]).

- Design a two-robot system in which the two robots are closer. In our case, the length of the indenter amplifies the influence of the parasitic rotations. As seen in subsection 7.2.1 on page 90, we deliberately increased the distance between the two robots to allow the measure of the Agietron Micro-Nano pose (the cube was not accessible to one autocollimator).

All those points are emblematic, demonstrating that the calibration and the measuring procedure have to be kept in account already during the design.

By limiting the effect of parasitic rotations, it will be then possible to align the substrate to the SEM frame, by using the points introduced in 8.2.4 and rotating the substrate under the microscope, until both the distances *ZA* and *ZB* measure 100.00 ±0.20 μm.

In the next subsections we will introduce the hardware modifications that could solve the parasitic rotations problem.

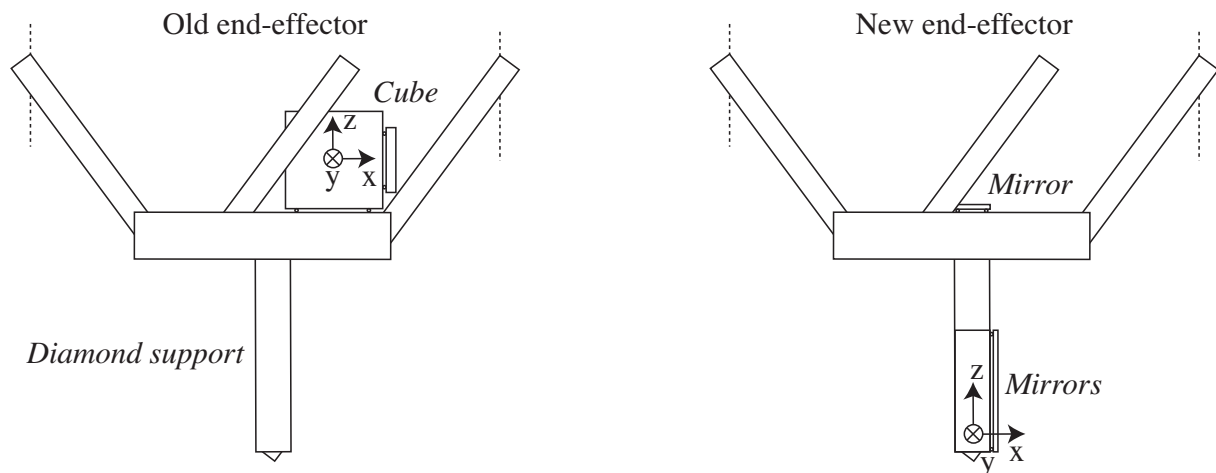### 8.5.1   Agietron Micro-Nano's End-effector Redesign

Figure 8.10: *A possible redesign of the Agietron Micro-Nano's end-effector.*

One of the difficulty in evaluating the parasitic motion of the tool-tip is due to its distance from the cube (the measuring frame). Reducing the distance between the cube and the tooltip will drastically reduce the influence of the parasitic rotations. This solution is

suitable not only for this case but also for all the applications where a long tool is connected to the end-effector.

To achieve this, we suggest a complete redesign of the robot end-effector (Figure 8.10). Instead of using a mirror cube as done in the previous cases, we suggest integrating the mirrors for the measuring devices *directly* on the diamond support. Specifically, we suggest gluing 2 mirrors on the diamond support (used to reflect the beams of two interferometers and two autocollimators) and a mirror on the end-effector (used to reflect the beam of the interferometer measuring along the vertical axis). We also suggest to measure the real angles between the mirrors, in order to evaluate and correct the perpendicularity error of the frame (this could be done in an institute specialized in ultra-high-precision measurement and measuring standards).

The advantages of this configuration are not only linked to the parasitic rotations, but also to the fact that less mass is on the end-effector, the center of mass of the end-effector coincides with its geometric center and for cost matters (buying 3 mirrors is less expensive than fabricating a mirror cube). For the mirrors on the tooltip, we suggest a size of 15 mm x 40 mm; moreover, we recommend a size of 15 mm x 15 mm for the mirror on the end-effector.

8.5.2 Measuring System Redesign

As a consequence of the new mirrors arrangement seen before, the measuring system has to be modifyed as well. The solution introduced in subsection 7.2.3 on page 96 has to be adapted to the new end-effector (Figure 8.11). Besides the support for the interferometer measuring the vertical axis, all the other supports must be lowered, in order to point their beams towards the new mirrors. The solution illustrated in Figure 8.11 was not possible when the cube was mounted on the end-effector, because the parallelograms of the Agietron Micro-Nano would have been in the way between the cube and the measuring instruments.
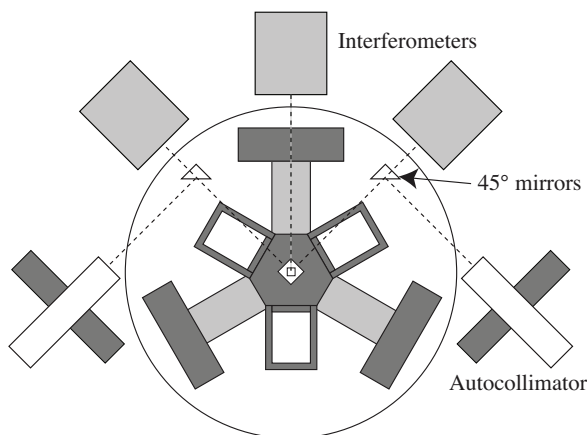

Figure 8.11: *Top view of the new arrangement of the measuring devices.*
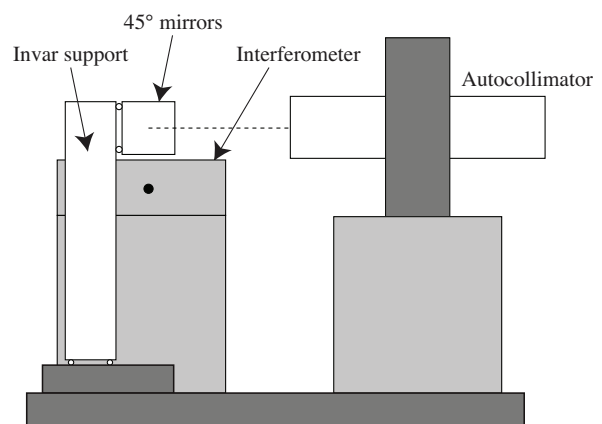

Figure 8.12: *View of the 45° mirror supports.*

To allow one interferometer and one autocollimator to reach a mirror, we suggest the solution illustrated in Figure8.12. A 45° mirror is used to reflect the beam of the autocollimator

towards the top part of the mirror. The interferometer's beam has to be pointed to the lower part of the beam, as it is foundamental to measure as much near as possible to the tooltip.

The supports for the 45° mirrors have to be designed with attention because they could decrease the quality of the measures. For this reason we suggest to glue the supports on the system base and the mirrors to the supports using three spheres, in order to avoid that the glue rotates the supports when thermally deforming.

About the choise of the material, we suggest to buy mirrors in Zerodur® and to build the supports in Invar®.

This solution once again underlines the need of considering the calibration phase already during the robot design.

8.6   Conclusions

The discrepancy between the calibration results obtained in Chapter 7 and the indentation results demonstrates that performing the calibration at the level of the end-effector frame (the cube) could in some cases not lead to a final absolute accuracy at the level of the tool-tip of the same order of magnitude. In fact, if the sources of inaccuracy between the cube and the tool-tip are not kept in account, the precision reached with the calibration procedure is lost.

Even if nano-indentation allows evaluating the accuracy of the robot at the level of the tool-tip, it does not prove to be an ideal calibration verification method. This is due to the incertitude introduced by this process that de facto justifies the need of an additional calibration.

If we consider nano-indentation as an industrial process to be calibrated, we conclude that to obtain a good final accuracy the measures must not be taken at the level of the robot frame (the cube) but at the level of the tool-tip. This gives us a general conclusion that states that, *for ultra-high-precision robots having a practical manufacturing application, it is necessary to calibrate the robot by measuring directly at the level of the tool-tip,* in order to model all the possible sources of inaccuracy with the Stepwise Regression algorithm.

Finally, in this chapter we have demonstrated the utility of the *Step 0* in the calibration procedure. Analyzing the sources of inaccuracy that still remain in the process will be a good point of departure for developing a new robot (or choose an existing robot) to improve the performances of a determined process. Furthermore, we have proposed a solution that could overcome the lack of accuracy of the nano-indentation process.

Chapter 9

Conclusion

This thesis represents the latest research on ultra-high-precision robotics performed in our laboratory, the LSRO. We first began with a brilliant work on the design of flexure parallel robots [36] and the integration of dynamics and control-related issues during the design phase [2]. After this, in [60] we have a study on the minimization of the passive DOF for ultra-high-precision parallel robots. Finally, the already cited work [27] established the basics of ultra-high-precision robot calibration and led to this thesis.

The goal of this thesis was to find a way to allow the usage of ultra-high-precision robots in an unsteady environment while external factors are acting on them without losing their final accuracy. This objective was reached by proposing a new calibration technique specific for this kind of robot used to model such external factors and compensate them in real-time. Finally, the calibration procedure was tested and validated on three robots.

The techniques and the tools introduced here add new strategies and concepts that will allow the miniaturization of assembly lines and the implementation and use of micro- and nano-factories in the industrial production.

9.1   Summary of Results

The aim of this thesis was to fill the gap between the thesis of Dr. Fazenda [27] and industrial reality. This objective has been carried out by considering the sources of inaccuracy acting on the robots, by choosing the most performing data processing algorithm, by optimizing the measuring time and the thermal stabilization time. Those improvements have led to the accomplishment of the following points:

- The calibration of an ultra-high-precision *linear axis* while keeping in account thermal effects acting on it. After a calibration process of less than 5 hours, an absolute accuracy of ±9 nm has been reached.

- By performing a calibration procedure of almost 6 hours on the robot *Agietron Micro-Nano*, we obtained a *measured* absolute accuracy of ±98 nm (±52 nm in the best case) while thermal effects and an external force were deforming the robot.

- In 17 hours we carried out the calibration of a 2-robot system (Agietron Micro-Nano and MinAngle) while keeping into account the thermal effects acting on them and their respective parasitic DOF. We also provided the basis for the concurrent use of multiple ultra-high-precision robots. Regarding the Agietron Micro-Nano we obtained a *measured* absolute accuracy of ±75 nm (±58 nm in the best case), while for the MinAngle we reached ±1.1 μm in translation and ±11″ in rotation in a limited working space.

- We performed a deep study of the nano-indentation process applied to the 2-robot system and we underlined its limitation as a calibration verification tool.

To the best of our knowledge, those are the first attempts to perform the calibration of ultra-high-precision robots while external sources of inaccuracy are acting on them.

9.2   Summary of the Original Contributions

The research performed in this thesis led to the following original contributions:

- A *general calibration procedure for ultra-high-precision robots* that keeps in account and corrects the effect of external sources of inaccuracy acting on the robots.

- The development of a *6 DOF ultra-high-precision measuring system* adapted for each case study.

- The study of the influence at nano-scale of three sources of inaccuracy on ultra-high-precision robots: *thermal effects, external forces and reference incertitude.*

- We proposed a single *data processing algorithm* based on the Stepwise Regression, capable of fitting the calibration data and producing a good quality calibrated model within seconds.

- We suggested *a mathematical approach to rapidly identify the calibrated geometric model of a robot without knowing its geometry in details,* while knowing the matching between motor coordinates and corresponding end-effector coordinates.

9.3   Articles

The following conference and journal articles have been written and presented in the context of this research:

- *Thermal Behavior of an Ultra High-Precision Linear Axis Operating in Industrial Environment,* for the 9th International Workshop on Research and Education in Mechatronics (REM2008), in Bergamo (Italy), September 18-19 2008.

- *Thermal calibration of a 3 DOFs Ultra High-Precision robot operating in industrial environment,* for in the ICRA 2010 conference (International Conference on Robotics and Automation), Anchorage, May 4-8 2010.

- *Modeling and compensation of the forces generated during the EDM process for ultra high-precision robots calibration,* for the International Symposium on Robotics (ISR 2010), in Munich (Germany), 7-9 June 2010.

- *Compensation of thermal effects and cutting-forces acting on ultra high-precision robots,* for the conference Actuator 2010 in Bremen, June 14-16, 2010.

- *Ultra-high-precision industrial robot calibration,* for the conference ICRA2011, Shanghai, May 9-13, 2011.

- *Development and calibration of ultra-high-precision robots,* for the IEEE "Robotics and Automation journal".

9.4 Challenges to Continue the Research

With the calibration procedure proposed here, we believe that no further improvements are needed considering an algorithmic and data processing point of view. For this reason we basically see three directions to continue the research in this multidisciplinary field, regarding the ultra-high-precision measure and the measure of the manufacturing process performed by the robot.

As demonstrated several times in this thesis, the bottleneck that limits the robot's final absolute accuracy is the measuring devices: as those are affected by the same sources of inaccuracy acting on the robot, it is difficult to split the measure of the robot deformation from the measuring error caused by the same inaccuracies. Moreover, those devices are often expensive and limited in course or precision. Lastly, many devices lose their measuring capability if translation/rotations along *other* DOF are performed. We believe that in the future the research in metrology will propose new measuring devices that will allow reaching new limits in the calibration of ultra-high-precision robots.

The second aspect that has to be considered is to keep in account the control issues and the dynamic of the robot in the calibration process. This matter is still linked to the measuring devices used to acquire the pose of the robot: in this thesis we acquired and averaged several measures in order to obtain a high-accuracy. In this way, most of the issues coming from the dynamics of the system are not visible. Using different measuring procedures and faster measuring instruments that could underline also the dynamic behavior of the robot is a difficult challenge that could improve once more the capabilities of ultra-high-precision robots.

The last aspect that has to be considered is the calibration towards the robot tooltip instead of the end-effector frame. We have seen that at nano-scale, performing a good calibration at the level of the end-effector will not necessarily lead to a good calibration at the level of the tooltip. Consequently for future research, we encourage the development of the following solutions:

- As we have shown in section 8.5 on page 121, *by designing an end-effector where the measuring frame is as close as possible to the tooltip frame*: by including the hardware

used for the robot's final application in the calibration process it is possible to also compensate most of the inaccuracy involving the tooltip.

- *By using a measuring strategy adapted to acquire the data directly from the robot manufacturing process.*

This last solution could be implemented on the Agietron Micro-Nano by using the μ-EDM process to perform the calibration. As seen in [42], it is possible to perform holes or other shapes on a work piece and then measure them with a microscope. Those measures will then be used to find a calibrated model with the Stepwise Regression algorithm.

The μ-EDM could also be used in the following way: by manufacturing a piece with a know geometry and use the robot equipped for μ-EDM to skim its surface. The proximity to the surface could be detected when an EDM spark is generated. Also in this case, the data for the calibration will be obtained from this experiment. For this solution, it is important to have a fine understanding of the EDM spark dynamics in order to assure the quality of the data.

Appendix

Appendix A

Measuring Device Working Principles

In this appendix we introduce the interferometer and the autocollimator, the two measuring instruments used to acquire the end-effector pose of the robots at ultra-high level of precision. The aim of this section is to briefly introduce the working principle of both devices, and explain how to configure them in order to have the best possible measure. Finally we will explain how the use of a 6 DOF system allows for the compensation of systematic errors.

A.1   The Interferometer

Interferometry is a technique of diagnosing the properties of two waves by studying the pattern of interference created by their superposition [71]. The instrument used to interfere the waves together is called interferometer.

In the interferometer (Figure A.1), a laser beam coming from the optical head is split into 2 different beams: a first beam is directly reflected by the measurand while the second is reflected by a reference mirror. These 2 beams interfere when they return to the splitter. At this point it is possible to calculate the distance in the interference pattern. Furthermore, it is possible to observe it in a detector.

The measure of the interferometer is strictly dependent on the measure of the laser wavelength in the air [84]. For this reason, every external factor capable of modifying the laser wavelength that varies considerably during the measures must be taken into account (see Table A.1).

As mentioned in the text of this thesis, the SIOS SP-2000 interferometers in our possession are equipped with a *pt100* thermal sensor. This sensor must be mounted as near as possible to the laser beam. Its reading is used to compensate for the following effects:

Source of inaccuracy	Change in environmental factors	Associate relative error $[\lambda]$
Temperature	0.3 °C	$\pm 2.8 \cdot 10^{-7}$
Pressure	50 Pa	$\pm 1.4 \cdot 10^{-7}$
Relative Humidity	3 %	$\pm 0.3 \cdot 10^{-7}$

Table A.1: *Influence of environmental factors on the interferometer reading.*
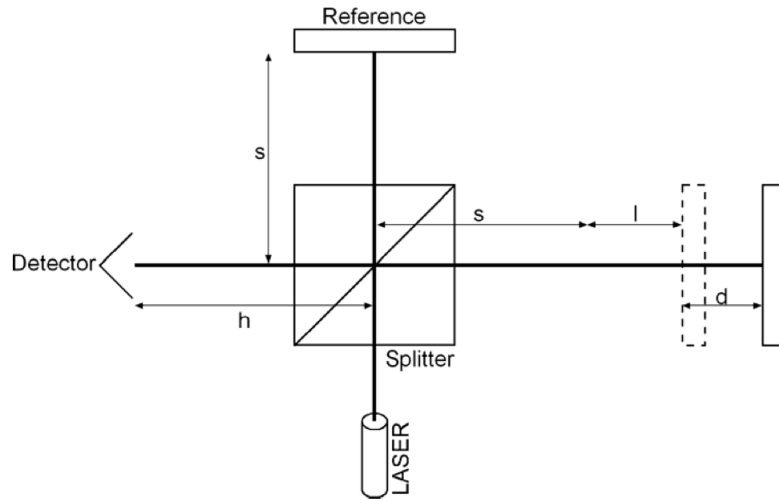
Figure A.1: *The basic operation principle of an interferometer, showing the trajectory of the measuring beam during a typical measurement. The distance* l *is called the dead-path while* d *is the distance to be measured.*

- Compensate for the wavelength changes due to variations of the air refractive index.

- By configuring the dead-path length value in the interferometer setting (Figure A.1), most of the drift caused by the change in the air temperature is kept into account. Unfortunately this feature is not described in [84] and its correction effect is not evaluated.

In addition to those techniques, we remind that it is very important to stabilize the interferometer bases (as explained in 4.2.1 on page 56), to carefully check the power of the signal (misalignment and dirt on the mirror may weaken the signal power and thus decrease the measurement quality) and wait a certain amount of time to let the system warm up.

Finally it is also necessary to choose wisely the measuring settings, such as the data filtering, the number of measures to be taken and the measures averaging. As we are interested in the static calibration of the system, we took the larger amount of measures as possible (16384 data point) to have a stable measure.

Notice that even if all those effects are kept into account, some measuring instability is still present. We evaluate the final accuracy of the interferometer between 5 and 10 nm.

A.2   The Autocollimator

A classic autocollimator [59] uses a back-illuminated cross-light reticle *A*, located at the back of the focal plane of a collimating lens *B*. The consequent image is projected to infinity to be reflected back to the instrument with a plane reflecting mirror *C* (Figure A.2).

The reflected image is focused on the back of the focal plane of the collimating lens. A beam splitter *D* is used to recover 50% of the returned light to form the source reticle. Such image can be observed with a measuring eyepiece (position sensing device) *E*. For each angular movement of the mirror *C*, a lateral displacement can be seen on the image reflected
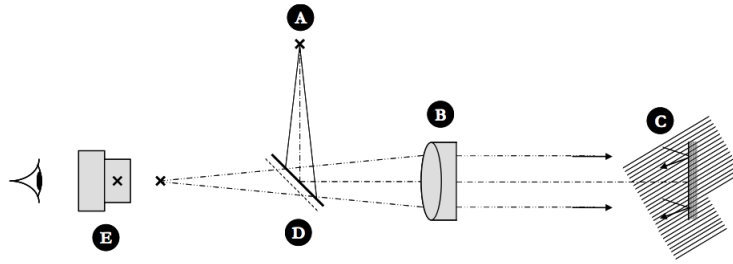
Figure A.2: *Basic principle of the classical autocollimator, according to the LDS-2000 manual.*

on the back of the focal plane of the collimated lens. If the value of the focal length of the collimated lens is *F*, then the lateral displacement will be:

$$\Delta Y = F \cdot tan(2 \cdot \Delta \theta) \tag{A.1}$$

where $\Delta \theta$ is the angular displacement of the mirror.

In the case of an electronic autocollimator this operation is performed automatically [59]. In fact, the measuring eyepiece (*E* in Figure A.2) is replaced by a position-sensitive device (PSD). Moreover, the source reticle is a laser diode. The *PSD* is an electronic device that delivers analog signals proportional to the displacement of the spot light position. These two analog signals are then converted into digital signals. Those values are the ΔY of equation A.1. At this point it is possible to calculate the angular displacements.

In comparison with the interferometer, the autocollimator does not suffer as much from thermal drift. Its great disadvantage is the limited measuring course.

A.3 Compensation of Systematic Errors

The use of a 6 DOF measuring system is undoubtedly a more practical and effective solution than using a single device mounted in different configurations during different measuring sessions. The advantage of collecting the data as the same time is evident.

Moreover, by using a 6 DOF measuring system it is also possible to actively correct the interferometers systematic errors, namely the cosine error and the abbe error.

A.3.1 Cosine Error Compensation

The cosine error is caused by an angular misalignment between the measuring axis and the object to be measured (Figure A.3 on the next page). By using the reading of the autocollimators it is possible to compensate for it for each axis [84]:

$$\Delta l = l \cdot (1 - cos(\alpha)) \tag{A.2}$$

Where *l* is the measure acquired with the interferometer, α is the misalignment value and Δl is the cosine error.
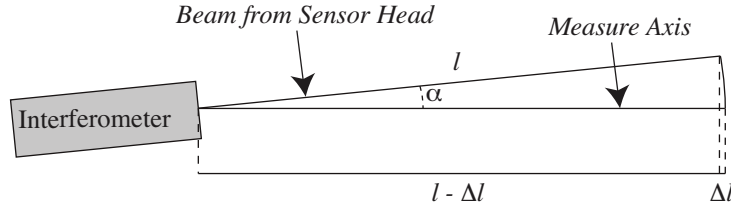
Figure A.3: *The cosine error.*

By using the reading of the two autocollimators and applying A.2 we are able to compensate the cosine error in the measure of the three interferometers:

$$\begin{cases} x_{corrected} & = x_{sios} \cdot cos\left(\theta_y\right) cos\left(\theta_z\right) \\ y_{corrected} & = y_{sios} \cdot cos\left(\theta_x\right) cos\left(\theta_z\right) \\ z_{corrected} & = z_{sios} \cdot cos\left(\theta_x\right) cos\left(\theta_y\right) \end{cases} \tag{A.3}$$

Where x_{sios}, y_{sios} and z_{sios} are the distances measured with the interferometers and θ_x, θ_y and θ_z are the angles measured with the autocollimators.

A.3.2 Abbe Error Compensation

The remaining systematic error coming from an angular error *together* with an offset between the axis of measure and the object axis is called Abbe error.

A way to minimize this effect consists in mounting the interferometer in order to point the beam as near as possible to the mirror center (this method has been used in [27]). This method is not always reliable, because as the robot moves, the laser does not point any more to the mirror center, adding the abbe error.

Considering Figure A.4, if a reading of a and α is available, it is possible to compensate this effect in real-time using the following equation:

$$\Delta l = a \cdot tan\left(\alpha\right) \tag{A.4}$$

Where a is the distance between the laser and the mirror's center of rotation and α is the tilt of the measuring device.

Again, by using Equation A.4, the reading of the autocollimators *and* the reading of the interferometers, we are able to compensate for this effect:

$$\begin{cases} x_{corrected} & = x_{sios} - a_y tan\left(\theta_y\right) - a_z tan\left(\theta_z\right) \\ y_{corrected} & = y_{sios} - b_x tan\left(\theta_x\right) - b_z tan\left(\theta_z\right) \\ z_{corrected} & = z_{sios} - c_x tan\left(\theta_x\right) - c_y tan\left(\theta_y\right) \end{cases} \tag{A.5}$$

Where x_{sios}, y_{sios} and z_{sios} are the distances measured with the interferometers, θ_x, θ_y and θ_z are the angles measured with the autocollimators and the *a*, *b*, and *c* are the relative displacements of the laser beam from the center of rotation along each axis. Each of those last coefficients is calculated in the following way, respectively for each axis:
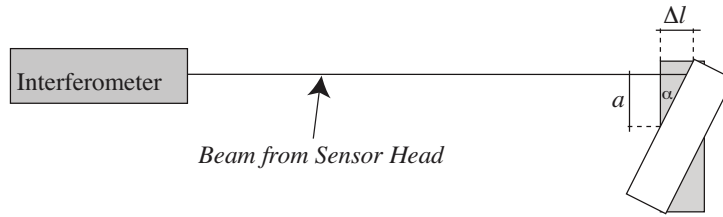
Figure A.4: *The abbe error.*

$$a_y = a_{y0} + y_{sios} \tag{A.6}$$

The a_{y0} values are measured at the beginning of the measuring session, by taking a picture of the cube and using an image analysis software to determine with a precision of 1 mm the relative spot position in zero.

Finally, the following system of equations represents the correction of the cosine error together with the abbe error:

$$\begin{cases} x_{corrected} & = x_{sios} \cdot cos\left(\theta_y\right) cos\left(\theta_z\right) - a_y tan\left(\theta_y\right) - a_z tan\left(\theta_z\right) \\ y_{corrected} & = y_{sios} \cdot cos\left(\theta_x\right) cos\left(\theta_z\right) - b_x tan\left(\theta_x\right) - b_z tan\left(\theta_z\right) \\ z_{corrected} & = z_{sios} \cdot cos\left(\theta_x\right) cos\left(\theta_y\right) - c_x tan\left(\theta_x\right) - c_y tan\left(\theta_y\right) \end{cases} \tag{A.7}$$

Appendix B

The Calibration System and the Software

The whole system is depicted in Figure B.1. Two computers are used to run the whole calibration process. A real-time computer (the *Control Computer) is* used to control the robot(s), while a second computer is used to collect the measurements and handle the thermal stabilization (the *Measuring Computer*). The two PCs are connected together through an Ethernet network and the measurement computer commands the real-time computer. The interferometers, autocollimators, the A/D converter for the thermal sensors are all connected to the measuring computer. The measuring computer sends the command to move to the next position to the control computer. Once the measures are stable those are recorded and a new position is sent to the control computer.

For the data processing we use a third personal computer on which Matlab is installed.

The software to control the robot is written in Visual C++ and the software to perform the data acquisition is written with LabView 8. In the next sections we will show some details about the LabView software used for the data-acquisition software and for indentation.

B.1 Data-acquisition Software

We wrote a LabView 8 software to handle all the data acquisition process. In this section we will show the entire modules used to acquire the data.

In Figure B.2 we show the acquisition of the 13 thermal readings, plus the target temperature for the three interferometers bases (Consigne).

The thermal measures are used to stabilize the three interferometers bases. In Figure B.3 we see the graphs of the current given to the Peltiers, the PID parameters and the current limit for the Peltiers amplifiers.

Once the interferometers bases are stabilized, the measures are started. It is possible to monitor the quality of the interferometers reading in the part of software displayed in Figure B.4. The top graph displays the measure of the interferometer. The central graph displays the corresponding standard deviation. In the lower graph we display the reading of the interferometers in the zero. The evolution of the zero is useful to understand if there are major problems in the measures (as measure "jumps" or interferometer lost of signal).
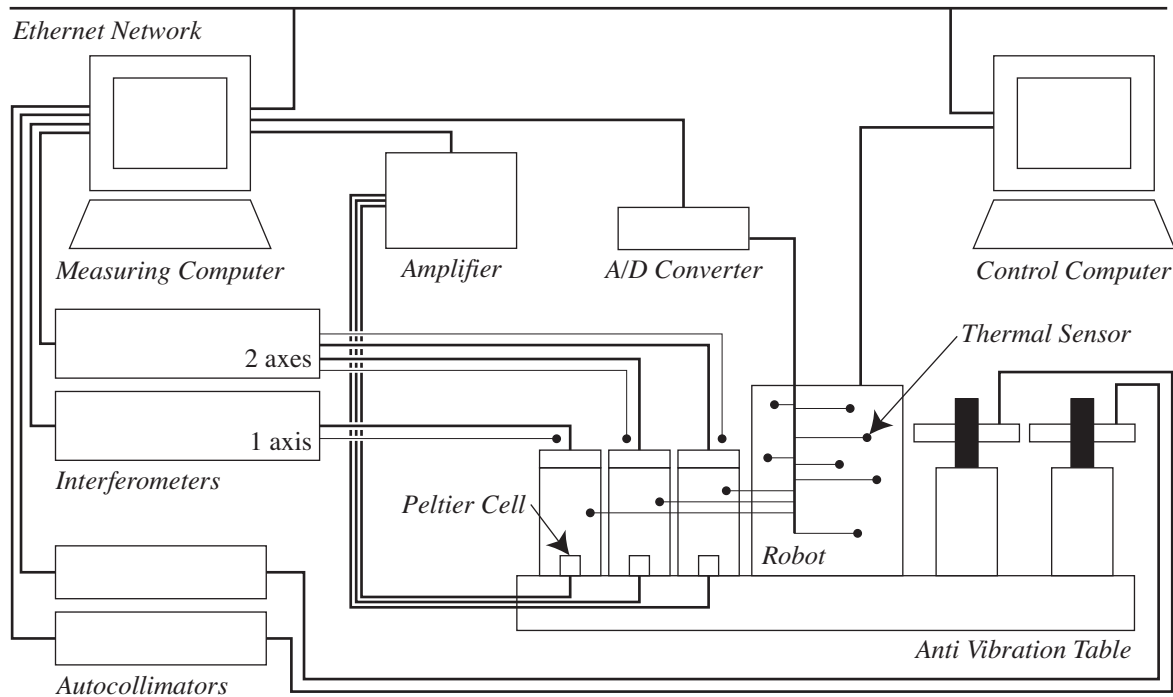
Figure B.1: *The complete system.*

In Figure B.5 we show the reading of the autocollimators and in Figure B.6 the software's part used to choose the trajectory file and to launch the measures.

B.2   Indentation Software

The indentation software is shown in Figure B.7. In the top-left part of the software we have a part used to move the robot manually. In the top-right part we have the link to the measuring devices used to perform the two indentation points in closed-loop with the interferometer. In the down-right part we have an utility used to calculate the MinAngle angular misalignment and correct it. Finally, in the down-left part we have the part to load the indentation trajectory file and to launch the process. Here it is also possible to choose the departing vertical axis position for the MinAngle.
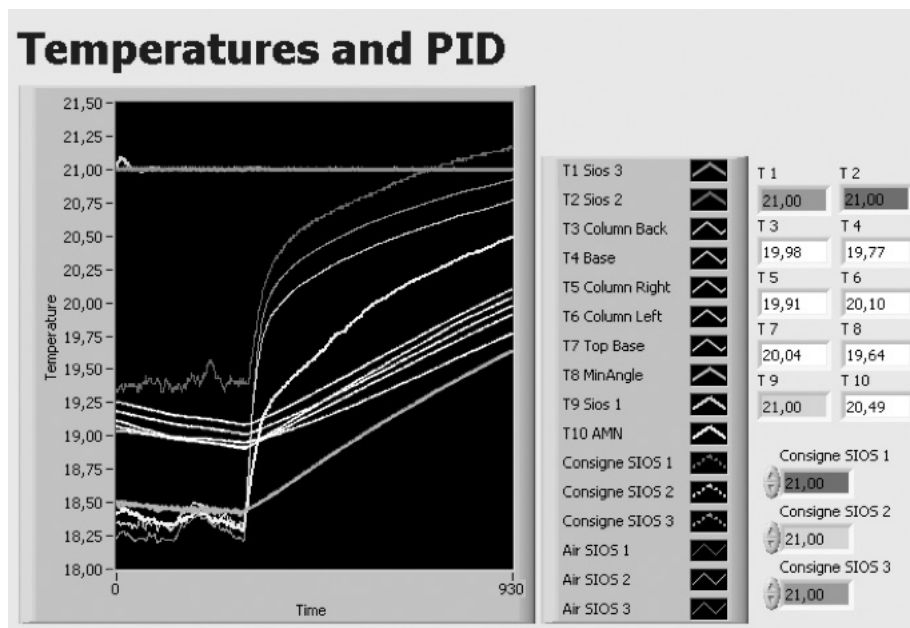
Figure B.2: *Part of software that displays the acquired temperatures.*
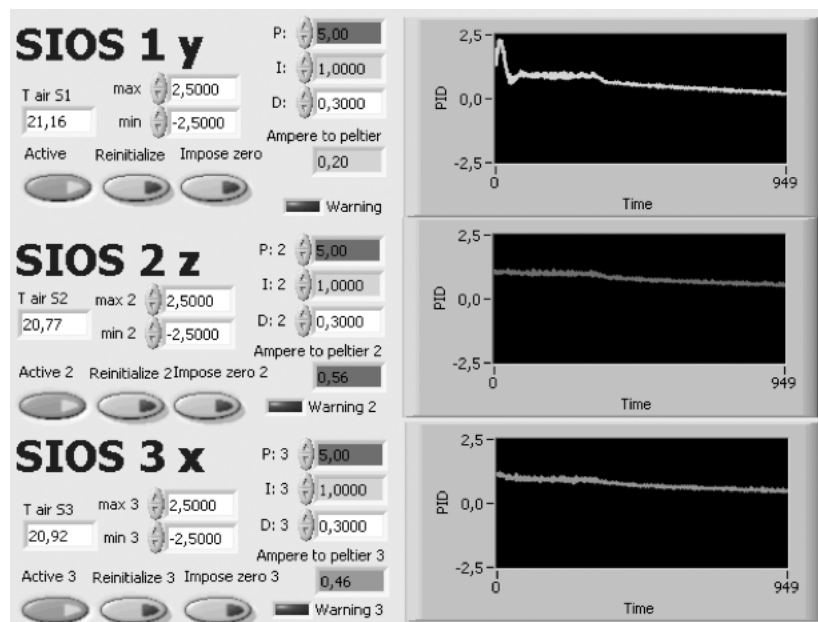
Figure B.3: *Part of software to control the stabilization of the interferometers bases.*
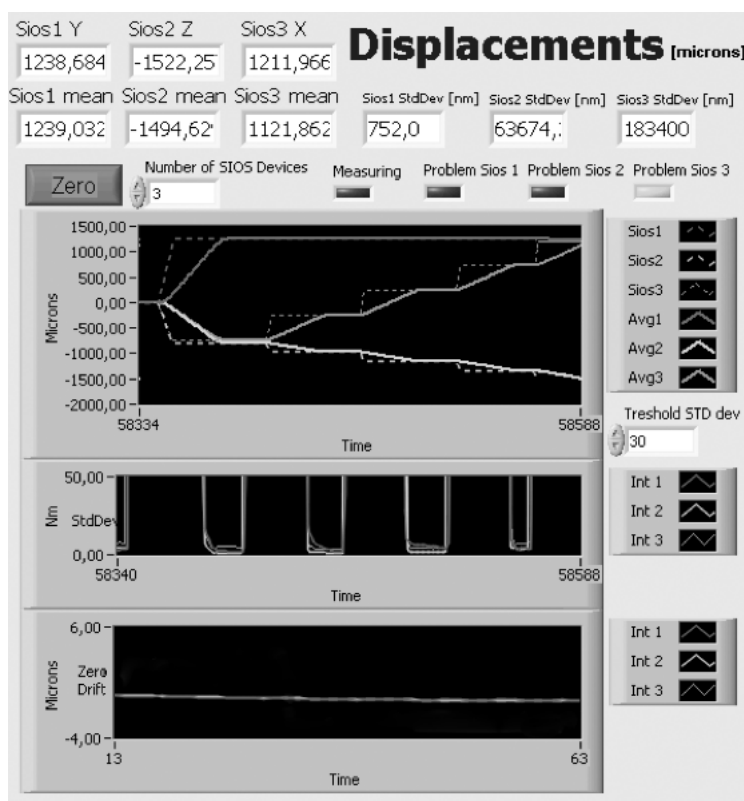
Figure B.4: *Software to monitor the interferometers reading and to check the measures quality.*
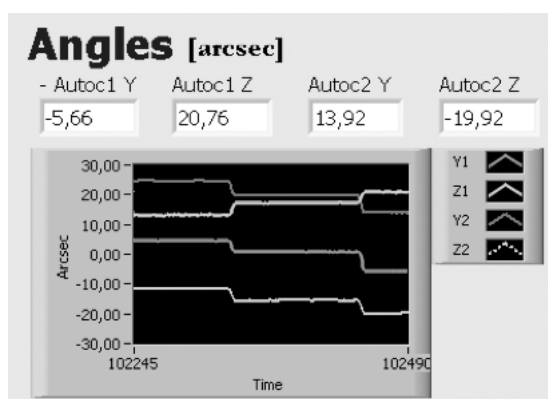
Figure B.5: *Part of software used to display the autocollimators reading.*

Figure B.6: *Part of software used to load the trajectory file and start the measures.*

Figure B.7: *Nano-indentation software.*

Appendix C

The Stepwise Regression Algorithm

To practically show how the Stepwise Regression algorithm works, we illustrate a simplified version of the coefficient search for the calibration of the linear axis (Subsection 5.3 on page 71).

To begin, we remind some elements of the calibration problem. We have at our disposal a set of measures composed by:

- Q: the vector of motor axis coordinates (corresponding to the readings of the Heidenhain® rule).
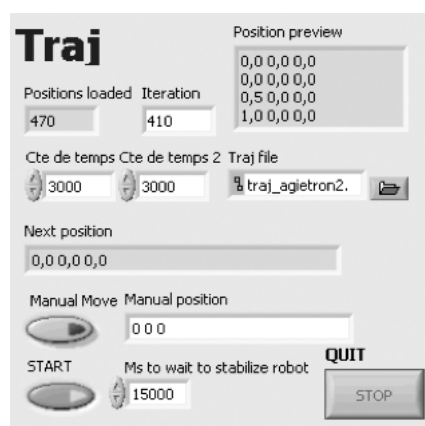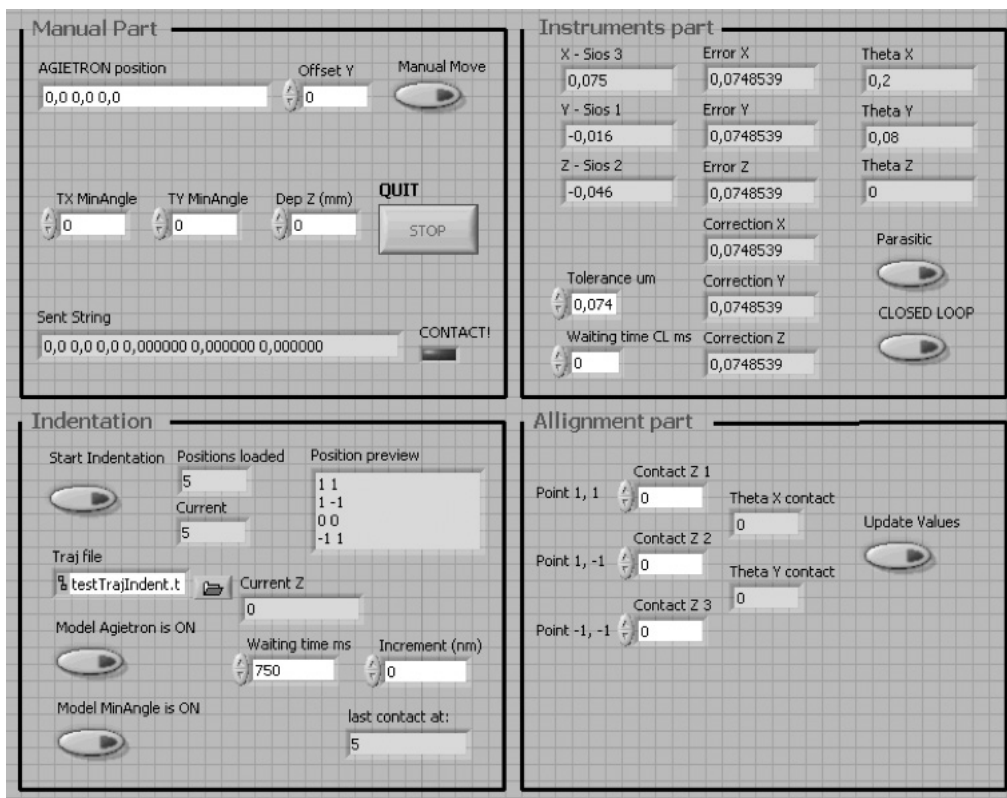
- X: the vector of measured end-effector coordinates (corresponding to the readings of the interferometer).

- $T_1, \ldots, T_{10}$:the temperatures acquired by the thermal sensors.

A further element is calculated after the measures: the vector X^2, containing the square power of every element of the vector X.

We need to find a relationship that performs the IGM transformation, while considering the thermal drift of the structure:

$$q = \alpha x^2 + \beta x + \gamma + a_1 t_1 + \ldots + a_{10} t_{10}$$

To find the values of the coefficients we use the Stepwise Regression algorithm:

$$\left(\alpha, \beta, \gamma, a_1, \ldots, a_{10}\right) = stepwise\left(\left[\begin{bmatrix} x_1^2 \\ \vdots \\ x_m^2 \end{bmatrix}\begin{bmatrix} x_1 \\ \vdots \\ x_m \end{bmatrix}\begin{bmatrix} t_{1,1} \\ \vdots \\ t_{1,m} \end{bmatrix}\ldots\begin{bmatrix} t_{10,1} \\ \vdots \\ t_{10,m} \end{bmatrix}\right], \begin{bmatrix} q_1 \\ \vdots \\ q_m \end{bmatrix}\right)$$

To maintain the explanation simple, we will use only the readings of one thermal sensor.

The first operation performed by the algorithm is scaling all the vectors[1], so that their values always fall between a specific range: [0, 1]. By doing this operation, all the values are in the same order of magnitude, making them comparable. We can say that each vector now does not express a measure anymore but a *probability* of fitting the data (the vector that better represents the vector Q "wins the entrance" in the model.

---

[1]We will express a scaled vector by adding a subscript "s" to the vector, for example Q has Q_s as scaled vector.
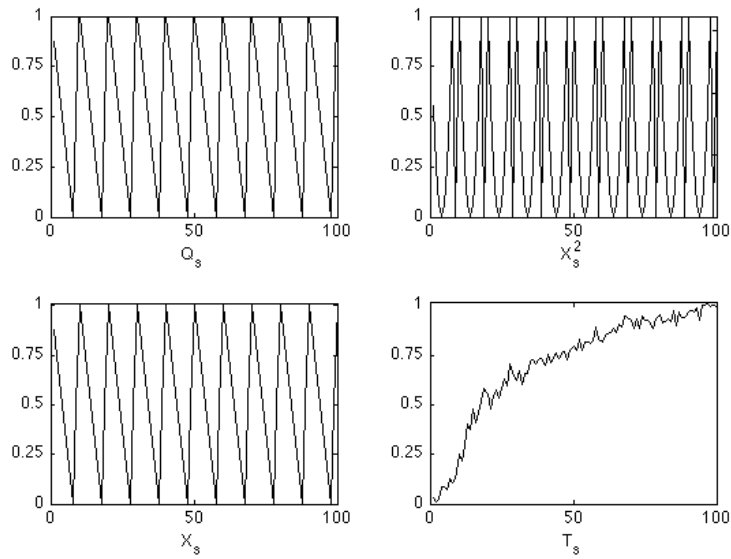
Figure C.1: *First step of the Stepwise Regression algorithm.*

To explain the process, we use 100 data points opportunely chosen from the original data set used to perform the calibration. In Figure C.1 we see the plot of all the scaled variables. As said, Q_s is the variable that has to be fitted, while X_s^2, X_s and T_s are the ones that Stepwise Regression has to use to fit Q_s. The algorithm will compute the p-value[2] of each variable and will choose the one with the lower value. The coefficient corresponding to this variable will be then calculated. We can see that Q_s and X_s are very similar. In fact, X_s is the variable that has the lower p-value. This variable is thus chosen and an appropriate coefficient to fit the data is calculated (in this case β). Notice that the scaled variables are only used to choose the good parameter; the coefficients are calculated using the standard variables.

In the second step of the regression, the function that has to be fitted is the residual of the last prediction: $Q_s - \beta X$. Stepwise Regression recalculates the p-value for each coefficient. This time, the variable that has a lower p-value is the temperature T_s. The coefficient a_1 is calculated and the new variable is inserted in the model. Notice in Figure C.2 how the two functions are similar. Notice also that the influence of X_s^2 starts to be visible.

In the final step that we consider here (Figure C.3) X_s^2 is added to the overall model and the coefficient α is calculated as well.

In the real case considered in this thesis, after X_s^2 the other temperatures are inserted in the model to augment the final accuracy of the model. Finally, the coefficient γ (the offset) has to be calculated by the user: it corresponds to the mean of the residual error.

To finish the coverage on the Stepwise Regression algorithm, we underline that in the same way in which the coefficients are added, they could be also suppressed. The algorithm checks at each step for variables that have a too high p-value.

---

[2]In statistics, the p-value represents the smallest fixed level at which the null hypothesis can be rejected. In this case, we can see this value as a "distance" between the variable that has to be fitted and the variable which we use to fit. In other words, the smaller the p-value, the bigger the correlation between the two variables.
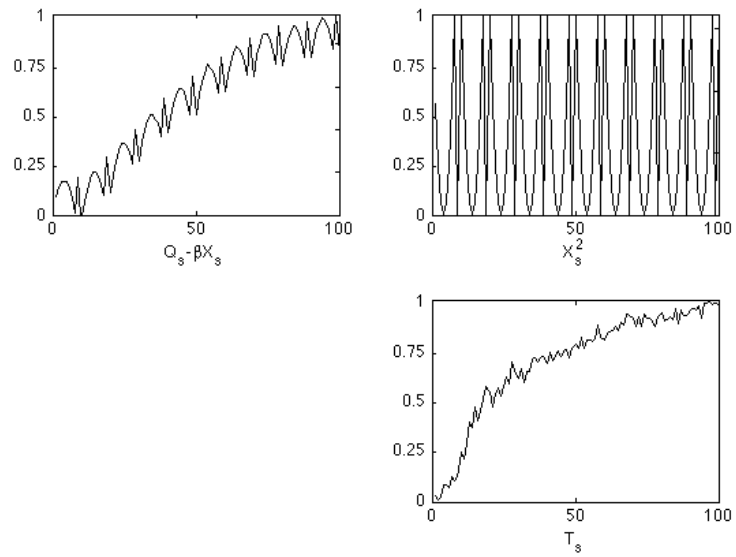
Figure C.2: *Second step of the Stepwise Regression algorithm.*
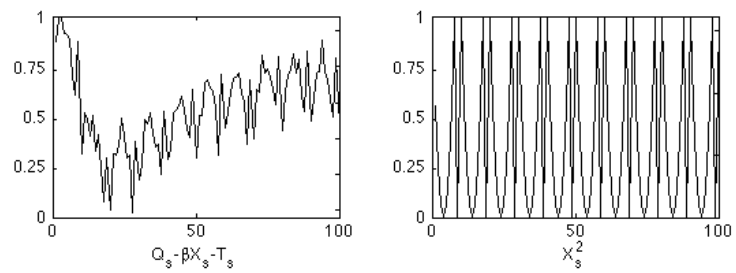

Figure C.3: *Third step of the Stepwise Regression algorithm.*

Glossary

Abbe Error: displacement caused by an angular error together with an offset between the axis of motion and the measuring axis. It characterizes every device used for distance measurement.

Accuracy: difference between a desired pose and a the pose attained in reality by the robot.

Autocollimator: optical instrument for measuring angles in a non-contact way.

Backlash: amount of lost motion due to clearance when movement is reversed and contact is re-established.

Calibration: a technique that consists in suppressing the systematic errors of a system so that the response of the system can be predicted within a certain acceptable error.

Closed-loop: configuration in which the output of a given system is used to control the system along with the input.

Cosine error: measurement error caused by an angular misalignment between the axis of motion and the axis being used to measure that motion. It characterizes every device used for distance measurements.

End-effector: part of the robot structure used to perform some desired tasks.

End-effector Coordinates: set of coordinates characterizing the position (3D) or pose (6D) of the robot end-effector with respect to a given frame.

Flexure Joint: joint that operates using the elastic property of matter and whose motions are thus free of dry friction or backlash.

Indentation: technique traditionally employed for the characterization or determination of the mechanical properties of different materials. It consists of pushing a hard tip of known geometry (indenter) into the sample surface (substrate) using a fixed peak load. The resulting footprint created in the substrate is called an indent.

Interferometer: optical instrument based on the principle of wave interference and traditionally used to measure distances with nm or even sub-nm resolution.

Inverse Geometric Model: model describing the geometry of a given robot in which the articular coordinates (output) are given as a function of the end-effector coordinates (input). The function that performs the opposite transformation is called the Direct Geometric Model (DGM).

Model Based Approach: method for processing the data for the purpose of calibrating a given robot in which a model having a full analytical formulation is used.

Model Free Approach: method for processing the data for the purpose of calibrating a given robot in which the input-output mapping is approximated without considering the robot geometric model.

Motor Coordinates: set of coordinates corresponding to the motions (angles or distances) imposed by the actuators to the active joints of the robot in order to obtain a certain pose at the end-effector.

Neural Networks: mathematical tool used to perform some task or function of interest, such as the approximation of a given input-output mapping (regression).

Orientation: set of coordinates describing the angles $(\theta_x, \theta_y, \theta_z)$ of some object with respect to a given Cartesian frame.

Parallel Robot: closed-loop mechanism in which the mobile platform is connected to the base by at least 2 kinematic chains.

Pose: set of coordinates describing the location (X, Y, Z) and orientation $(\theta_x, \theta_y, \theta_z)$ of some object with respect to a given Cartesian frame.

Position: set of coordinates describing the location (X, Y, Z) of some point of interest with respect to a given Cartesian frame.

Precision: refers to the positioning capabilities of a given robot. Since the exact meaning of this term varies from author to author, we prefer instead the use of the terms accuracy and repeatability.

Repeatability: statistical measure of how much a robot's actual motions differ one from each other when the robot is commanded to repeat a single desired motion.

Resolution: finest incremental motion that can be achieved by a robot. The resolution at the level of the joints corresponds to the resolution of the joints' sensors. The resolution in end-effector coordinates in positioning and orientation has to be measured.

Robot: manipulator with several degrees of freedom which is controlled and programmable in order to accomplish some operation of interest.

Bibliography

[1] D.S. Acjersib et al. *Theory, Experimental Results, and Recommended Standards Regarding the Static Positioning and Orienting Precision of Industrial Robots.* Robotics & Computer-Integrated Manufacturing, Pergamon Journals Ltd., 1985.

[2] J.-P. Bacher. *Conception de robots de très haute précision à articulations flexibles: interaction dynamique-commande.* PhD Thesis No. 2907, Lausanne, EPFL, 2003.

[3] S.P. Baker. *Nanoindentation Techniques.* Encyclopedia of Materials: Science and Technology, pp 5908 – 5916, Elsevier, 2001.

[4] R. Bernhardt et al. *Robot calibration.* Kluwer Academic Publisher, 1993.

[5] C. Brecher et al. *Active and passive tool alignment in ultraprecision machining for the manufacturing of highly precise structures.* Production Engineering - Research and Development, Annals of the German Academic Society for Production Engineering, 2006.

[6] C. Brecher et al. *New approaches for an automated production in ultra-precision machining.* Int J Adv Manuf Technol, Springer, 2010.

[7] F. Caccavale et al. *An experimental set-up for cooperative manipulation based on industrial manipulators.* Industrial Robot: An International Journal, MCB University Press, 2000.

[8] W.D. Callister. *Materials science and engineering. An introduction.* Wiley International Edition, 6th edition, New York, 2003.

[9] J.-S. Chen. *Fast calibration and modeling of thermally-induced machine tool errors in real machining.* Int. J. Mach. Tools Manufact., Pergamon, 1997.

[10] R. Clavel. *Conception d'un robot parallèle rapide à 4 degrés de liberté.* PhD Thesis No. 925, Lausanne, EPFL, 1991.

[11] F.L.M. Delbressine et al. *Modelling thermomechanical behaviour of multi-axis machine tools.* Precision Engineering, Elsevier, 2006.

[12] A. De Luca et al. *An Iterative Scheme for Learning Gravity Compensation in Flexible Robot Arms.* Automatica, Pergamon, 1994.

[13] A. Descoeudres et al. *Optical Emission Spectroscopy of Electrical Discharge Machining Plasma.* Centre de Recherches en Physiques des Plasmas (CRPP), EPFL, 2003.

[14] A. Descoeudres. *Characterization of electrical discharge machining plasmas.* PhD Thesis No. 3542, Lausanne, EPFL, 2006.

[15] Q. Ding et al. *Calibration of A 2-DOF Planar Parallel Robot: Home Position Identification and Experimental Verification.* Niagara Falls, Canada, 2005.

[16] L. Dong et al. *Robotics in the Small. Part II: Nanorobotics.* IEEE Robotics & Automation magazine, september 2007.

[17] J. Dratler. *A proportional thermostat with 10 microdegree stability.* Rev. Sci. Instrum., American Institute of Physics, 1974.

[18] G. Ecorchard et al. *Self-Calibration of Delta Parallel Robots with Elastic Deformation Compensation.* IEEE/RSJ International Conference on Intelligent Robots and Systems, 2005.

[19] Edmund Optics®. *Optics and Optical Instruments Catalog,* 2007.

[20] A.Y. Elatta et al. *An Overview of Robot Calibration.* Information Technology Journal 3, Asian Network for Scientific Information, 2004.

[21] Engineer's Handbook website. *http://www.engineershandbook.com/Tables/hardness.htm,* February 2011.

[22] W.T. Estler. *High-accuracy displacement interferometry in air.* Applied optics, 1985.

[23] L. Everett et al. *A Sensor Used for Measurements in the Calibration of Production Robots.* Atlanta, IEEE, 1993.

[24] R.D. Esman et al. *100-µK temperature controller.* Rev. Sci. Instrum. 54, American institute of Physics, 1983.

[25] K.C. Fan et al. *Development of a Constant Temperature Environment Chamber with High Stability.* Material Science Forum Vol 594, Trans Tech Publication, Switzerland, 2008.

[26] A. Faretta. *Sviluppo di un sistema ad articolazioni flessibili per la microEDM.* M.Sc. Thesis, Politecnico di Milano, 2004.

[27] N. Fazenda. *Calibration of high-precision flexure parallel robots.* PhD Thesis No. 3712, Lausanne, EPFL, 2007.

[28] N. Fazenda et al. *Calibration of the 6 DOF high-precision flexure parallel robot "Sigma 6".* Chemnitz, Fraunhofer, 2006.

[29] H. Flordal et al. *Supervision of Multiple Industrial Robots - Optimal and Collision Free Work Cycles.* International Conference on Control Applications, IEEE, 2004.

[30] H. Frayssinet. *Méthode d'étalonnage d'une machine-outil à cinématique parallèle à cinq axes à grands angles d'inclinaison.* PhD Thesis No. 3702. Lausanne, EPFL, 2007.

[31] Gisler C. *Vermessung und Kalibrierung einer Mikroelektroerosionsmaschine.* M.Sc. Thesis, ETH Zürich, 2006.

[32] Goodfellow's website. *http://www.goodfellow.com/*, in Catalogue, Materials Properties, "I", Invar. February 2011.

[33] T.A. Harris. *Rolling bearing analysis.* Wiley, New Jersey, 2001.

[34] M. Hattori et al. *Estimation of thermal-deformation in machine tools using neural network technique.* Journal of Material Processing Technology 56, Elsevier, 1996.

[35] Heidenhain website. *http://www.heidenhain.de/en_US/products_and_applications/ length_measurement/exposed_linear_encoders/*, March 2011.

[36] S. Henein. *Conception des structures articulées à guidages flexibles de haute précision.* PhD Thesis No. 2194, Lausanne, EPFL, 2000.

[37] J.M. Hollerbach. *A Survey of Kinematic Calibration.* In Robotic Review, O. Khatib, J.J. Craig and T. Lozano-Perez (editors), MIT Press, 1988.

[38] J. Hwang et al. *Compensation of temperature induced position measuring error in the ultra-precision moving robot system.* International Conference on Smart Manufacturing Application, KINTEX, Korea, 2008.

[39] P. Helmer. *Conception systématique de structures cinématiques orthogonales pour la microrobotique.* PhD Thesis No. 3365. Lausanne, EPFL, 2006.

[40] M.J. Jackson. *The Future of Micro- and Nanomanufacturing.* Microfabrication and nanomanufacturing, CRC Press LCC, 2006.

[41] G. Jaeger. *Limitations of precision length measurements based on interferometers.* Measurement 43, Elsevier, 2010.

[42] C. Joseph. *Contribution à l'accroissement des performances du processus de µEDM par l'utilisation d'un robot à dynamique élevée et de haute précision.* PhD Thesis No. 3281, Lausanne, EPFL, 2005.

[43] C. Kuang et al. *A high-precision five-degree-of-freedom measurement system based on laser collimator and interferometry techniques.* Review of scientific instruments 78, American Institute of Physics, 2007.

[44] N.T. Larsen, *50 Microdegree Temperature Controller.* The review of scientific instruments, American Institute of Physics, 1968.

[45] K.M. Lawton et Al. *A high-stability air temperature control system.* Precision Engineering, Elsevier, 2000.

[46] J.W. Li et al. *Thermal-error modeling for complex physical systems: the-state-of-arts review*. Int Journal Adv Manuf Technol, 2009.

[47] S. Li et al. *A study of pre-compensation for thermal errors of NC machine tools*. Int. J. Mach. Tools Manufact., Pergamon, 1997.

[48] J.C. Liang et al. *A comprehensive Error Compensation System for Correcting Geometric, Thermal, and Cutting Force-Induced Errors*. The International Journal of Advanced Manufacturing Technology, Springer-Verlag, 1997.

[49] Z.-C. Lin et al. *The building of spindle thermal displacement model of high speed machine center*. Int J Adv Manuf Technol, 2006.

[50] C.-H. Liu et al. *Development of a laser-based high-precision six-degrees-of-freedom motion errors measuring system for linear stage*. Review of Scientific Instruments 76, American Institute of Physics, 2005.

[51] Z. Lu et al. *Force Sensing and Control in Micromanipulation*. Transaction on Systems, Man, And Cybernetics, IEEE, 2006.

[52] E. Lubrano. *Calibration of a 6 DOF High-Precision Parallel Robot using Artificial Neural Networks*. M.Sc. Thesis, EPFL, 2005.

[53] E. Manske et al. *Advances in Traceable Nanometrology with the Nanopositioning and Nanomeasuring Machine*, in Nanosacle Calibration Standards and Methods: Dimentional and Related Measurements in the Micro- and Nanometer Range. G. Wilkening and L. Koenders (editors), Wiley-VCH Verlag, pp 47-59, 2005.

[54] F. Meli. *International comparison in the field of nanometrology: pitch of 1D gratings (Nano4)*. Proceedings of the 2nd EUSPEN International Topical Conference, Vol. 1, p 358, Torino, May 2001.

[55] A. Menciassi et al. *From "Macro" to "Micro" Manipulation: Models and Experiments*. Transactions on Mechatronics, IEEE, 2004.

[56] B.W. Mooring et al. *Fundamentals of Manipulator Calibration*. John Wiley & Sons, 1991.

[57] Y. Nakamura et al. *Mechanics of Coordinative Manipulation by Multiple Robotic Mechanisms*. IEEE, 1987.

[58] *The MathWorks™ Statistics Toolbox™ 6, User guide*. The MathWorks™, 2008.

[59] *Newport® LDS-1000 Autocollimator*, User's Manual.

[60] T. Niaritsiry. *Optimisation de la conception du robot parallèle delta cube de très haute précision*. PhD Thesis No. 3567, Lausanne, EPFL, 2006.

[61] H. Ota et al. *Forward kinematic calibration and gravity compensation for parallel-mechanism-based machine tools*. IMechE, 2002.

[62] E. Pernette. *Robot de haute précision à 6 degrés-de-liberté pour l'assemblage de microsystèmes.* PhD Thesis No. 1909, Lausanne, EPFL, 1998.

[63] Fact sheet *Dyneema high-strength, high-modulus polyethylene fiber.* DSMBrand, 2008.

[64] P. Pham. *Design of Hybrid-Kinematic Mechanism for Machine Tools.* PhD Thesis No. 4314, Lausanne, EPFL, 2009.

[65] P. Pham et al. *Orion MinAngle: A flexure-based, double-tilting parallel kinematics for ultra-high precision applications requiring high angles of rotation.* Tokyo, ISR Proceedings, 2005.

[66] J.P. Prenninger et al. *Real-time contactless measurement of robot pose in six degrees of freedom.* Measurement 14, Elsevier, 1995.

[67] M. Rahman et al. *Modeling, measuring and error compensation of multi-axis machine tools. Part I: theory.* International Journal of Machine Tools and Manufacture, Pergamon, 2000.

[68] R. Ramesh et al. *Error compensation in machine tools – a review. Part I: geometric, cutting-force induced and fixture-dependent errors.* Singapore, Pergamon, 2000.

[69] R. Ramesh et al. *Error compensation in machine tools – a review. Part II: thermal errors.* Singapore, Pergamon, 2000.

[70] R. Ramesh et al. *Support Vector Machines Model for Classification of Thermal Error in Machine Tools.* The International Journal of Advanced Manufacturing Technology, Springer-Verlag, 2002.

[71] P.K. Rastogi. *Optical Measurement Techniques and Applications.* Artech House, Inc. Boston - London, 1997.

[72] M. Richard et al. *A new concept of modular kinematics to design ultra-high precision flexure-based robots.* Munich, ISR proceeding, 2010.

[73] Z.S. Roth et al. *An overview of Robot Calibration.* IEEE Journal of Robotics and Automation, Col. ra-3, No. 5, pp 377-385, 1987.

[74] D. Sarid et al. *A ±15 microdegree temperature controller.* Rev. Sci. Instrum. Vol. 45. American Institute of Physics, 1974.

[75] U. Seker. *The Measurement of Temperature during machining.* International Conference on Power Transmission, 2003.

[76] N. Srinivasa et al. *Automated measurement and compensation of thermally induced error maps in machine tools.* Precision Engineering, Elsevier, 1996.

[77] V.A. Sukaylo et al. *Development and verification of a computer model for thermal distortions in hard turning.* J Mater Process Technol 155–156:1821–1827, 2004.

[78] M. Thurneysen. *Méthode systématique de conception de cinématiques parallèles.* PhD Thesis No. 3009, Lausanne, EPFL, 2004.

[79] D. Tolfree. *Commercialising Nanotechnology concepts-products-markets.* Int. J. Nanomanufacturing, Inderscience Enterprises Ltd. 2006.

[80] P.-C. Tseng et al. *A Study of High-Precision CNC Lathe Thermal Errors and Compensation.* The International Journal of Advanced Manufacturing Technology, Springer-Verlag, 2002.

[81] P.-C. Tseng et al. *The Neural-fuzzy Thermal Error Compensation Controller on CNC Machining Center.* JSME International Journal, 2002.

[82] E. Sahin Conkur et al. *Clarifying the definition of redundancy as used in robotics.* Robotica, volume 15, pp 583-586, Cambridge University Press, 1997.

[83] Schott Website (the owner of the Zerodur® trademark): *http://www.schott.com/advanced_optics/english/our_products/zerodur/zerodur.html,* January 2011.

[84] *SIOS® SP 2000 laser interferometer,* User's manual.

[85] B. Shirinzadeh et al. *Laser interferometry-based guidance methodology for high-precision positioning of mechanisms and robots.* Robotics and Computer-Integrated Manufacturing, Elsevier, 2010.

[86] P. Vanherck et al. *Compensation of thermal deformations in machine tools with neural nets.* Computers in Industry, Elsevier, 1997.

[87] W.K. Veitschegger et al. *Robot calibration and compensation.* IEEE Journal of Robotics and Automation, Vol. 4, No. 6, 1988.

[88] I. Verettas et al. *PocketFactory: a modular and miniature assembly chain including a clean environment.* Besançon, IWMF, 2006.

[89] P. Vischer. *Improving the accuracy of parallel robots.* Ph.D. Thesis, Lausanne EPFL, 1996.

[90] L.Q. Wang et al. *Operating temperature in high-speed ball bearing.* Proc. IMechE Vol. 221 Part C: J. Mechanical Engineering Science 353–359, 2007.

[91] Y. Wang et al. *Compensation for the thermal error of a multi-axis machining center.* Journal of Materials Processing Technology, Elsevier, 1996.

[92] M. Wautelet. *Scaling laws in the macro-, micro- and nanoworld.* Eur. J. Phys. 2001.

[93] S. Yang et al. *Real-time cutting forces induced error compensation on a turning center.* Int. J. Mach. Tools Manufact., Pergamon, 1997.

[94] S. Yang et al. *The improvement of thermal error modeling and compensation on machine tools by cmac neural network.* Int. J. Mach. Tools Manufact., Pergamon, 1996.

[95] H. Yang H et al. *Dynamic neural network modeling for nonlinear, nonstationary machine tool thermally induced error.* Int J Mach Tools Manuf 45:455–465, 2005.

[96] H. Wu et al. *Synthetically Modeling of Thermal Error and Grinding Force Induced Error on a Precision NC Cylindrical Grinding Machine.* Advanced Materials Research, Trans Tech Publications, 2007.

[97] H. Zhuang et Al. *Camera-Aided Robot Calibration.* Boca Raton, CRC Press, 1996.

Curriculum Vitae

Emanuele Lubrano
Rue de la tour 6
1004 Lausanne (VD) Switzerland
emanuele.lubrano1@gmail.com

Nationality: Italian
Born: 31st July 1982
Civil status: Single

Education

Mar. 07 – Aug. 11 **EPFL - Ecole Polytechnique Fédérale de Lausanne** (Switzerland), Doctoral School; Ph.D. in Manufacturing Systems and Robotics. Ph.D. thesis.

Mar. 04 – Dec. 06 **Università di Genova**, Facoltà di Ingegneria Informatica (Italy); M.Sc. in Computer Science Engineering, specialization in automation and robotics (Grade: 100/110). M.Sc. thesis done at EPFL: "Calibration of a 6 DOF high-precision parallel robot using Artificial Neural Networks" (Grade: 6/6).

Professional Experience

Mar. 07 – Aug. 11 **EPFL - Ecole Polytechnique Fédérale de Lausanne, Laboratory of Robotic Systems** (Switzerland); Research assistant for Prof. Reymond Clavel:

Sep. 05 – Feb. 07 **EPFL - Ecole Polytechnique Fédérale de Lausanne, Laboratory of Robotic Systems** (Switzerland); Undergraduate research assistant for Prof. Reymond Clavel: Calibration of 3 ultra high-precision robots; reports writing and presentations.

Jul. 04 – Sep. 04 **EPFL - Ecole Polytechnique Fédérale de Lausanne, Laboratory of Robotic Systems** (Switzerland): Summer traineeship on the development of an ultra high-precision measuring system.

Skills

- **Languages**: Italian (mother tongue), French (fluent), English (fluent)

- **Programming languages**: C/C++, C#, Java, SQL, VHDL.

- **OS**: Linux, UNIX, Windows and Macintosh.

- **Engineering software**: Matlab, Mathematica, LabView, SolidWorks.

Publications

- E.Lubrano, M. Richard and R. Clavel. *Development and calibration of ultra-high-precision robots*, for the IEEE "Robotics and Automation journal".

- E.Lubrano, M. Bouri and R. Clavel. Ultra-high-precision Industrial Robots Calibration. Presented during the 2011 IEEE International Conference on Robotics and Automation ICRA2011, Shanghai, China.

- E. Lubrano and R. Clavel. Compensation of thermal effects and cutting-forces acting on ultra high-precision robots. Presented during the 12th International Conference on new actuators Actuator2010, Bremen, Germany.

- E. Lubrano, A. Prodan and R. Clavel. Modeling and Compensation of Cutting-Forces Generated During the EDM Process for Ultra High-Precision Robots. Presented during the 41st International Symposium on Robotics ISR2010, Munich, Germany.

- E. Lubrano and R. Clavel. Thermal Calibration of a 3 DOF Ultra High-Precision Robot Operating in Industrial Environment. Presented during the 2010 IEEE International Conference on Robotics and Automation ICRA2010, Anchorage, Alaska, US.

- E. Lubrano and R. Clavel. Thermal Behavior of an Ultra High-Precision Linear Axis Operating in Industrial Environment. Presented during the 9th International Workshop on Research and Education in Mechatronics REM2008, Bergamo, Italy.

- N. Fazenda, E. Lubrano and R. Clavel. Calibration of the Six DOF High-Precision Flexure Parallel Robot "Sigma 6". Keynote paper. Proceeding of the 5th Chemnitz Parallel Seminar PKS2006, Germany.

Extra-curricular Activities

Sep. 09 – Mar. 11 **Emergency Psychologist for the EPFL campus** (Switzerland): Support of witnesses of a traumatic event on the campus; RNAPU certification.

Sep. 08 – Jun. 09 **President of the EPFL Student association "Xchange"** (Switzerland), part of Erasmus Student Network: Led a group of 25 members and managed an annual budget of 50k CHF; Fundraise, sponsorship, relation with EPFL direction.

Sept. 07 – Jun. 08 **Venturelab**, Lausanne (Switzerland); Participation in the course Venture Challenge: Wrote 2 business plans for 2 startups, business models presented to sponsors; Participated to the Venture08 competition, Zürich (Switzerland).

Interests

- Amateur bassist and drummer; guitarist and lead voice in a rock band.

- Passionate of mountain sports: ski, ski touring, rock-climbing and hiking.